CONTACT METAL-DEPENDENT ELECTRICAL TRANSPORT IN CARBON NANOTUBES AND FABRICATION OF GRAPHENE NANORIBBONS

by

David Perello

B.S. in Electrical Engineering, University of Pittsburgh, 2007

M.S. in Electrical Engineering, University of Pittsburgh, 2010

Submitted to the Graduate Faculty of

the Swanson School of Engineering in partial fulfillment

of the requirements for the degree of

Doctor of Philosophy

University of Pittsburgh

2013

UNIVERSITY OF PITTSBURGH

SWANSON SCHOOL OF ENGINEERING

This proposal was presented

by

David Perello

It was defended on

March 29, 2013

and approved by

Guangyong Li, PhD, Assistant Professor, Department of Electrical and Computer Engineering

William Stanchina, PhD, Professor, Department of Electrical and Computer Engineering

Kevin Chen, PhD, Associate Professor, Department of Electrical and Computer Engineering

Alexander Star, PhD, Associate Professor, Department of Chemistry

Dissertation Director: Minhee Yun, PhD, Associate Professor, Department of Electrical and
Computer Engineering

CONTACT METAL-DEPENDENT ELECTRICAL TRANSPORT IN CARBON NANOTUBES AND FABRICATION OF GRAPHENE NANORIBBONS

David Perello, PhD

University of Pittsburgh, 2013

In this thesis, we fabricate and characterize carbon nanotube (CNT) and graphene-based field effect transistor devices. The CNT-based work centers around the physics of metal contacts to CNT, particularly relating the work function of contact metals to carrier transport across the junction. The graphene work is motivated by the desire to utilize the high carrier mobility of graphene in field effect transistors.

CNT have excellent electrical properties including high carrier mobility, large field effect switching capabilities, and a long mean free path. Absent, however is an experimentally-backed model explaining contact-metal work function, device layout, and environment effects. To fill this void, we introduce a surface-inversion channel (SIC) model based on low temperature and electrical measurements of a distinct single-walled semiconducting CNT contacted by Hf, Cr, Ti and Pd electrodes. Anomalous barrier heights and metal-contact dependent band-to-band tunneling phenomena are utilized to show that dependent upon contact work function and gate field, transport occurs either directly between the metal and CNT channel or indirectly via injection of carriers from the metal-covered CNT region to the CNT channel. The model is consistent with previously contradictory experimental results, and the methodology is simple enough to apply in other contact-dominant systems.

In agreement with the initial contact theory above, we further develop a model explain I_{sd}-V_{sd} tendencies in CNT FETs. Using experimental and analytical analysis, we demonstrate a relationship between the contact metal work function and electrical transport properties

saturation current (I_{sat}) and differential conductance $\left(\sigma_{sd} = \dfrac{\partial I_{sd}}{\partial V_{sd}} \right)$ in ambient exposed CNT. A single chemical vapor deposition (CVD)-grown 6 millimeter long semiconducting single-walled CNT is electrically contacted with a statistically significant number of Hf, Cr, Ti, Pd, and Ti, Au electrodes, respectively. The observed exponentially increasing relationship of I_{sat} and σ_{sd} with metal-contact work function that is explained by a theoretical model derived from thermionic field emission. Statistical analysis and spread of the data suggest that the conduction variability in same-CNT devices results from differences in local surface potential of the metal contact. Based on the theoretical model and methodology, an improved CNT-based gas sensing device layout is suggested; a method to experimentally determine gas-induced work function changes in metals is also proposed.

Third, a performance analysis on CNT Schottky diodes using source-drain current anisotropy is explored. An analytical model is derived based on thermionic field emission and used to correlate experimental data from Pd-Hf, Ti-Hf, Cr-Hf, Ti-Cr, and Pd-Au mixed metal devices fabricated on one single 6 mm-long CNT. Results suggest that the difference in work functions of the two contact-metals, and not a dominant Schottky contact, determines diode performance. Results are further applied and demonstrated in a reversible polarity diode.

Next, we develop experimental processes to grow high quality monolayer graphene on Cu foil. Cu foil is pre-annealed and hand polished to increase Cu crystalline domain size and reduce surface roughness. This is done to reduce nucleation sites for graphene during CVD growth. After growth on Cu foil, the graphene is transferred to SiO_2 using a floating PMMA method described in section 3.2.2. Finally, the quality of the graphene is analyzed via Raman spectroscopy, optical imagery, and sheet resistance measurements.

After demonstrating the quality of the graphene film, we investigate the effect of UV irradiation of graphene, CNT, and graphene/CNT hybrids in an oxygen environment. Samples were irradiated by 254/185 nm UV light in an oxygen environment for up to two hours. Results suggest a unique method to generate graphene nanoribbons using aligned carbon nanotubes (CNT) as a graphene etch mask. Ambient and cryogenic G_{sd}-V_g measurements of resulting ultra-thin graphene nanoribbons show p-type character and field effect $G_{On}/G_{Off} > 10^4$.

TABLE OF CONTENTS

LIST OF TABLES

LIST OF FIGURES

PREFACE

As a graduate student, I have had the chance to work on many topics related to carbon nanotubes, graphene, and device physics. This work was greatly influenced by a number of current and past researchers in my field of study, and it is my sincere hope to one day influence others in the great manner that I have benefited.

On a personal level, the work in this thesis was not possible without the guidance and assistance from many impressive colleagues at the University of Pittsburgh (USA) and Sungkyunkwan University (Republic of Korea). I am sincerely thankful to Professor Minhee Yun at University of Pittsburgh and Professor Young Hee Lee at Sungkyunkwan University for the opportunity to perform research in two world-class laboratories. With Professor Yun as an advisor, I had the opportunity to travel across the globe for conferences, visit Korea six times during my graduate school career, and work on many stimulating research projects. Secondly, I want to thank committee members Dr. Guangyong Li, Dr. William Stanchina, Dr. Kevin Chen, and Dr. Alexander Star for their time as well as invaluable comments and suggestions. Thirdly, I want to thank past and current group members from Pitt: Jiyoung Huang, Dave Sanchez, Yushi Hu, Innam Lee, Michael Nayhouse, Alex "Sir Degas" Patterson; as well as from Sungkyunkwan: Dr. Seongyeol Jeong, Sanghoon Chae, Woojong Yu, Siyoung Lee, Huy Ta Quang, Jungjun Bae, Dr. Seongchu Lim, and Dr. DongJae Bae for their valuable contributions to my work. I also want to thank any and all my friends who were understanding and supportive. Last but not least, I owe

debt of gratitude to my grandmother, mother, and sister for all the help they have given me over

the last decade. I can never repay the help and support everybody has given me, but I hope to

inspire others to never give up on their dreams and strive for knowledge.

1.0   INTRODUCTION

1.1   CARBON NANOMATERIALS

Carbon nanomaterials are some of the most of the most frequently studied materials in the literature today. The field continues to grow in research popularity in terms of publications more than 20 years after Iijima and Bethune's TEM analysis of single-walled CNT (SWCNT) in 1993,[1,2] and nearly 30 years since the first preparation of buckminsterfullerene renewed interest in carbon.[3] In fact, prior to the experimental demonstration of buckminsterfullerene, carbon research centered primarily around two other popular allotropes of carbon: diamond and graphite. Diamonds are the hardest known natural mineral known equally for its industrial applications as for its beautiful light dispersive properties. Without doping, diamond is typically an insulator with a bandgap of 5.5 eV. Due to rarity and cost, it is not useful for semiconductor devices and electrical applications. Graphite, however, is a layered structure wherein each layer has carbon atoms arranged in a hexagonal lattice. Naturally occurring, graphite is useful industrially as a lubricant, in batteries, and is perhaps most commonly known as "pencil lead". Electrically it is a semimetal with highly anisotropic conductivity due to poor interlayer carrier transport. To understand what makes CNT and graphene special when comparing to these former famed carbon allotropes, one must consider dimension. The limited dimensionality combined with the ultra-strong C-C Sp^2 hybridized bonding in both graphene and CNT make them attractive for

1

electrical, mechanical, chemical, and various theoretical purposes. While the primary focus of this thesis is the electrical characterization of novel CNT and graphene devices, the mechanical and chemical properties of these special carbon allotropes are equally as unique and are widely discussed elsewhere in the literature.

1.2   THESIS ORGANIZATION

Chapter 2 begins by introducing interesting and related background work on CNT and discusses the motivation for my work. General electrical properties and interesting physical properties of CNT are also discussed. Experimentally, section 2 covers all of the CNT-related work we have performed in the past 4 years. This includes:

-Physical model for the contact barriers at carbon nanotube-metal interfaces

-Derivation and experimental fitting of CNT I-V data to a novel model based on thermionic field emission

-Derivation and experimental fitting of I-V data from CNT with hetero-metal contacts to determine voltage and work function dependencies

Chapter 3 begins with background work and motivation for the use of graphene in electronic devices. The plethora of interesting physics relating to graphene is also discussed. Experimentally, chapter 3 covers all graphene related work including growth, substrate transfer, and characterization. Noteworthy success' in this research area includes:

-Growth of high quality monolayer graphene

-Novel fabrication method for sub 5 nm graphene nanoribbons

-Demonstration of room-temperature on/off field effect switching ratios greater than 10^4 in fabricated graphene nanoribbon field effect devices.

2.0 CONTACT METAL-DEPENDENT ELECTRICAL TRANSPORT IN CARBON NANOTUBES

2.1 BACKGROUND

CNTs are a unique platform for investigating chemical,[4-6] biological,[7] electrical,[8-13] mechanical,[14-16] and interdisciplinary concepts.[17-20] Underlying its ubiquitous interest in the scientific community is the quasi 1-dimensional hexagonally aligned lattice structure held together with strong sp^2 bonding. This bonding alignment, with three nearest neighbors to every carbon atom, creates a structure that is both mechanical stable and electrically conducting. CNT come in a variety of flavors that are differentiated by their Chirality, which is explained further in Appendices A and B. CNT can also be classified by the number of concentric walls of carbon the tube is composed of. SWCNT have a single atomic layer of carbon atoms wrapped in a cylinder, typically with diameter less than 3 nm. Multi-walled CNT (MWCNT) can have diameters from a few nm up to nearly 100 nm.

Physically, the ultimate tensile strength of MWCNT is estimated to be at least 63 GPa, although this value is considered a lower bound for ultimate strength.[21] SWCNTs have a lower bound on ultimate strength of 100 GPa and a theoretically predicted strength around 1 TPa.[22] Axial compressive strength or strain has yet to be measured, although this value may yield even greater values due to the cylindrical structure. This strength makes CNT ideal for improving

physical and electrical properties in composites.[23] CNTs can also be purchased as ultra high resolution tips for scanning probe microscopy, which is perhaps the only commercialized application at this time.[19]

In CNT, the low-energy electrical transport is almost exclusively dominated by the out of plane π, π^* states, while the in-plane σ states only effect carriers with energy greater than 4 eV, exceeding realistic room temperature energies.[24] This permits us to derive an accurate energy dispersion in a CNT band structure using a simple tight binding model of graphene derived in Appendix A. We observe from the tight binding model that an isolated sheet of graphene is a semimetal (zero band gap semiconductor) where conduction and valence bands touch only at the K-points. Imposing boundary conditions due to the finite CNT circumference reduces the allowable k values to a quantized number of energy bands. The existence of an electronic bandgap is determined by whether one of the allowable k values crosses through a K-point. Further details regarding the relationships between metallicity and diameter can be found in both Appendix A and Appendix B.

In metal CNTs (allowable k crosses the K point), the low energy dispersion is linear with transport governed by filled π and unfilled π^* bonding states. With a mean free path often greater than a micron for low-energy carriers,[25] transport can be ballistic over long length scales. Assuming ballistic transport in a device, the conductivity of metallic CNTs is determined using the 1-D Landaur-Büttiker formula: $G = \dfrac{2e^2}{h} NT$ where h is Planck's constant, N is the number of conducting channels, and T is the transmission probability at the contacts. Assuming N = 4 when accounting for spin degeneracy and two conducting channels, and T =1 (reflection-less contacts), the minimum possible resistance for a CNT is ~6.5 kΩ. This can be interpreted to mean, and is experimentally proven, that regardless of channel length, the lowest resistance for a single CNT

device is approximately 6.5 kΩ.[25] In ultraclean samples, particularly at low temperatures, evidence for quantized conductance manifests step-like conductance properties as seen in the literature. [26] Metallic CNT are also an excellent platform for investigation of quantum mechanical transport effects. Phenomena such as Anderson localization,[27] Aharonov-Bohm Oscillations due to the cylindrical nature of CNT (this was observed in metallic MWCNT),[28] as well as a low temperature Lüttinger-Liquid transition have been observed.[29-33] An open question in CNT physics is the manifestation of superconductivity[34] which was earlier observed in SWCNT ropes[35,36] but is difficult to explain theoretically.

Semiconducting CNTs, on the other hand, have zero density of states at the Fermi level and can have an optical band gap approaching 1 eV for very small diameters.[37] Strong exciton binding energies reduce the effective electrical bandgap, however and leads to novel screening effects.[38-40] Optically, semiconducting CNT have strong absorption due to Van Hove Singularities in the density of states. This enhanced optical absorption led to significant Raman spectra studies,[41-45] and further enabled observation of optical phenomena such as the Stark Effect.[46,46] For all nanotubes, but particularly semiconducting CNT, carrier transport is overwhelmingly dominated by the metal-CNT contact effects. In discussing the Landaur-Büttiker formula for metal tubes, it was simply assume that the transmission coefficient T = 1. In reality, reflection-less contacts are extremely difficult to fabricate due to resist residue, metal oxidation, [47] CNT defects, environmental effects such as humidity,[48] and poor metal wetting to the CNT surface.[49] This innate contact energy barrier to semiconducting CNTs in particular has allowed single-electron transistor operation[50,51] and observation of the Coulomb blockade[31,52,53] in simple back gated field effect transistor devices. In fact, semiconducting CNTs display remarkably high field effect mobility[11,12] which allows for excellent transistor operation. As such,

in section 2 of this thesis, various contact-effects associated with the use of CNTs in field effect and diode devices will be considered. As part of this section, the effect of applying different metal species to the same tube will be investigated.

2.1.1 Motivation

Carbon nanotube field effect transistors (CNT-FETs) have high current-carrying capability,[54] on/off ratio greater than 10^6,[55-57] and switchable polarity dependent upon environment and chemical treatment.[58,59] Rapid optimization and performance enhancement in CNT-FETs has occurred[24]. Nevertheless, the physics and the underlying mechanisms for transport are still incomplete. For instance, experimentally distinguishing energy band alignment at the metal-CNT contact has proven to be exceedingly difficult[60,61] and scarce experimental evidence exists in the form of Schottky barrier heights. Initially, it was believed that gas adsorbates in the CNT channel induces a charge transfer from CNTs to adsorbates, resulting in p-type conduction in ambient measurement conditions.[62,63] However, more recently it was argued that the adsorbate-induced planar dipole layers at the interface are the key factor for determining the majority carrier.[64]

The model of the induced dipole layer at the interface generally explains the CNT device operation. For Au contacts, conduction variations are attributed to the induced dipole moment due to oxygen adsorbates at the interface. In the absence of oxygen, Au electrons are spilled over to CNT. In the presence of oxygen however, strong charge transfer occurs from Au to O_2, forming a dipole opposed to the spillover.[65] This dipole layer depletes the CNT, pulling the Fermi level (E_F) of CNT towards the valence band maximum. Similarly, in the case of Ti, a commonly used contact metal, oxygen-induced surface potential variations were introduced to explain the dominant p-type behavior.[64] However, contrary to these earlier reports, McClain *et al.*

7

observed that under atmospheric O_2 exposure, the range of off-state gate bias was extended significantly into the n-region until the electron conducting on-state weakly appeared.[66] This occurrence cannot be explained by a planar dipole model, nor is it consistent with earlier oxygen doping model. The formation of dipole layer at the interface (due to oxygen in this case) should give rise to a threshold voltage change exclusively. Conversely, increases in dopant (oxygen) concentrations should be followed by a significant increase in off-current[67] in contrast to the CNT devices which often exhibits the reverse phenomenon. In this proposal we seek to solve these issues via introduction of a new theory based on the concept that the shortest distance is certainly not always the path of least resistance. In a circuit with multiple current paths, carriers will always traverse the path with the lowest resistance, even if the physical length of such a path is longer. When contacted with low work function metals, the electron contribution of the sub-surface metal-covered CNT is often neglected because of the longer conduction pathway compared to that of the metal edge to CNT path. As a result, the interface-dominant conduction of the surface dipole model is inconsistent with conduction in extremely low work function metals where surface-passivated metal contacts with work functions $\ll 4.0$ eV have usually been required for stable electron conduction.[57,68] These inconsistencies (as well as our observations in this report) suggest that an updated model is required to accommodate such complications in the transport phenomena at the metal-CNT contact.

Knowledge of the aforementioned lack of measured Schottky barrier magnitudes is crucial to development of said model. For example, the magnitude of the Schottky barrier over a range of applied gate bias (V_g) will provide the energy band offsets and alignments, while the slope of barrier versus gate bias will provide information with respect to the nature of the dominant carrier (electron, hole, or both). These measurements must be performed for devices

located on a single, distinct, CNT, since contact Schottky barriers on different CNTs and results from different groups may also induce further complications as a result of the variable diameter CNTs and fabrication conditions adopted. For consistent data acquisition and clear understanding of results, different metal contacts must all be fabricated on one single-walled CNT, using identical fabrication conditions and testing environment.

From a device-level perspective, the purpose of this thesis is to describe the current-voltage characteristics of a CNT-FET with a known metal. This type of knowledge has been gathered for materials such as silicon and III-V semiconductors over the last half century, while little data exists for CNT or many other nanostructures. For instance, CNT FETs are unique because the current modulation in CNT-FETs is dominated by field-adjusted energy barriers at the contacts,[60,62,64,69,70] in contrast to Si-based devices.[71] Without chemical treatment, the metal-contact work function determines the CNT device polarity,[10,63] applicable in advanced adaptive logic circuits[56] and dopant-free CMOS circuitry.[57,72,73] However, previous attempts at understanding the contact dependences of CNT-FETs[66,68,74,75] are complicated by usage of CNT with varying diameter and the lack of an analytical CNT transport model. Therefore, we use systematic experimental and theoretical analysis to relate metal-contact work function and electrical transport properties saturation current (I_{sat}) and differential conductance $\left(\sigma_{sd}\right)$ in CNT-FETs incorporating a theoretical model analytically derived from thermionic field emission. Previous variation-limitations are overcome with measurement, statistical analysis, and data fitting from ~100 Hf, Cr, Ti, Au, and Pd contacts on a single CNT. Further analysis suggests the model is applicable for quantitative nanotube-based gas sensing, and for noninvasive metal work-function measurement.

CNTs have been implemented into steadily more advanced logic circuits beyond FET devices,[56,72,73,76-78] and with advances in growth and positioning,[79-82] and better contact engineering,[60,83] scalable CNT-based logic circuits could be feasible within the next decade. CNT-based Schottky diodes are of particular interest due to simple fabrication and promising high-frequency characteristics.[84] Hence, the literature is littered with individual diode devices utilizing mixed-metal contacts to CNT.[84-88] The diode-like characteristics of these mixed-metal devices is suggested to result from one contact having ohmic properties (typically Pd or Ti) and the other being Schottky in nature. Innately this assumes that the energy difference between the contact-metal work function Φ_m and CNT Fermi level (E_F) determines the device current-rectifying ability. However, the validity of this assumption has not been systematically tested and no model has been developed to explain the Φ_m-dependent rectifying capabilities.

Using experimental data fitted to a derived theoretical model we consider this issue and demonstrate that in hole-conducting devices where both contacts are Schottky in nature, the difference in Φ_m $(\Phi_m = \Phi_{m1} - \Phi_{m2})$ determines the rectification, not the energy band alignment at a dominant Schottky contact. This result is applied to demonstrate a reversible-polarity diode with bias-dependent rectifying characteristics.

2.1.2 Experimental Details

2.1.2.1 Carbon Nanotube Growth

Ultra long aligned CNTs utilized for devices in sections 2.2-2.4 were synthesized by laminar flow TCVD with $FeCl_3$ (Sigma Aldrich) in ethanol as a catalyst. After cleaning Si/SiO_2 (300 nm) wafers with oxygen plasma and acetone/IPA/DI water, the edge of the samples were dipped in

0.001 M FeCl$_3$/ethanol. The samples were then dried in air for 5 minutes before loading onto a quartz sample holder, which was then placed inside a 2 cm diameter quartz tube to reduce turbulence and promote laminar flow for increased CNT length.[82] The 2 cm inner-diameter tube is then placed inside the chamber on alumina stilts so that the catalyst-coated edge facing towards the gas inlet. This orientation is done such that long tubes can nucleate from the catalyst near the edge. Growth was performed in atmospheric pressure, firstly by purging the chamber with 300 sccm of 99.999% Ar gas, followed by maximum temperature ramp up to 900° C while flowing 100 sccm H$_2$ gas. At 900° C, the FeCl$_3$ catalyst is reduced and decomposes into Fe nanoparticles. After holding the temperature at 900° C for 10 minutes, the furnace is again max-ramped to 1000° C for growth of the CNTs. CNTs were then grown for up to 30 minutes while reducing Ar flow to 0 sccm, and increasing H$_2$ and CH$_4$ flow to 16 and 14 sccm, respectively.

To confirm that the flow inside the inner tube was indeed laminar in nature, a Reynolds number < 2300 must be demonstrated, with smaller numbers indicating a more stable flow. The Reynolds number is the figure of merit for determining the turbulence of flow, and is defined by

$R_e = \dfrac{\rho \upsilon d}{\mu}$, where ρ is the gas density, υ is flow velocity, μ is the viscosity as a function of temperature, and d is the tube inner diameter. At 23 K, $\rho \sim 0.66 \, kg/m^2$ for methane, and

$\rho \sim 0.09 \, kg/m^2$ for hydrogen at room temperature and $0.152 \, kg/m^2$ and $0.02 \, kg/m^2$ at 1000° C, respectively. Flow velocity is equal to the volume flow rate (m^3/s) divided by the large outer tube (d = 5 cm) cross section area. Viscosity was calculated as a function of temperature using the

Sutherland formula $\mu = \mu_0 \left(\dfrac{T_0 + C}{T + C} \right) \left(\dfrac{T}{T_0} \right)^{3/2}$.

A summary of the calculated and empirical values for the CNT growth conditions are shown in Table 1. The resulting Reynolds number ~.03 indicates an extremely stable flow that will promote tip growth due to a dominance of the CNT/catalyst buoyancy force due to a temperature gradient within the small tube.[89]

Table 1. Reynolds number calculation data for methane gas in a tube furnace

Parameter	T = 27° C	T = 1000° C
μ_0	11.2 $\mu Pa \cdot s$	x
C	169	x
T_0	T = 27° C	x
ρ	$.66 \left(kg / m^2 \right)$	$.152 \left(kg / m^2 \right)$
μ	11.2 $\mu Pa \cdot s$	31.84 $\mu Pa \cdot s$
υ	X (no methane flow)	$2.8 \cdot 10^{-4}$ m/s
R_e	x	.0267
Laminar Flow?	-	Yes
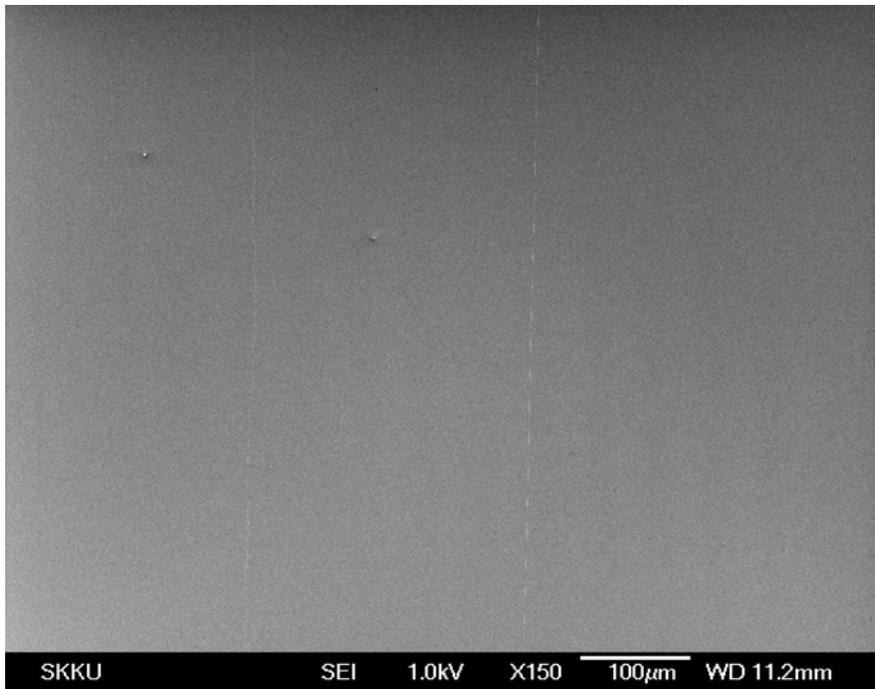
Figure 1. SEM image of ultra-long aligned CNT grown via laminar flow TCVD.

For growth times between 15-30 minutes, no noticeable differences in CNT length and quantity were observed, although longer times occasionally resulted in deposition of amorphous carbon on the SiO_2 surface. Within this range, conditions were ideal for centimeter or longer (substrate limited) aligned CNT growth, with sparse CNT spacing ~100 µm. Typical results for CNT growth are shown in the SEM Image in fig. 1.

2.1.2.2 Device Fabrication

After CNT growth and transferred with the floating PMMA-Hf etchant method, e-beam lithography (EBL, Raith E-Line) patterning was used to define alignment markers that were subsequently etched into the SiO_2 with 9:1 buffered oxide etch. Using a scanning electron microscope, we first examined near the catalyst region to locate a desirable CNT. As the CNT are strongly aligned, 1 mm steps were taken along the same CNT to denote its exact location without exposing the future device regions to the electron beam. To contact the CNT with metal electrodes, hundreds of large probe-able pads (modular design) were fabricated with lead lines approaching within ~15µm of the CNT. Individual metal contact species were then patterned with EBL, metal deposited by e-beam evaporation, and lift-off performed in 45° Celsius acetone. Post fabrication, CNT-FETs regions were covered with optical photo resist and the sample etched in 100-150 W O_2 plasma to remove other CNTs. Typical device is shown in figure 2.
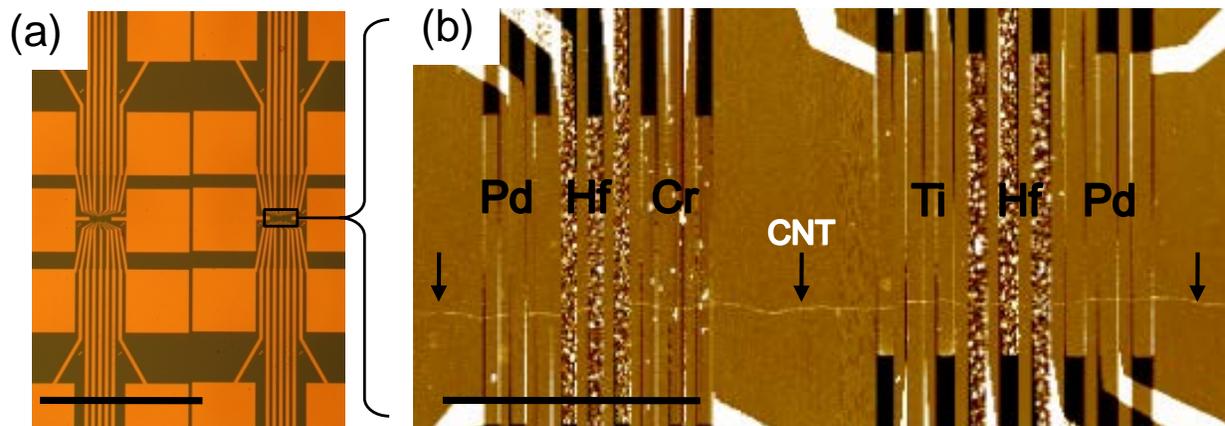
Figure 2. Optical image (a) and AFM image of zoomed in region (b) showing the device layout used for the CNT experimental section of this proposal. Scale bars are 1 mm and 20 microns respectively. Arrows denote the CNT.

2.1.2.3 Schottky Barrier Measurements

Barrier heights were calculated by measuring devices in a closed cycle refrigerator for $150 < T < 300$ K (Although Schottky barrier estimations only utilized the temperature range 250-300K). Richardson plots were generated for all gate biases. By plotting $\ln\left(I_{sd}/T^2\right)$ vs. $\frac{1}{T}$ at specific V_g and V_{sd}, the slope of the resulting plot is equal to the Schottky barrier height at that point according to the equation,[71]

$$\ln\left(I_{sd}/T^2\right) = \ln(A^*) - \frac{\Phi_b}{kT} \tag{2.1}$$

After extrapolation of the barriers, we can find the zero-bias barrier height $\left(\Phi_0\right)$ by plotting Φ_b as a function of $\sqrt{V_{sd}}$ according to the equation:

$$\Phi_b = \Phi_0 - A\sqrt{V_{sd}} \tag{2.2}$$

The y-intercept provides an estimation of Φ_0 which does not incorporate image force lowering.

2.2   ANOMALOUS SCHOTTKY BARRIERS AND CONTACT BAND-TO-BAND

TUNNELING IN CARBON NANOTUBE TRANSISTORS

2.2.1   Introduction

On a single ultra long 1.7 nm diameter semiconducting CNT[81] with an estimated energy gap,

$E_g \approx 0.65\,\text{eV}$,[37] we fabricated FETs with Hf, Ti, Cr, and Pd contacts by e-beam lithography.

These metals were chosen because they offer a wide range of work functions (3.9 (Hf) - 5.1(Pd)).

Devices had 1 µm channel length and were limited to a 40 micron region of the same CNT to

further minimize the risk of diameter change. Using temperature-dependent characteristics of

thermionic emission, we fit the subthreshold p-type and n-type regions of operation with the

basic Schottky model. Richardson plots were constructed and the model was fit for 250 K < T <

300 K to extract zero-bias barrier height estimations.

2.2.2   Results and Discussion

The activation energy method explained in section 2.1.2.3 was used to extract Schottky barrier

heights from I_{sd} in terms of gate bias (fig. 3). Hole barriers were extracted as a function of

applied gate bias (V_g) for Pd and Ti (fig. 4a), and electron barriers for Hf and Cr FETs (fig. 4b).

From these plots we observed that: (i) A clear exponential relationship between barrier height

(Φ_b) and V_g, and (ii) $\dfrac{\partial \Phi_b^{holes}}{\partial V_g} > \dfrac{\partial \Phi_b^{electrons}}{\partial V_g}$. Later these relationships will further confirm the

validity of the SIC model. Our purpose of the exponential fittings of fig. 4 is to obtain Schottky

barrier height at $V_g = 0$ and determine the E_F of the CNT. Ambiguity occurs in the case of Cr and

Hf, where near $V_g = 0$, carrier type conversion occurs. We assume that for Cr and Hf at $V_g = 0$,

the carrier is n-type. The barrier height for electron carriers is obtained by extrapolating the

linearized log-scale relationships to $V_g = 0$ as shown in Fig. 4b (trend lines). The estimated

$\Phi_b(V_g = 0)$ can be used to extract a CNT bulk E_F position and subsequent band diagram. All

estimations of E_F should be equivalent due to the common CNT and environment of each device.

The estimations for E_F are extracted by applying the unpinned level assumption and Schottky

Mott relationship ($\Phi_b^{electrons} + \Phi_{metal} = E_F$ and $\Phi_{metal} - \Phi_b^{holes} + = E_F$ where Φ_{metal} denotes the

metal work function).[71] In the case of Hf, the extrapolated barrier height is far different from the

measured barrier height at $V_g = 0$, due to the switch of majority carrier. Common work functions

are assumed for each metal, including: Ti = 4.6 eV,[90] Cr = 4.4 eV,[91] Hf = 4.0 eV, and Pd = 5.0

eV, explanations for which are found in Table 2. For electron barriers, the extrapolated E_F values

are 4.55 eV for Hf and 4.56 eV for Cr. For hole barriers, $E_F = 4.5$ eV for Ti and 4.9 eV for Pd. +

Table 2. Metal work functions

Metal	Work function Range	Common Value	Explanation
Hf	3.9 - 4.0	4.0	Minimal literature exists on the ambient measurement of work function for Hafnium. Therefore we utilized the theoretical value of 4.0.
Cr	4.1 – 4.5	4.4	Effect of hydrogen and oxygen exposure on the ambient work function measured by the Kelvin method. A large group of samples was measured in ambient first, and had a large grouping between 4.3 – 4.52. We averaged these values to assume $\Phi_m = 4.4$.[2]
Ti	4.5 – 5.3	4.6	Work function was measured as a function of oxygen exposure by Jonker *et al*. Initial clean surface value was 4.58 $\pm$ 0.05 eV. With maximum value observed was an oxygen saturated surface with $\Phi_m = 5.3$. We assume a value of 4.6 since the reference suggests that significant oxygen loading is required to raise the surface potential[90].[3]
Pd	4.9 – 5.2	5.0	Kelvin force microscopy has shown that Pd on Au has a surface potential difference of less than 0.1 eV, thus giving our expected lower limit of about 4.9 or 5.0 eV.[4] Gu *et al* measured Pd work function of 5.15 on atomic layer deposited HfO_2.[5]
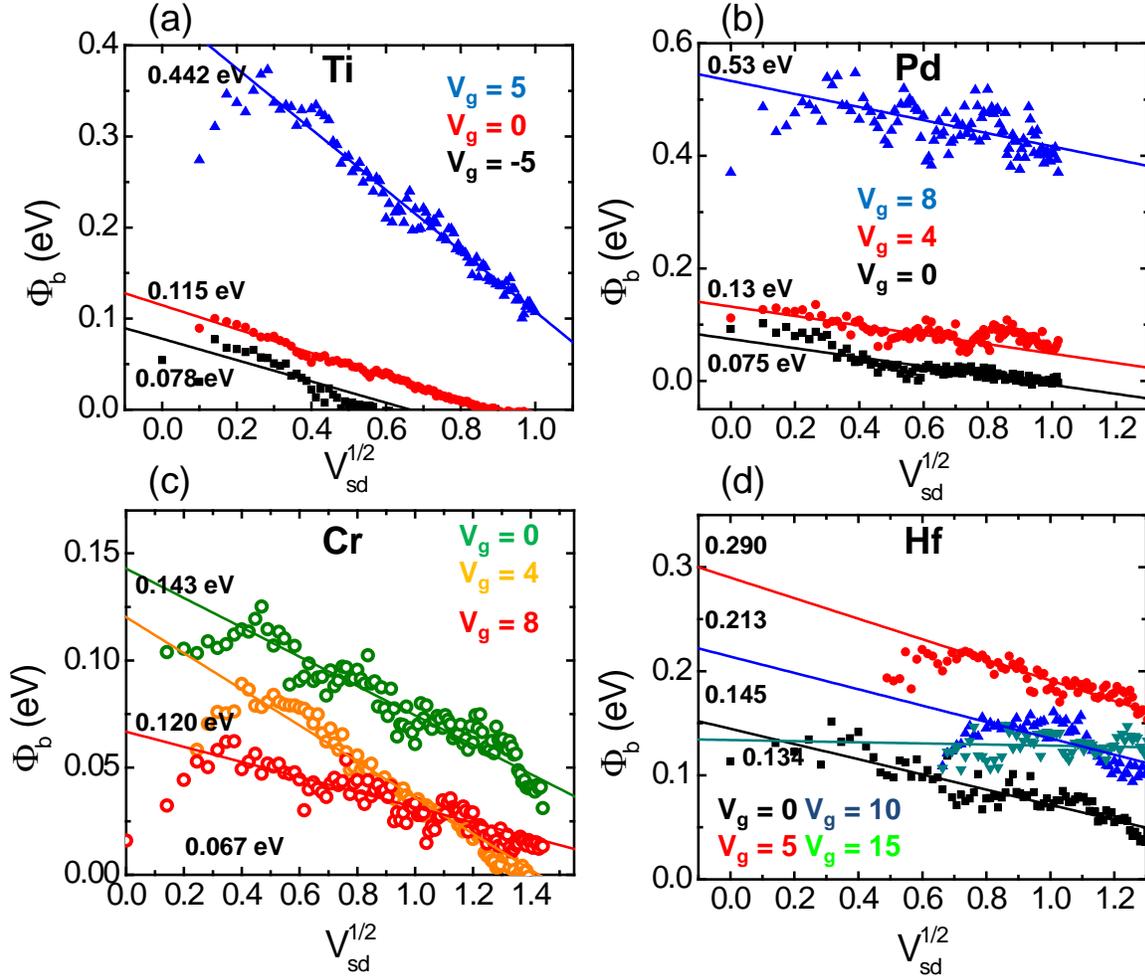
Figure 3. Schottky barrier height measurements for metals (a) Ti, (b) Pd, (c) Cr, and (d) Hf. Ti and Hf measurements were performed for the hole-carrier energy barriers while Cr and Hf measurements were only possible for electron barriers. For Ti and Pd, Φ_b vs. $\sqrt{V_{sd}}$ contains no intercepting curves and each plot contains steadily increasing slope as V_g was increased. Cr and Hf fittings have multiple intercepting curves and near zero slopes, particularly as V_g is increased positively. The actual barrier is the CNT inversion region, and unlike a typical Schottky-type barrier it is possible to have little dependence on applied V_{sd}.
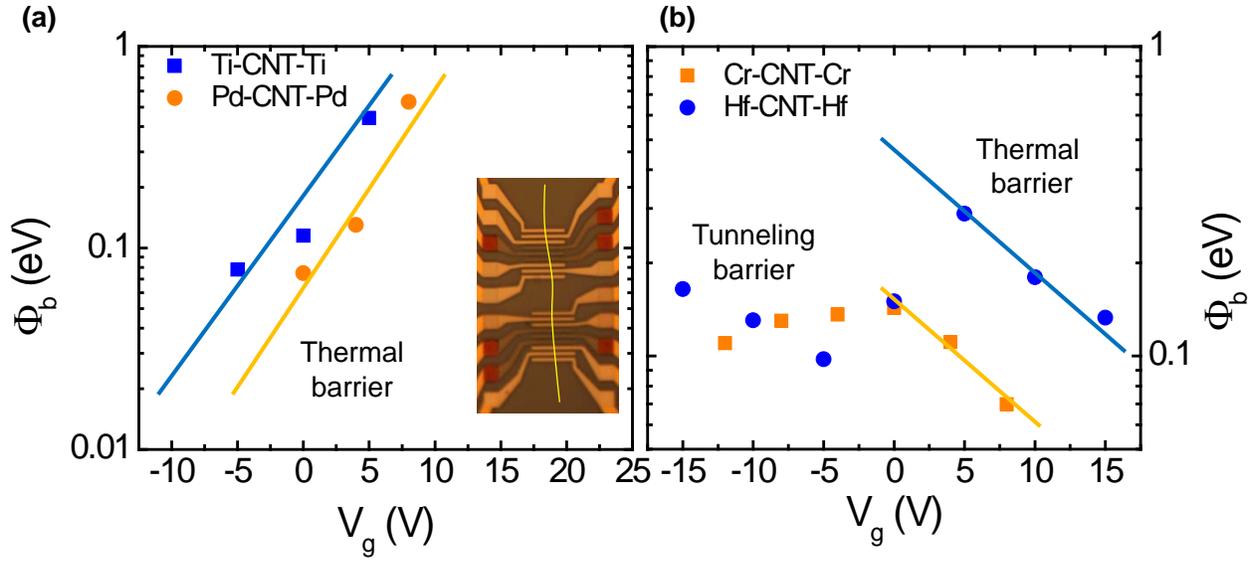
Figure 4. (a) Schottky barriers extracted by using thermionic model and activation energy measurements. Ti (square), Pd (circle) barrier heights as a function of gate voltage. Inset is an optical image of the device layout used for measurements. The solid line denotes the location of the single CNT used for all the measurements with four different metal electrodes. (b) Schottky barrier heights for low work function metals Cr (square) and Hf (circle). The solid lines indicate least square fit of the data in the range.

A few observations can be made from the source-drain current (I_{sd}) and Schottky barrier height as a function of V_g as shown in Fig. 5. I_{sd} is inversely proportional to the barrier height. Hole currents are dominant in all the devices regardless of metal contact type and the onset of hole current is $V_g \geq 0$ for all the devices. Hence, E_F of the CNT should be significantly greater than 4.8 eV (electron affinity + $E_g/2$), which is the estimated intrinsic E_F of a 1.7 nm CNT.[37] The observed E_F values above are clearly underestimated and suggest an unusual band alignment near the contacts. We emphasize that this underestimated E_F does not result from inaccurate measurements, since any underestimation of the barrier height violates the Schottky Mott relationship as $\Phi_b > E_g$ (particularly for the Hf case).[71]

Careful examination of Fig. 5 gives insight for different transport phenomena among the metals. For example, Pd has the largest work function, and as expected, has the largest threshold voltage of the metals (Fig. 5a). In the case of Ti (Fig. 5b), weak ambipolar behavior is observed and more importantly, similar n-type and p-type currents are observed at equal Schottky barrier heights. This suggests that Ti transport has similar properties for both electrons and holes (note that Schottky barrier measurements are offset by gate sweep hysteresis). On the other hand, Hf has the lowest work function and yet has negligible electron current for positive V_g (Fig. 5c). The Schottky barriers for Hf closely resemble those of Ti for electron conduction, and are in fact smaller for hole conduction. Measurement yielded nearly constant barriers of 0.1 - 0.15 eV for $V_g < 0$ V in the case of Hf. It is noted that the hole current is extremely low in spite of low Schottky barrier height and high source-drain bias (V_{sd}). This suggests that Hf has a very thick energy barrier compared to that of Ti, and furthermore, for Hf the electron barrier is thicker than the hole-type barrier. Another intriguing phenomena for Hf near $V_g = 0$ is the existence of a region of negative transconductance, as shown in Fig. 5d. This characteristic usually occurs in

the case of BTB tunneling[71] and during filling of multiple energy bands during transport.[92] However, multiple energy band conduction is ruled out near $V_g = 0$ V, since E_F is located mid-gap. The hump was not visible for $V_{sd} \ll 3$ V but appeared in all three Hf devices (same CNT) tested in vacuum with $V_{sd} = 3$ V (Fig. 6). This was only observed in the case of Hf metal, not others.
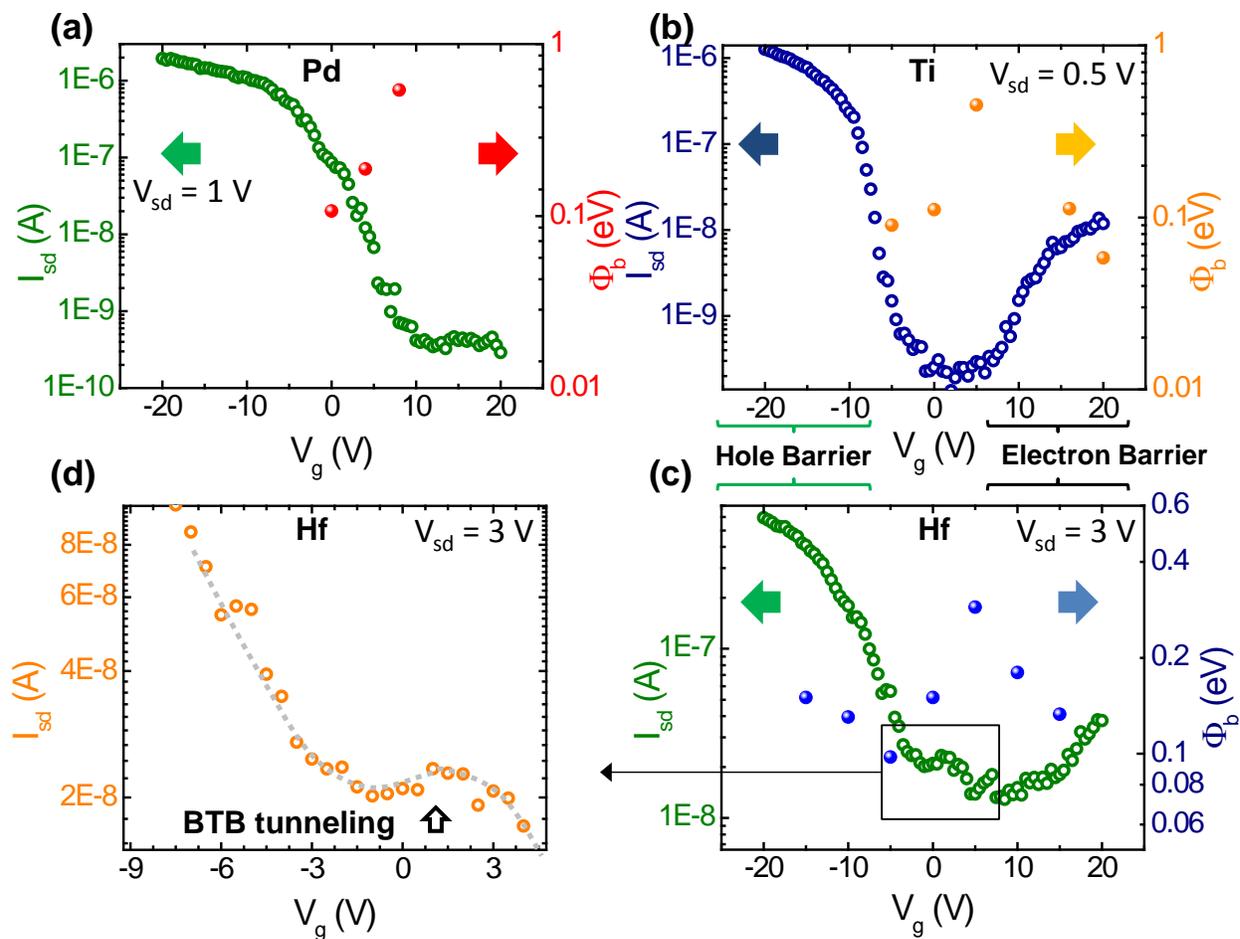
Figure 5. The measured V_g - I_{sd} characteristics and the corresponding barrier height for a given gate bias from (a) Pd p-type device, (b) hole dominant ambipolar Ti device, (c) hole-dominant ambipolar Hf device. Note that in this case $V_{sd} = 3.0$ V, and (d) negative transconductance at the onset of hole conduction, which is evidence of high source-drain bias BTB tunneling at $V_{sd} = 3.0$.
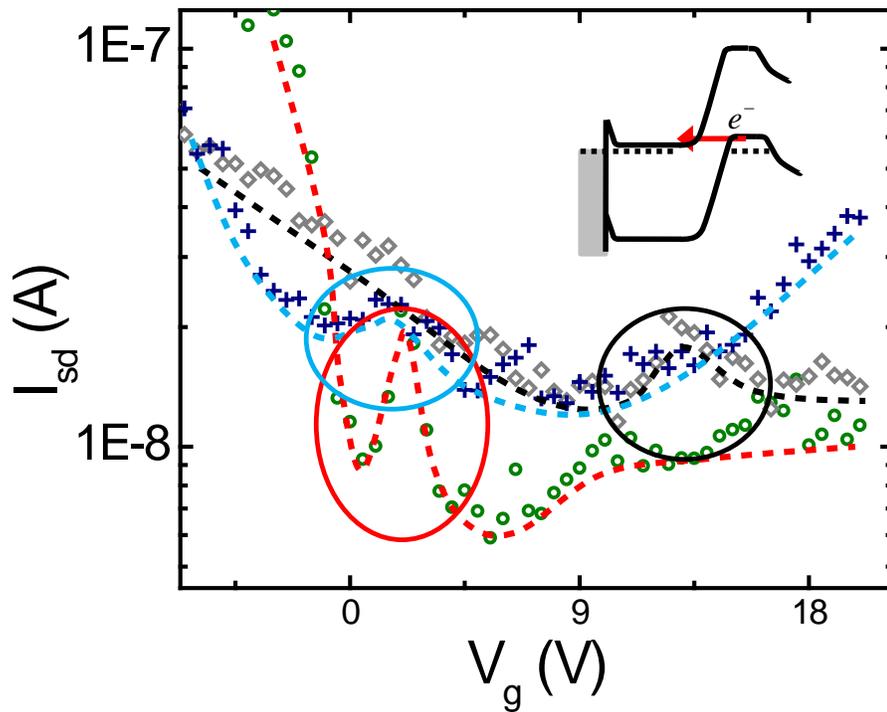
Figure 6. I_{sd}-V_g sweeps at 300K vacuum conditions for different Hf-CNT-Hf transistors on the same CNT. Negative transconductance at the onset of p-type behavior denotes BTB tunneling of minority electrons from the CNT inversion region valence band to the conduction band of the metal-covered CNT. The threshold voltage difference for the above devices is due to variations in work function of the contact materials (different contact crystal face or variation of environmental exposure). Circles denote the location of the BTB tunneling region. Inset shows band diagram according to the SIC model.

Using the above Schottky barrier measurements, metal dependent transport characteristics, and the BTB phenomenon we propose the SIC model and then explain details of the transport phenomena according to this model. The first SIC model presumption is the formation of a CNT inversion layer at the junction. The CNT-metal contact region is strongly affected by gas adsorbates and oxide growth, particularly for low-work function metals, where oxygen exposure can increase surface potential by an eV or more.[90,93] Experimental evidence in the study of oxidation also shows that electric fields enhance native oxide growth. This type of electric field-induced growth produces non-stoichiometric metal oxide species and a reduced activation energy for physisorption or chemisorption at the CNT/metal that can enhance the charge transfer with the CNT.[94] Large field strengths are possible in the local region around the CNT-metal contact to enhance the thickness of oxide or oxygen absorption depth. Therefore, in the case of oxygen exposure, the surface dipole induces electron transfer from the CNT to the metal and typically produces a strongly p-type region that we refer to as the CNT inversion layer. E_F in this region is difficult to modify, and will require large gate fields to overcome the screening of the surface dipole. The second presumption is the formation of additional conduction path through the CNT located under the metal electrode. This CNT region underneath the metal contact is completely resistant to gate fields due to the metal screening, and E_F remains unchanged with applied V_g. Due to enhanced growth of a surface oxide layer, which is particularly thick in the case of Hf, the subsurface metal region is protected from adsorbates and will reflect pristine conditions.

Figure 7a shows a schematic of our SIC model for particularly Hf case (low work function). In the metal-covered CNT region, charge transfer from the metal to the CNT occurs, favoring electron conduction. The direction of the charge transfer of the CNT inversion region is

26

opposite to that of metal-covered CNT region, favoring hole conduction. This resulting energy band alignment resembles an inversion layer in a metal oxide semiconductor device. To demonstrate the validity of the SIC model, we will explain conduction phenomenon as a function of gate bias. In fig. 7a, the off-state is assumed to occur around $V_g = 0$, although this will depend on gate dielectric and trapped oxide charge. The electron barrier is in agreement with the previously extrapolated value of 0.55 eV. The measured barrier is 0.2 eV with respect to the direct hole conduction, as shown in the schematic.
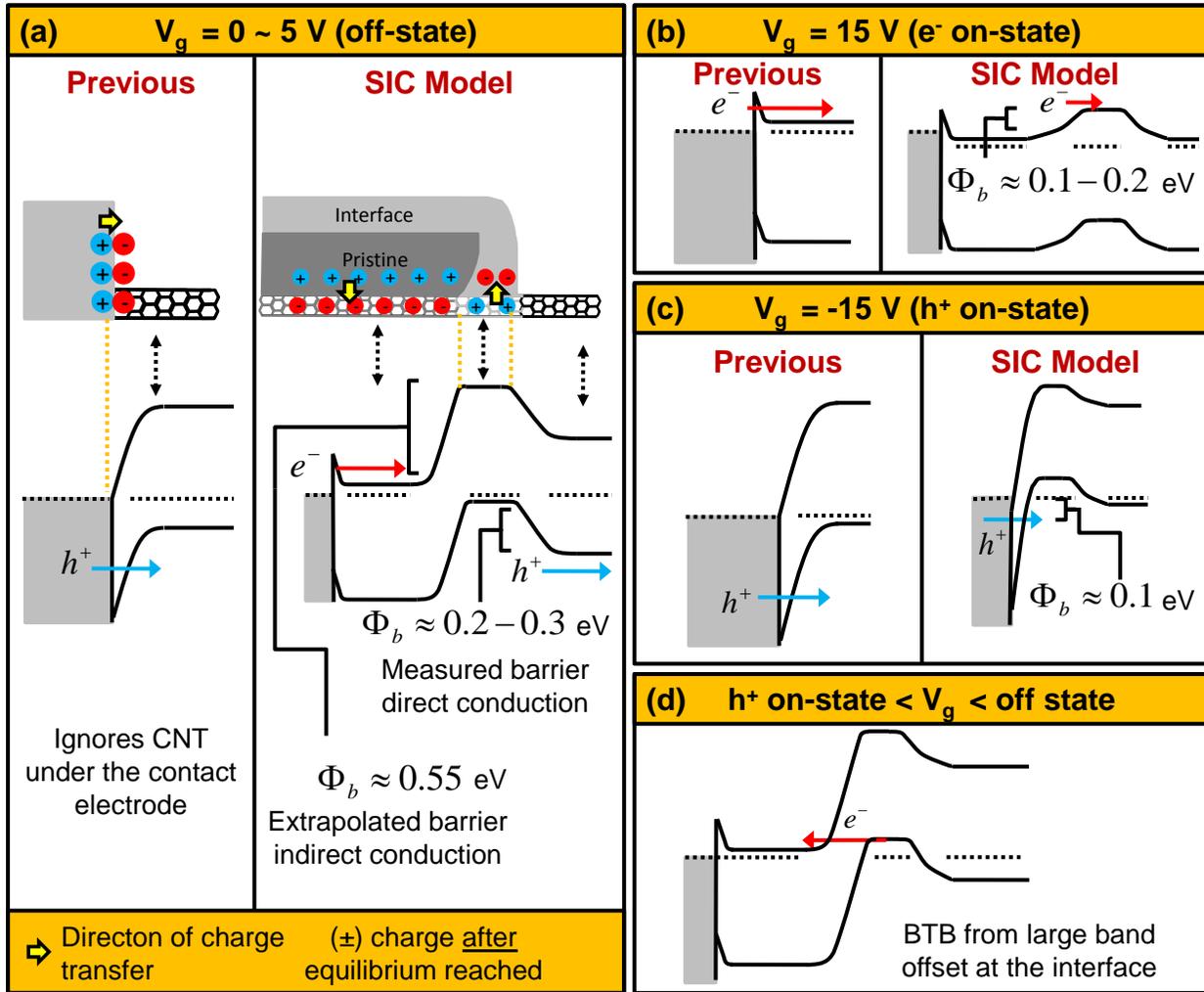
Figure 7. (a) Top panels show the charge transfer between CNT and Hf (low work function metal) with exposure to oxygen. The bottom panels show comparison of typical band diagram of surface dipole layer model and our SIC model. In the surface dipole layer model, band bending occurs due to the formation of dipole layer and the tunnels through the regular Schottky barrier. In SIC model, three distinct CNT regions are formed: metal-covered CNT, CNT inversion layer, and intrinsic channel. (b) Band diagram of electron conducting on-state at V_g = 15 V. Electron barrier between the metal-covered section of the CNT and inversion CNT region dominates conduction. (c) Band diagram of hole conducting on-state at V_g = -15 V. Tunneling dominates and transport is governed by direct injection of holes from the metal. (d) The band diagram at a gate bias of intermediate region to show negative transconductance due to BTB tunneling resulting from a large band offset at the interface.

Electron conduction is favorable at V_g = 15 V (fig. 7b), because the metal-covered CNT region has a favorable energy line up for electron conduction with the CNT channel. The "Schottky" barrier observed in the measurements for electron conduction is actually the thick surface inversion layer. The barrier thickness suppresses tunneling current, in agreement with our observations of low electron current in this region. To pass from the electrodes to the CNT, carriers travel first from the metal into the metal-covered CNT, and then traverse the thick inversion layer barrier before entering into the CNT channel. This will be referred to as "indirect transport". Carriers travelling directly from the metal, across the inversion region and into the channel will be referred to as "direct transport". On-state hole transport (at V_g = -15 V) is dominated by this direct transport due to severe band bending at the CNT inversion layer interface with the metal (fig. 7c). The subsurface metal contact cannot contribute to the current flow, because E_F is located near the conduction band edge. As a consequence, direct hole transport across the inversion region will be dominated by tunneling and a nearly constant barrier for V_g < -5 V, as observed in our measurements.

At the transition region from indirect transport to direct transport (5 V < V_g < -5 V), a large band offset exists between the subsurface CNT and the CNT Inversion layer. With a large enough applied V_{sd}, minority electron carriers from the CNT can tunnel from the valance band of the inversion region to the metal-covered CNT conduction band (fig. 7d). As V_g is decreased (larger negative magnitude) majority hole carriers start to tunnel from the metal and into the inversion layer (direct conduction) as shown in fig. 9C, and the minority electron current decreases. This decrease of minority carriers gives rise to the brief decrease of the total current, visible as a hump (fig. 5d, fig. 6).

Other metals, including the barrier height measurements of Ti, and Pd, are also consistent with the model and are summarized briefly in fig. 8. Strong hole conduction is observed in Pd due to the p-type nature of both the subsurface and inversion layer (although it is not actually an inversion layer in this context). The off-state occurs when the barrier between the inversion region and CNT channel increases as the gate bias increases. Neither electron conduction nor hole conduction is allowed due to the lack of an indirect or direct transport path for large positive V_g. Therefore, no ambipolar behavior can be expected in the case of Pd metal. For Ti, on the other hand, increased ambipolar conduction is observed when compared with metal contacts having much lower work function due to favorable direct conduction of both hole and electron carriers. The work function of Ti (4.6 eV) is located 0.1 - 0.2 eV below the conduction band minimum of CNT (in the band gap) and limits indirect hole conduction in the presence of a surface dipole. However, the CNT inversion layer E_F is located closer to the valence band, permitting larger directly injected current. The Schottky barrier for direct conduction of electron current in the case of Ti is smaller than in the case of Hf and Pd. This direct mechanism is in addition to a small indirect flow of electrons, allowing weak ambipolar behavior even in the presence of surface dipole (fig. 8). The direct transport mechanism dominance is further confirmed due to the equivalent hole and electron currents at equal measured Schottky barrier heights (fig. 5b).

After considering each metal independently, we also note that the differences in $\dfrac{\partial \Phi_b^{holes}}{\partial V_g}$ and $\dfrac{\partial \Phi_b^{electrons}}{\partial V_g}$ from fig. 4 must be a direct consequence of $\left| \dfrac{\partial E_F^{Inversion}}{\partial V_g} \right| << \left| \dfrac{\partial E_F^{channel}}{\partial V_g} \right|$. The value of $\dfrac{\partial E_F^{Inversion}}{\partial V_g} \propto \dfrac{\partial \Phi_b^{electrons}}{\partial V_g}$ is strongly limited by the dipole induced screening. Meanwhile,

$\dfrac{\partial E_F^{channel}}{\partial V_g} \propto \dfrac{\partial \Phi_b^{holes}}{\partial V_g}$ is unaffected by dipoles and related only to the gate/CNT coupling. A

significantly large value of $\dfrac{\partial \Phi_b^{holes}}{\partial V_g}$ is observed in our measurements, as evidenced by the

electrical measurements in fig. 5 for Ti and Pd. Additionally, we suggest that the previously

observed decreases in on-state hole current[66] after annealing or high vacuum degassing are the

consequence of a weakened CNT inversion region and not a significant variation in work

function. The inversion region remains p-type, but E_F shifts closer to mid-band gap as oxygen

desorbs. The result is a thicker barrier for hole conduction and a decrease in tunneling current.

The appearance of a weak electron conducting on-state can occur if desorption weakens the

dipole significantly, similar to recent reports.[66]
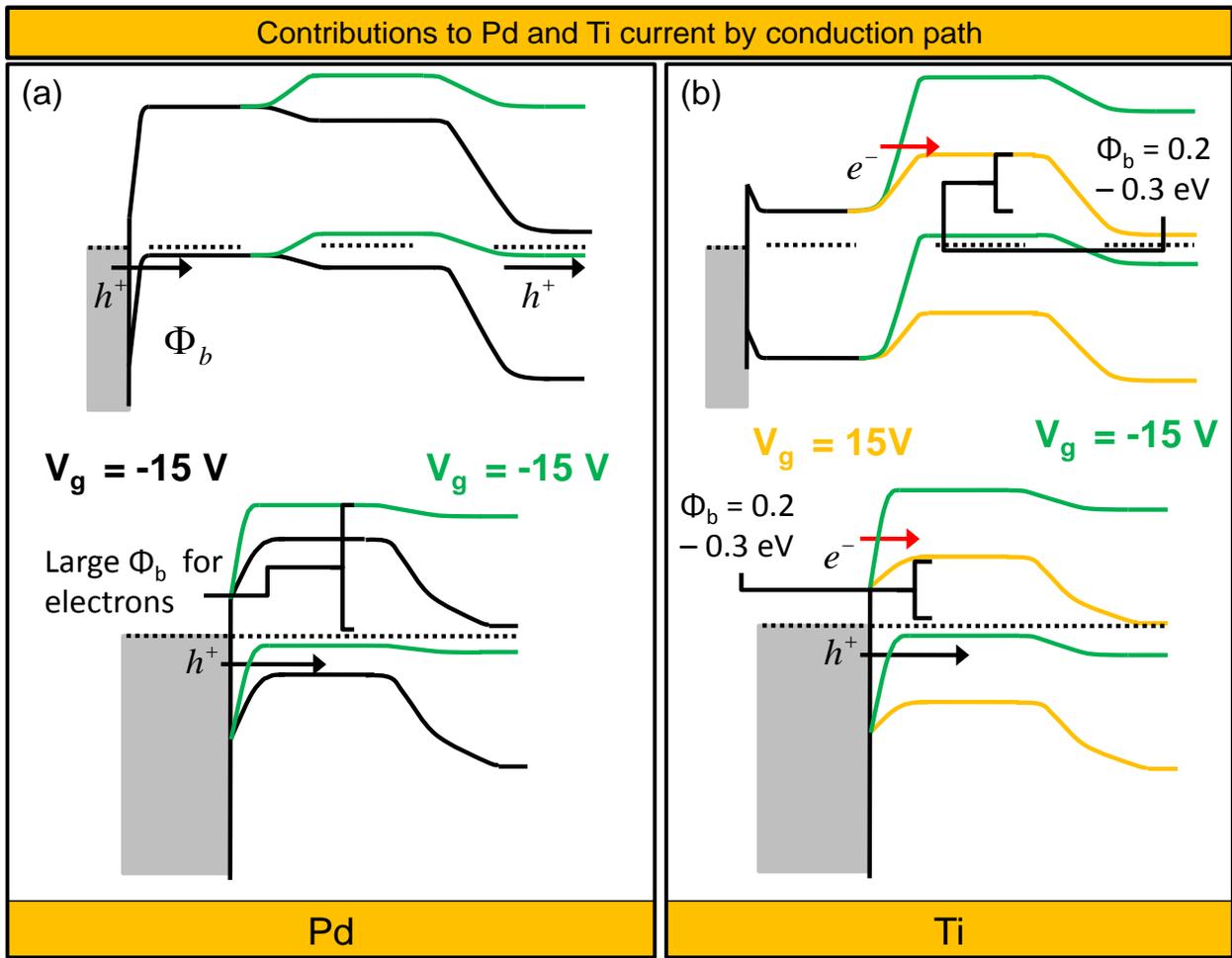
Figure 8. Band diagrams at various V_g for Pd and Ti. (a) Pd in hole conduction state has possibility of carrier contribution via both direct and indirect mechanisms. Conversely, large direct and indirect transport barriers for electrons suppress electron current flow. (b) On the other hand, Ti direct transport contributes carriers to both hole and electron transport. For this reason, Ti devices often show better ambient ambipolar characteristics than metals with much smaller work function. Indirect current likely also contributes electrons for large positive V_g as can be seen from (b).

2.2.3   Conclusion

In conclusion, surface inversion channel model, which includes two competing pathways for carrier transport, has been proposed to explain the anomalous barrier heights and a transconductance hump in our experimental results. This model clearly explains why ohmic contacted n-type devices are difficult to achieve. For air-stable electron conduction, low work function metal with weak surface dipole must be utilized for CNT contact. The inversion channel model is in agreement with previous results by other groups and should serve as a basic outline for adsorbate exposed CNT-FET conduction.

2.3 THERMIONIC FIELD EMISSION TRANSPORT IN CARBON NANOTUBE

TRANSISTORS: CONTACT METAL DEPENDENCE

2.3.1 Introduction

We focus on two CNT-FET samples in this study, the first contained 120 electrodes (114 devices) on a single 6 mm long semiconducting CNT of 1.7 nm diameter with 86 devices electrically active at the first measurement (75.4 % yield). The diameter was confirmed by AFM, and the lack of 100% yield results from regions where the single CNT was damaged during fabrication. Sample 1 utilizes the metals Ti, Pd, Cr, and Hf as metal contacts. In addition, to confirm the model consistency, we prepared a second sample incorporating only Ti and Au electrodes on a 5 mm long, 1.53 nm diameter semiconducting CNT. Optical images of samples are shown in Fig. 2a and a magnified AFM image in Fig. 2b. The metals Au, Ti, Pd, Cr, and Hf were chosen because they are non0-ferromagnetic, and possess a wide range of work functions $(4.0 - 5.2 \, \text{eV})$.

2.3.2 Results and Discussion

I-V measurements were performed on two CNT samples in ambient environment using a probe station. A back gate bias of $V_g = -15$ V was found to be sufficient to bias all devices in the hole-conducting on-state. This restriction was necessary to prevent the existence of multiple carrier types and eliminate the effect of threshold voltage shifts in the analysis of different metals. Figure 9a shows the clear I_{sd} relationship with metals, with an order of

$I(Hf) < I(Cr) < I(Ti) < I(Pd)$. I_{sat} is found by extrapolating the linear region of $\ln(I_{sd})$ vs. V_{sd} to $V_{sd} = 0\,\text{V}$, as illustrated in Fig. 9a. The corresponding σ_{sd} curves are also provided in Fig. 9b. To calculate σ_{sd}, $I_{sd}(V_{sd})$ curves were smoothed with a 16 point Savitzky Golay filter and the resulting curves are differentiated. The data were tabulated by metal type, and differential conductance at $V_{sd} = 0$ point was chosen from each device for comparison.

To accurately compare σ_{sd} and I_{sat} for different metal contacts, statistical analysis is performed on the raw data to check the normality of each distribution. For data with a normal distribution, the mean will be used as an accurate comparative value to test for a dependence between metal σ_{sd} and I_{sat}. Figure 10a shows a histogram of differential conductance by metal type. Although there is an overlap in the differential conductance for each metal, a distinct trend for σ_{sd} is observed with an order, $\sigma_{sd}(Hf) < \sigma_{sd}(Cr) < \sigma_{sd}(Ti) < \sigma_{sd}(Pd)$. It will be demonstrated later in this report that the overlap is attributable to the widely varying and often overlapping work functions for each of the metal species. A Shapiro-Wilk normal distribution test of the data with $\alpha = 0.05$ permitted rejection of the normal distribution hypothesis for the metal Pd due to the wide asymmetric distribution of the data.[95] In this case, σ_{sd} for Pd-contacted devices is very unlikely to be representative of a normal distribution, as expected due to the ohmic qualities of many devices limiting the upper range of conductance. To examine the dependence of mean σ_{sd} on work function of Hf, Cr, Ti, and Au metal, $\ln(\sigma_{sd})$ vs. work function (See Table 2 for more details) is plotted in fig. 10b. A linear relationship between $\ln(\sigma_{sd})$ and work function is observed, although nonlinearity comes into play at large work function.
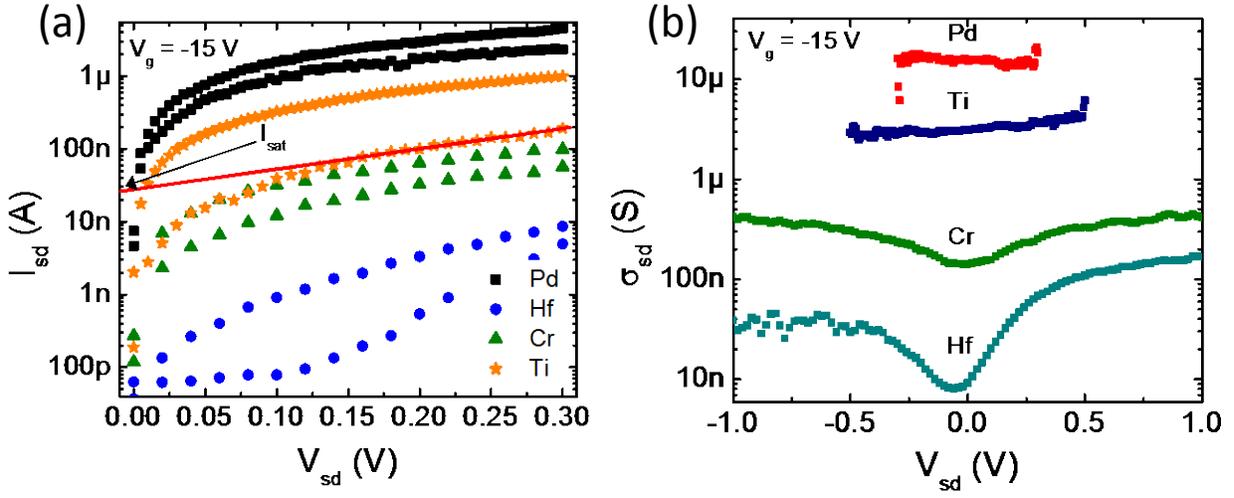
Figure 9. Device structure and electrical properties of SWCNT. (a) Optical image and (b), AFM image of CNT-FET devices. Scale bar is 1mm for optical and 20 µm for AFM image. (c) I_{sd} vs. V_{sd} curves for a group of metals on the same CNT. Example of extrapolation procedure used to estimate I_{sat} is shown in the case of a Ti contact. (d) Differential conductance curves for sample of Hf, Cr, Ti, and Pd metals exemplifying metal-dependence.

In order to understand relationship between $\ln(\sigma_{sd})$ and work function, we begin with

TFE current, since strict thermionic emission current and field emission current will give rise to a

linear relationship. Pure thermionic emission theory also predicts that:

$$I_{sd} = A^{**} e^{-\frac{\Phi_0 - B\sqrt{V_{sd}}}{kT}} \left(e^{\frac{V_{sd}}{kT}} - 1 \right)$$ (2.3)

Where A** is the effective Richardson constant, B is a constant dependent upon the

semiconductor dielectric.

Differentiating:

$$\frac{\partial I_{sd}}{\partial V_{sd}} = \left(C \frac{\left(e^{\frac{V_{sd}}{kT}} - 1 \right)}{\sqrt{V_{sd}}} \right) e^{-\frac{\Phi_0 - B\sqrt{V_{sd}}}{kT}} + D e^{-\frac{\Phi_0 - B\sqrt{V_{sd}}}{kT}} e^{\frac{V_{sd}}{kT}}$$ (2.4)

To evaluate at $V_{sd} = 0$, l'Hôpital's rule is used for the first term, which approaches zero as V_{sd}

tends to zero. This leaves the expression:

$$\frac{\partial I_{sd}}{\partial V_{sd}}(0) \propto e^{-\frac{\Phi_0}{kT}}$$ (2.5)

Taking the natural log of this expression the final relationship is observed:

$$\ln\left[\frac{\partial I_{sd}}{\partial V_{sd}}(0) \right] \propto -\frac{\Phi_0}{kT} \propto -38.61\Phi_m$$ (2.6)

A simple linear fit of the data in fig. 10b produces a slope < 10, indicating the presence of

a large field emission component. Therefore, a mixed TFE theory adopted from Crowell et al.[96]

and Padovani et al.[97] is incorporated to fit the experimental observations. TFE current at a metal-

semiconductor junction is described by,

$$I_{sd} = I_{sat}\left[e^{\frac{V_{sd}}{kT}} - 1\right] \qquad (2.7)$$

With

$$I_{sat} = \frac{A\pi^{1/2}E_{00}^{1/2}\left(\Phi_b - V_{sd} + \varsigma_2\right)^{1/2}}{kT\cosh\left(E_{00}/kT\right)} \times e^{\left(\frac{\varsigma_2}{kT} - \frac{\Phi_b + \varsigma_2}{E_0}\right)} \qquad (2.8)$$

where A is the Richardson constant, T is temperature in Kelvin, k is the Boltzmann constant, Φ_b is the Schottky barrier height, $\varsigma_2 = E_F - E_V$, E_F is the CNT Fermi level, E_v is the CNT valence band, E_{00} is a TFE tunneling parameter,[96] and $E_0 = E_{00}\coth\left(\frac{E_{00}}{kT}\right)$. Applying $V_g = -15\,\text{V}$ results in $\varsigma_2 = E_F - E_V \approx 0$, simplifying the system. We utilize the Schottky-Mott relationship and assume that $\Phi_b \approx \Phi_s - \Phi_m$. From the value of graphite, electron affinity, $X_{CNT} \approx 4.5$ and for a CNT diameter of 1.7 nm, energy gap, $E_g \approx 0.65\,\text{eV}$.[37] Therefore, $\Phi_b \approx 5.15 - \Phi_m$, allowing replacement of the barrier dependence with a work function dependence. Further differentiating equation (2.7) and substituting equation (2.8) with the above relationships for Φ_b, we now derive an expression for σ_{sd}:

We begin with the source – drain current described above, and first, differentiating with respect to V_{sd} using chain rule:

$$\frac{\partial I_{sd}}{\partial V_{sd}} = \frac{\partial I_s}{\partial V_{sd}}\left[e^{\frac{V_{sd}}{kT}} - 1\right] + I_s \frac{\partial e^{\frac{V_{sd}}{kT}}}{\partial V_{sd}} \qquad (2.9)$$

Substituting in the values of the derivatives:

$$\frac{\partial I_{sd}}{\partial V_{sd}} = -\frac{1}{2}\frac{A\pi^{\frac{1}{2}}E_{00}^{\frac{1}{2}}\left(\Phi_b - V_{sd} + \varsigma_2\right)^{-\frac{1}{2}}}{kT\cosh\left(E_{00}/kT\right)}\times e^{\left(\frac{\varsigma_2}{kT}-\frac{\Phi_b+\varsigma_2}{E_0}\right)}\left[e^{\frac{V_{sd}}{kT}}-1\right]+$$
$$\frac{A\pi^{\frac{1}{2}}E_{00}^{\frac{1}{2}}\left(\Phi_b - V_{sd} + \varsigma_2\right)^{\frac{1}{2}}}{kT\cosh\left(E_{00}/kT\right)}\times e^{\left(\frac{\varsigma_2}{kT}-\frac{\Phi_b+\varsigma_2}{E_0}\right)}\left[\frac{e^{\frac{V_{sd}}{kT}}}{kT}\right] \tag{2.10}$$

Gathering like terms, simplifying:

$$\frac{\partial I_{sd}}{\partial V_{sd}} = \left[\frac{\left(\Phi_b - V_{sd} + \varsigma_2\right)^{\frac{1}{2}}}{kT}-\frac{1}{2\left(\Phi_b - V_{sd} + \varsigma_2\right)^{\frac{1}{2}}}\right]\frac{A\pi^{\frac{1}{2}}E_{00}^{\frac{1}{2}}}{kT\cosh\left(E_{00}/kT\right)}\times e^{\left(\frac{\varsigma_2}{kT}-\frac{\Phi_b+\varsigma_2}{E_0}\right)}\left[e^{\frac{V_{sd}}{kT}}\right] \tag{2.11}$$

Combining the fractions:

$$\frac{\partial I_{sd}}{\partial V_{sd}} = \left[\frac{2\left(\Phi_b - V_{sd} + \varsigma_2\right)-kT}{2\left(\Phi_b - V_{sd} + \varsigma_2\right)^{\frac{1}{2}}kT}\right]\frac{A\pi^{\frac{1}{2}}E_{00}^{\frac{1}{2}}}{kT\cosh\left(E_{00}/kT\right)}\times e^{\left(\frac{\varsigma_2}{kT}-\frac{\Phi_b+\varsigma_2}{E_0}\right)}\left[e^{\frac{V_{sd}}{kT}}\right] \tag{2.12}$$

Letting $V_{sd} = 0$;

$$\frac{\partial I_{sd}}{\partial V_{sd}}\left(V_{sd}=0\right) = \left[\frac{2\left(\Phi_b + \varsigma_2\right)-kT}{2\left(\Phi_b + \varsigma_2\right)^{\frac{1}{2}}kT}\right]\frac{A\pi^{\frac{1}{2}}E_{00}^{\frac{1}{2}}}{kT\cosh\left(E_{00}/kT\right)}\times e^{\left(\frac{\varsigma_2}{kT}-\frac{\Phi_b+\varsigma_2}{E_0}\right)} \tag{2.13}$$

In our case, $2\left(\Phi_b + \varsigma_2\right) \gg kT$, so the parenthesis can be reduced to:

$$\frac{\partial I_{sd}}{\partial V_{sd}} = \left[\frac{\left(\Phi_b + \varsigma_2\right)^{\frac{1}{2}}}{kT}\right]\frac{A\pi^{\frac{1}{2}}E_{00}^{\frac{1}{2}}}{kT\cosh\left(E_{00}/kT\right)}\times e^{\left(\frac{\varsigma_2}{kT}-\frac{\Phi_b+\varsigma_2}{E_0}\right)} \tag{2.14}$$

Simplifying:

$$\frac{\partial I_{sd}}{\partial V_{sd}} = \left(\Phi_b + \varsigma_2\right)^{\frac{1}{2}}\frac{A\pi^{\frac{1}{2}}E_{00}^{\frac{1}{2}}}{\left(kT\right)^2\cosh\left(E_{00}/kT\right)}\times e^{\left(\frac{\varsigma_2}{kT}-\frac{\Phi_b+\varsigma_2}{E_0}\right)} \tag{2.15}$$

Taking the natural log of both sides:

$$\ln\left(\frac{\partial I_{sd}}{\partial V_{sd}}(V_{sd}=0)\right) \propto \frac{1}{2}\ln(\Phi_b+\varsigma_2)+\frac{\varsigma_2}{kT}-\frac{\Phi_b+\varsigma_2}{E_0} \qquad (2.16)$$

$V_g = -15$, we can assume that $\varsigma_2 \approx 0$:

$$\ln\left(\frac{\partial I_{sd}}{\partial V_{sd}}(V_{sd}=0)\right) \propto \frac{1}{2}\ln(\Phi_b)-\left(\frac{1}{E_0}\right)\Phi_b \qquad (2.17)$$

The final relation is found by substituting $\Phi_b = 5.15 - \Phi_m$ for $E_g \sim 0.65$ eV.

$$\ln\left(\frac{\partial I_{sd}}{\partial V_{sd}}(V_{sd}=0)\right) \propto \frac{1}{2}\ln(5.15-\Phi_m)-\left(\frac{1}{E_0}\right)(5.15-\Phi_m) \qquad (2.18)$$

Or simply:

$$\ln(\sigma_{sd}) \propto \frac{1}{2}\ln(5.15-\Phi_m)-\left(\frac{1}{E_0}\right)(5.15-\Phi_m) \qquad (2.19)$$

The fitting of this function to Hf, Cr, Ti, and Au is shown fig. 10b. These results allow extraction of tunneling parameters $E_0 = 0.147eV = E_{00}$ and $\frac{kT}{E_{00}} \approx 0.176$. The analysis of Crowell and Rideout is next used to find $\alpha_M = \frac{E_{carriers}}{(\Phi_b)} = \cosh\left(\frac{E_{00}}{kT}\right)^{-2}$,[96] where α_M is defined as a ratio of carrier energy $E_{carriers}$ to barrier height Φ_b. $\alpha_M \approx 0$ from our model, indicating that most carriers tunnel directly to the valence band maximum. As a result of assumptions in the derivation, the excellent fit of equation (2.19) to the experimental observations strongly supports the existence of an unpinned Fermi level at metal-CNT interface. The source of the nonlinearity in fig. 10b results from growth of the logarithmic term in equation (2.19) as $\Phi_m \Rightarrow 5.15$. Phenomenologically, the energy barrier is sufficiently small and field emission dominant such that variations in barrier height produce little to no change in differential conductance.

We next consider the saturation current of the above measured SFETs as a function of metal work function to further validate the theoretical model and the accurate fitting of the differential conductance. I_{sat} for the metals was found by using both $\pm V_{sd}$ curves from all device measurements as the positive and negative voltage regimes are correlated to the source/drain contacts separately (Hence two I_{sat} values for each device).[98] A histogram of the raw data is shown in fig. 11a. The Shapiro-Wilk normal – distribution test of these data again allowed rejection of the possibility that Pd came from a normal distribution for $\alpha = 0.05$. The data set for the saturation current is significantly larger than that for differential conductance due to the use of both $\pm V_{sd}$ from raw data, hence (other than Pd) the distributions have more visually symmetrical shape.

Interestingly, the exact same TFE relationship as for σ_{sd} can be used to fit I_{sat}, using equivalent work function and Fermi level assumptions:

First taking natural log of equation 2.8, setting $V_{sd} = 0$ (due to finding I_{sat} at $V_{sd} = 0$) and assuming that $\varsigma_2 \approx 0$ once again:

$$\ln\left(I_{sat}(V_{sd} = 0)\right) = \ln\left(\frac{A\pi^{1/2}E_{00}^{1/2}}{kT\cosh\left(E_{00}/kT\right)}\right) + \frac{1}{2}\ln\left(\Phi_b\right) - \frac{\Phi_b}{E_0} \tag{2.20}$$

Removing offset (we only care about proportion, although after extraction of E_0 the above equation 2.20 may be usable at a later time to calculate empirical constants for the metal-CNT junction.),

$$\ln\left(I_s(V_{sd} = 0)\right) \propto \frac{1}{2}\ln\left(\Phi_b\right) + -\frac{\Phi_b}{E_0} \tag{2.21}$$

Hence we have derived the exact same relationship (equation 2.19) as differential conductance.

$$\ln\left(I_{sat}\left(V_{sd}=0\right)\right) \propto \frac{1}{2}\ln\left(5.15-\Phi_m\right)-\left(\frac{1}{E_0}\right)\left(5.15-\Phi_m\right) \qquad (2.22)$$

Note that the first term is much smaller than the second term since E_0 is presumably small. With the above expression, we again tried to fit the experimental $\ln\left(I_{sat}\right)$ data. Pd was not included in the fitting, again because the sample mean was not reflective of the asymmetric distribution. Figure 11b shows $\ln\left(I_{sat}\right)$ versus work function. The extracted tunneling parameters, $E_0 = 0.139 = E_{00}$ and $\frac{kT}{E_{00}} \approx 0.186$, are similar to those of differential conductance. This indicates that TFE and the derived model explain hole conduction in CNTFETs accurately.
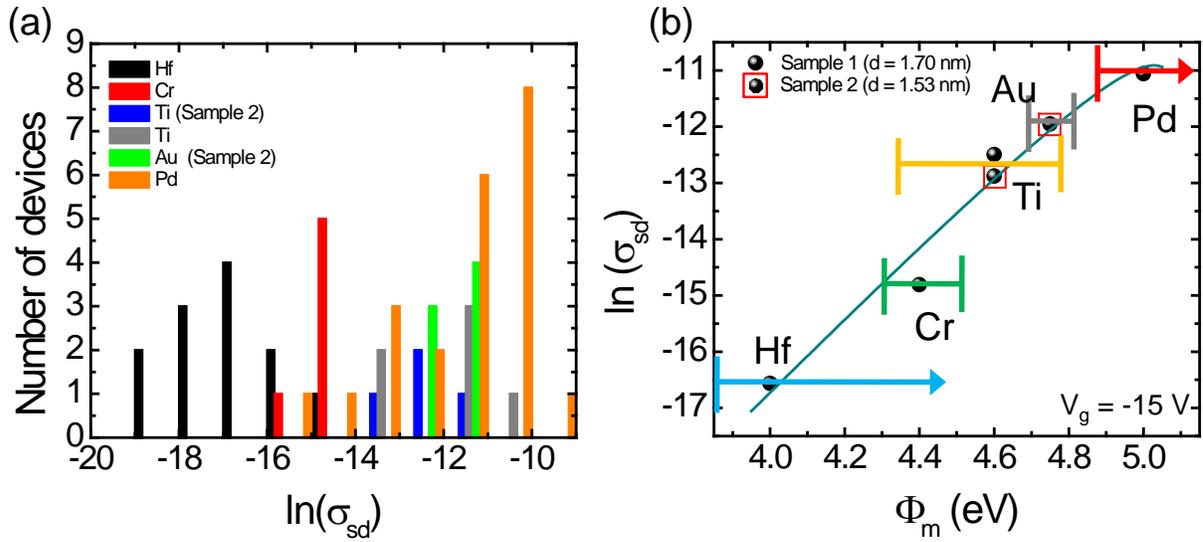
Figure 10. Raw data of differential conductance (σ_{sd}) and fitting to theoretical thermionic field emission model. (a) Histograms of $\ln\left(\sigma_{sd}\right)$ at $V_g = -15V$. In order of smallest to largest mean value: Hf, Cr, Ti, Au, Pd. (b) $\ln\left(\sigma_{sd}\right)$ plotted vs. contact metal work function. The differential conductance value used for fitting each metal is the mean of the distributions in (a.) Work function range is from the literature (Supplementary Information T1). Hf and Pd arrows are due to possibility of large work function variations; in these cases the theoretical or only available literature values were chosen.
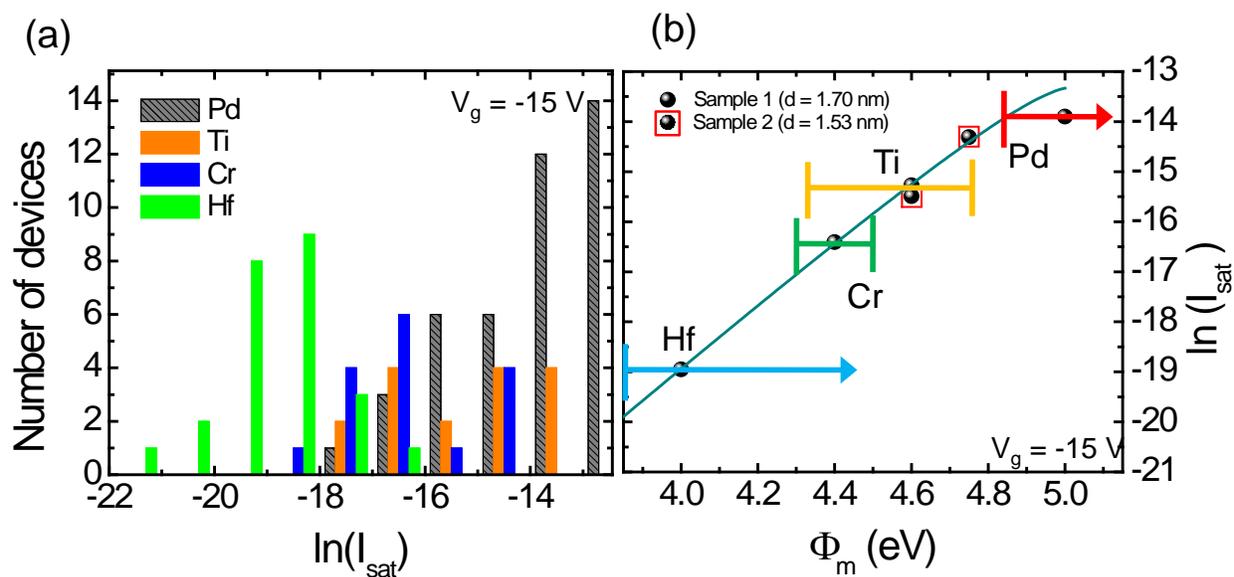
Figure 11. Raw data of $\ln\left(I_{sat}\right)$ and fitting to theoretical thermionic field emission model. (a) Raw data of $\ln\left(I_{sat}\right)$ at $V_g = -15$ as a function of metal. (b) Fitting of the mean values of $\ln\left(I_{sat}\right)$ for Hf, Cr, and Ti to TFE model derived and discussed in the text. The error bounds for work function are taken from the literature (Supplementary Table S1). Hf and Pd arrows are due to possibility of large work function variations; in these cases the theoretical or only available literature values were chosen.

Next, we consider the small variation of differential conductance (and I_{sat}) observed particularly in the case of Au and Cr in fig. 12. These metals are in contrast with Pd and Hf in which a large variation was observed. Further, if one fits the raw data variance onto the observed curve of $\ln(\sigma_{sd})$ vs. Φ_b, the resulting work function spread falls within the expected work function range observed in ambient, indicating strong correlation between local work function and σ_{sd}. This phenomenon is demonstrated in fig. 12. It is therefore concluded that variation of σ_{sd} (and I_{sat}) is strongly related to environmental stability of metal, since work function can be easily modified by adsorbates (Particularly in the case of Pd and Hf). Implication of our measurements and theoretical model fitting are very intriguing, particular for gas sensing. Physisorption of gases on a metal alters the work function and surface dipole according to exposure dose, often by well-known relationships. While the metals display no change of conductance with exposure, when used as a contact to a CNT, the work function and dipole change will result in a measurable I_{sat} and σ_{sd} difference explainable by the relationships derived in this report. An initial constraint to this sensing approach is the variation in conducting properties for different CNT under varying initial environmental conditions. However, the use of different diameter CNT will only affect CNT work function, and a simulation of curves increased (decreased) saturation current for smaller (larger) diameter CNT is seen in fig. 13. Similar trends are visible for each diameter, but the model fails at a lower contact-metal work function due to the smaller CNT work function in larger diameter tubes. In CNT with a diameter 3.0 nm, I_{sat} approaches 15 µA, similar to what has been observed experimentally. This suggests that with large work function metal contacts, the model can also predict I_{sat} in other CNT devices.[99]

Therefore, simple I-V measurement during exposure will allow extraction of the work function of the metal, which will in turn allow one to measure the existence and even the concentration of certain gas species, which previously has been impossible to quantify.

2.3.3 Conclusion

In conclusion, we have demonstrated clear work-function dependent relationships for hole current σ_{sd} and I_{sat}. These parameters have been correlated by an existing contact-dominant conduction mechanism. Using TFE theory, tunneling parameters were extracted using a novel characterization method that strongly suggests an unpinned Fermi level in carbon nanotubes. Additionally, the results for σ_{sd} and I_{sat} fittings are in agreement and the mathematical model presented can also be utilized to selectivity sense adsorbates in single CNT sensors *via* contact work function change. The process could further be reversed to detect work function of a metal in the case of a well controlled environment, an important discovery for materials where local probing or optical methods are impossible.
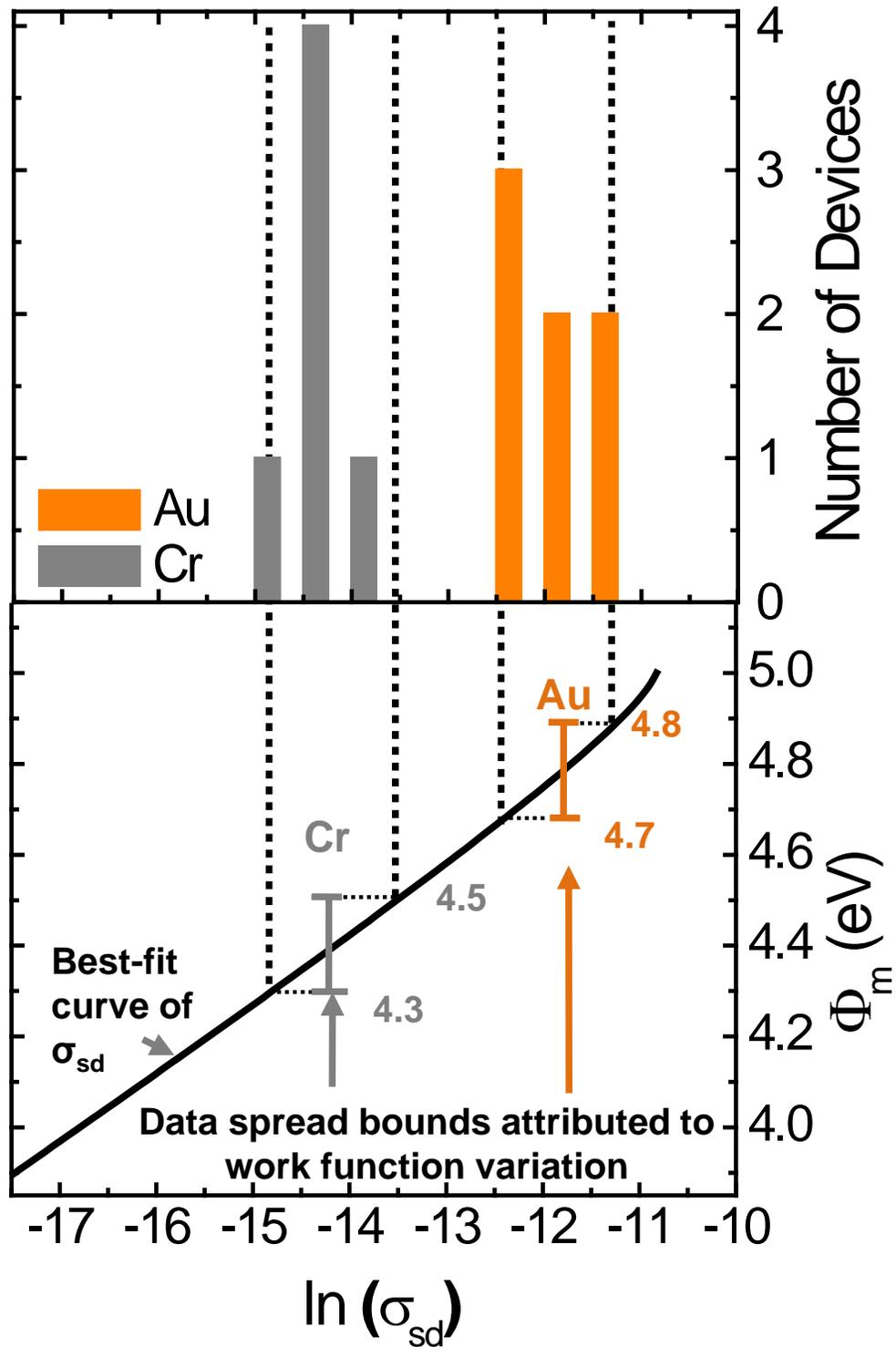
Figure 12. Precise correlation is observed in the differential conductance of Au and Cr devices. The spread that could be expected due to work function changes is identical to the data spread, suggesting that work function differences at the contact is the dominant cause of I-V variations among same-metal contacts.
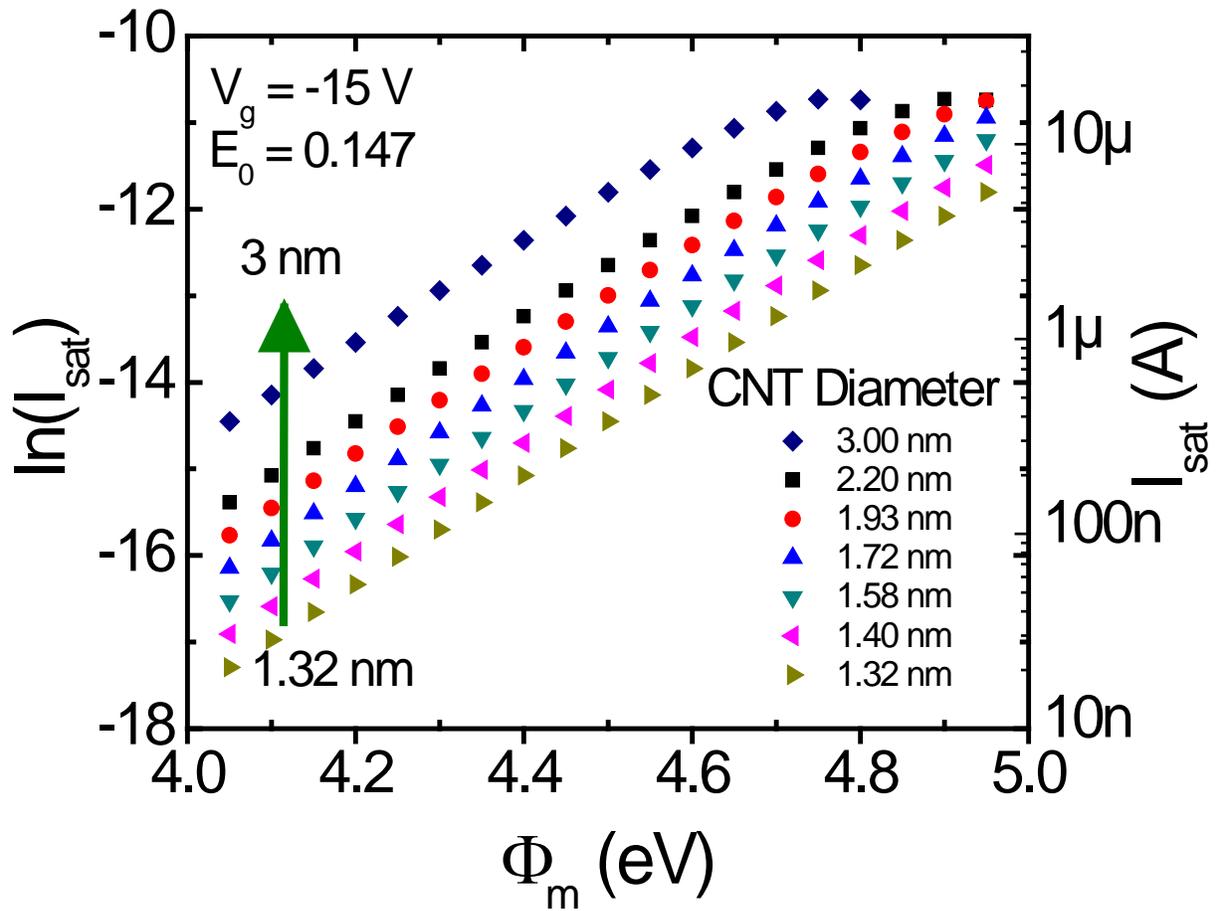
Figure 13. Simulation of diameter effect on $\ln(I_{sat})$ best fit curves. Simulated $\ln(I_{sat})$ curves for different diameter CNT using the model and constants from the text. Assuming $E_{00} = 0.147$ and that all other factors except CNT work function are constant.

2.4   CARBON NANOTUBE DIODES: VOLTAGE AND CONTACT-METAL WORK

FUNCTION DEPENDENCE

2.4.1   Introduction to Anisotropy

To construct a model for CNT diode hole-transport with gate-bias V_g = -15 V (hole transport

only), we introduce current anisotropy defined by $\tilde{A} = \dfrac{\left| I_{sd}\left(V = V_F\right)\right|}{\left| I_{sd}\left(V = -V_F = V_R\right)\right|} = \dfrac{\left| I_F\right|}{\left| I_R\right|}$. I_F is defined as

the larger magnitude current (V_{sd} > 0 for consistency). Note that this definition does not imply

direction of current flow as in a typical metal-semiconductor junction. Here, I_R is the smaller

magnitude current (V_{sd} < 0 V), and I_F the larger current (V_{sd} > 0). For a mathematical model of

$\tilde{A}$, a few assumptions are needed as follows: (i) both metal contacts to the CNT are Schottky in

nature. (ii) For I_F (I_R), the contact with larger (smaller $\Phi_m = \Phi_{m2}$) $\Phi_m = \Phi_{m1}$ is the dominant

contact. The large work function Φ_{m1} (small Φ_{m2}) contact will be defined by Schottky barrier

height $\Phi_{b1}\left(\Phi_{b2}\right)$ with subscript "1" ("2"), and (iii) application of V_g = -15 V is sufficient to

bias the device in the hole-only conducting state for all devices/metals.

Assumption (ii) is most significant, since it presents a new paradigm for on-state hole

transport in CNT diodes. By assuming a V_{sd}-dependent dominant contact, we effectively propose

that the resistance of current entering the CNT from the metal at either contact is less than that

from the CNT channel to the metal (for both contacts, metal type independent). Although

contrary to three-dimensional semiconductors, this assumption is appropriate for CNT due to the

large tunneling current contribution to current flow from the metal to the semiconductor. The assumption is visually explained by the band diagrams in fig. 14a and fig. 14b.

2.4.2 Anisotropy Model

To verify the above hypotheses, we introduce a model utilizing the above assumptions derived from thermionic field emission (TFE),[96] and fit the model to experimental observations. TFE was chosen since in its limiting conditions, it accurately models both field emission and thermionic emission. As mentioned above, assuming that Φ_{b2} is dominant for hole transport I_R and Φ_{b1} is dominant for hole transport I_F, we have the following expressions for the magnitudes of I_F and I_R:

$$\left| I_{F(i=1),R(i=2)} \right| = \frac{A\pi^{\frac{1}{2}} E_{00}^{\frac{1}{2}} \left(\Phi_{b(i)} - \left| V_{sd} \right| + \varsigma_{(i)} \right)^{\frac{1}{2}}}{kT \cosh\left(E_{00} \big/ kT \right)} \times e^{\left(\frac{\varsigma_{(i)}}{kT} - \frac{\Phi_{b(i)} + \varsigma_{(i)}}{E_0} \right)} \left(e^{\frac{\left| V_{sd} \right|}{kT}} - 1 \right) \qquad (2.23)$$

Where T is temperature (K), A is the Richardson constant, k is the Boltzmann constant, $\zeta_2 = E_F - E_V = 0$ for V_g = -15 V (E_V = CNT valence band), E_{00} is a TFE tunneling parameter, and $E_0 = E_{00} \coth\left(\dfrac{E_{00}}{kT} \right)$. Applying the above with the Schottky-Mott relationship $\Phi_b \approx \Phi_s - \Phi_m$,[37] substituting into equation (2.23), and solving for $\tilde{A}$ using a first order linear approximation:

$$\ln\left(\tilde{A} \right) \propto \Phi_{b2} - \Phi_{b1} \propto -\Delta\Phi_m$$
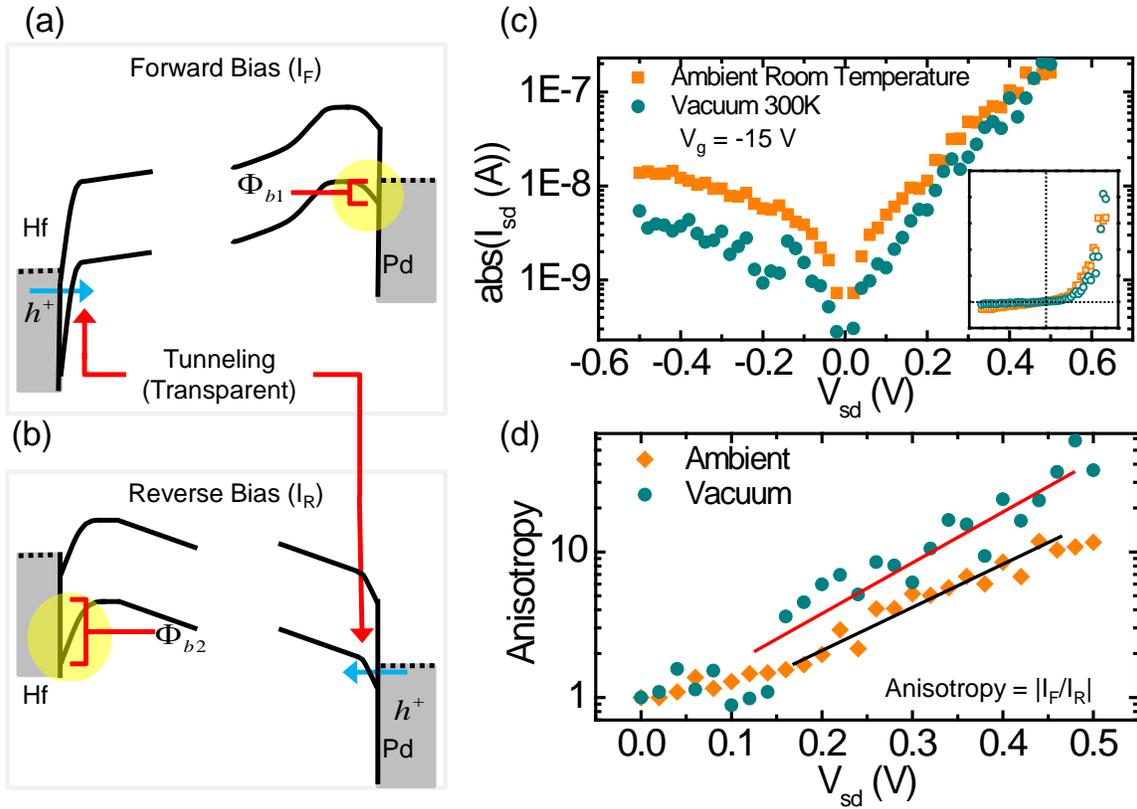
Figure 14. Hf-Pd diode: (a)-(b) Energy band diagram. (a) Device forward bias and (b) device reverse bias. (c) $\left|I_{sd}\right|$ measured in ambient (squares) and vacuum (circles). Inset: linear scale I_{sd} for comparison. (d) Contrast of $\tilde{A}$ in vacuum and ambient.

2.4.3 Results and Discussion

To test the model, we consider heterometallic contacts to CNT with metals Hf, Cr, Ti, Pd, and Au. Since devices were fabricated on the same CNT, fabrication is more difficult but we may assume a consistent CNT band gap, resistance, fabrication/growth conditions, and environment. These are all necessary assumptions to accurately validate the derived TFE model, as use of different CNT will vary each of the parameters. I-V measurements were performed in ambient using a probe station with V_g applied via a back gate, unless otherwise noted. $\tilde{A}$ was then calculated point by point for the following metal electrode pairs: Hf-Cr, Hf-Ti, Hf-Pd, Cr-Ti, Pd-Au. Ambient Φ_m used in the remainder of this report are as follows: Hf = 4.0, Cr = 4.4,[91] Ti = 4.6,[90] Au = 4.8,[100] and Pd ~ 4.9.[100,101]

We first consider the Pd-Hf device measured in ambient and then vacuum as in fig. 14c. Devices fabricated with Pd and Hf contacts had the largest $\Delta\Phi_m$ and largest $\tilde{A}$, as in fig. 14d. Three effects are evident from fig. 14d: (i) I_R decreases by an order of magnitude when comparing measurements in air and vacuum. This is a direct result of the Pd Φ_m increase and Hf Φ_m decrease due to gas desorption in vacuum. (ii) $\tilde{A}$ is exponentially related to V_{sd}. (iii) $\tilde{A}$ of the Pd-Hf device in the vacuum state is significantly increased when compared to ambient; for $V_{sd} = \pm 0.5$ V, anisotropy increases from $\tilde{A} \approx 10$ in ambient to $\tilde{A} \approx 55$ in vacuum without device modification.

To expand upon the qualitative Φ_m dependence in the Pd-Hf results, other mixed-metal devices measured from the same 6mm long CNT are plotted and fit with equation (2.24). Figure 15a displays the raw $\tilde{A}$ for different hybrid device types. Each curve was produced via point by point averaging of 3-5 different devices.

Figure 15a shows that as $\Delta\Phi_m$ increases, $\tilde{A}$ increases for significantly large V_{sd} (~0.5 V). To fit equation (2), we plot $\ln(\tilde{A}) \propto \Phi_{2b} - \Phi_{1b}$ at $V_{sd} = 0.5$ V in fig. 15b. $\Phi_{b1,b2}$ were found by assuming $X_{CNT} \approx 4.5$ eV (graphite), and $E_g \approx 0.65 eV$ for a CNT with diameter of 1.7 nm, giving $\Phi_b \approx 5.15 - \Phi_m$. The resulting graph of $\ln(\tilde{A})$ in fig. 15b is fit well to equation (2.24). If intrinsic Φ_m values for the vacuum measurement of the Hf-Pd device are assumed (Hf = 3.9 eV, Pd = 5.2eV), the resulting data point also fits well to the best fit of equation (2.24), further reassuring the validity of the TFE model and the three major assumptions. Further, the best-fit line has slope $E_{00} = 0.285$, suggesting field emission is dominant for hole on-state transport.[19]

Next, we examine the effect of V_g and majority carrier on a Pd-Hf device. fig. 16a displays I_{sd} vs. V_{sd} for a mixed-metal device in three gate bias regimes: $V_g = -20$ V is a hole-conducting diode, $V_g = -8$ V corresponds to a resistor, and $V_g = 16$ V is an electron transport diode. In the hole conducting on state shown in fig. 16b the device displays $\tilde{A} \approx 10$, while the resistor state has $\tilde{A} \approx 1$. At $V_g = 16$ V, the device has $\tilde{A} \approx 0.1$. Equation (2.24) can be rewritten for electron transport in the form $\ln(\tilde{A}) \propto -(\Phi_{b2} - \Phi_{b1})$.

If it is further assumed that $\Phi_{bx} = \Phi_{mx} - \left[4.5 + .5E_g e^{-V_g/\tau} \right]$ for electrons, $x \in \{1, 2\}$, $0 \le V_g$, and τ a constant dictated by $V_g \sim E_F$ coupling strength, it can be shown that:

$$\frac{\partial \ln(\tilde{A})}{\partial V_g} \propto -V_g \qquad (4.22)$$

This equation is equivalent to the hole-only relationship, valid only for single carrier type conduction for large $\pm V_g$ as in fig. 16b. Figure 16b also indicates that although the device changes polarity, the current magnitude in the intermediate resistor state is by far the greatest. Also, for $V_g \gg 0$, I_{sd} is small for either $\pm V_{sd}$, while I_{sd} at $V_{sd} < 0$ (on state) at $V_g = 16$ V is actually lower than I_{sd} for $V_{sd} < 0$ (off state) at $V_g = -16$ V; limiting practical utilization of the device.

2.4.4   Conclusion

In summary, we have demonstrated that in CNT-based Schottky diodes, the primary variable in controlling rectification capabilities is $\Delta\Phi_m$ between the mixed-metal contacts. The CNT-based reversible polarity device, although having reduced current anisotropy compared with Si planar diodes, has greater versatility. A circuit based on adaptive reversible polarity diodes may be implemented in both pull-up or pull-down networks without physical modification.
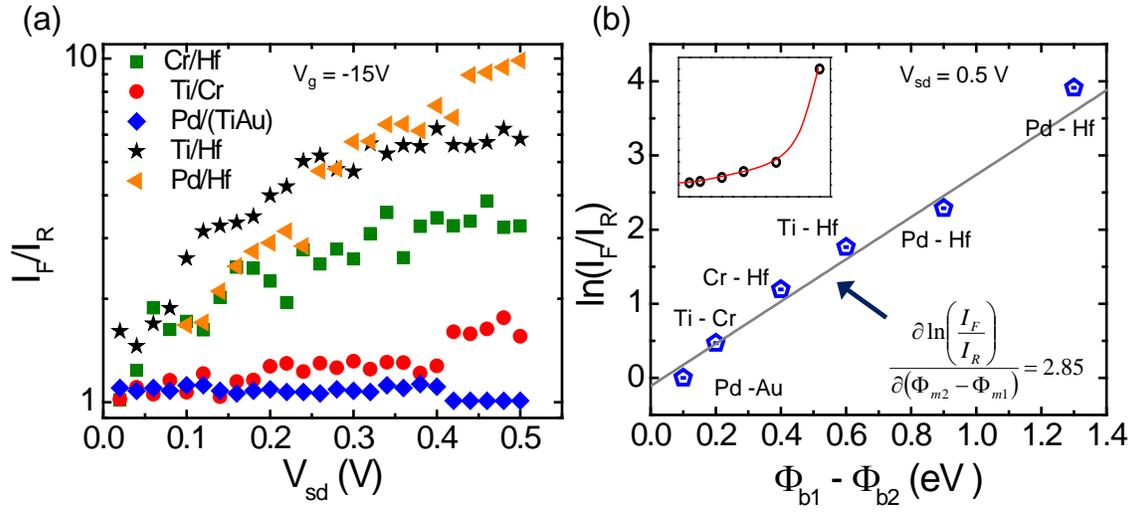
Figure 15. Mixed-metal devices on 1.7 nm diameter CNT: (a) average $\tilde{A}$ vs. V_{sd} for 3-5 devices of each pairing. (b) $\ln\left(\tilde{A}\right)$ vs. $\Phi_{2b} - \Phi_{1b}$ with best fit. Inset shows linear plot of $\tilde{A}$ vs. $\Phi_{2b} - \Phi_{1b}$.
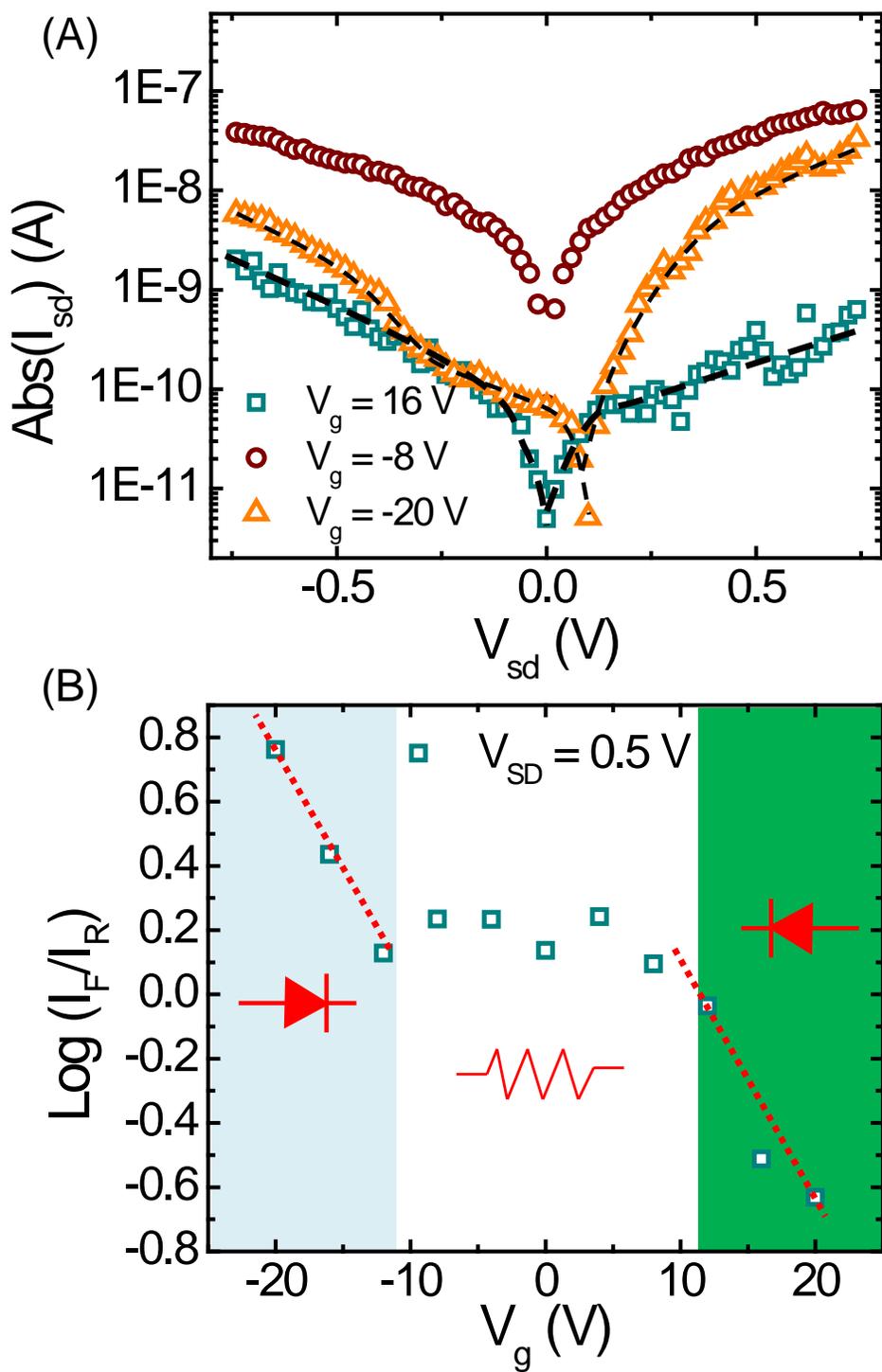
Figure 16. Reversible polarity diode: (a) $\left|I_{sd}\right|$ vs. V_{sd} for V_g = 16, -8, -20 V. (b) $\ln\left(\tilde{A}\right)$ vs. V_g at V_{sd} = 0.5 V.

3.0   FABRICATION OF GRAPHENE NANORIBBONS

3.1   BACKGROUND AND MOTIVATION

The immergence of graphene in 2004 is a major breakthrough in the world of physics. Novoselov *et al*. became the first group to isolate, identify, and electrically measure a truly 2-dimensional crystal lattice.[102] In contrast to 2-dimensional electron gases present at the hetero-interface in III-V high electron mobility transistors, graphene is perfectly 2-dimensional in that it is only 1 atomic layer thick. Although sharing the same basic hexagonal lattice of CNTs, graphene has vastly different electrical properties. Electrons near the Fermi level are described by the linear energy dispersion relation $E = \pm v_F \hbar |q|$, where $v_F \sim 10^6\ ^m\!/_S$ is the Fermi velocity, q is elementary electron charge. The density of states is then linear with respect to momentum and energy (k, E). Carriers near the Fermi level can therefore be described by the Weyl-Dirac Hamiltonian $H = v_F \vec{\sigma} \cdot \vec{p}$ where $\vec{\sigma}$ is the Paul matrice and $\vec{p}$ is the momentum. Therein presents the paradox, because the Weyl-Dirac Hamiltonian describes ultra-relativistic massless Dirac Fermions. Proof of the linear band structure came in the form of field effect measurements in the initial work in 2004, which showed an expected "V" shape in the I_{sd} - V_g characteristics. An example from our work is shown in fig. 17. This was seen as the first confirmation of successful isolation and measurement of graphene. However, the massless Dirac nature of carriers was not confirmed until a year later when the same group at Manchester observed that (i) conductivity at

the cusp or "Dirac Point" in the I_{sd} - V_g sweep of graphene never fell below the quantum unit of conductance, (ii) an anomalous integer quantum hall effect occurring at half-integer filling factors, and (iii) the cyclotron effective mass is described by Einstein's famed $E = mc^2$ relationship. Amazingly, it was shown that a two dimensional lattice of carbon atoms has electrical transport properties typically reserved for ultra-relativistic particles. To further verify the relativistic nature of the graphene carriers, a non-zero Berry's phase was observed in magneto-electric measurements in 2005,[103] and relativistic Klein tunneling in 2009.[104-106] Aside from more academic quantum electrodynamics demonstrations, graphene is interesting from an engineering standpoint due to its extremely high carrier mobility,[107-109] and good thermal conductivity.[110] The difficulty with graphene is not necessarily in the extraction of extraordinary physics from ideal samples, but rather it is the realization of monolayer or bilayer graphene sheets and utilization of graphene in FET devices.

The highest quality graphene samples thus far are produced via mechanical exfoliation of highly ordered pyrolitic graphite (HOPG) or KISH graphite.[111-115] Mechanical exfoliation is performed using the so called scotch tape-method on HOPG,[116] which involves the attachment, and subsequent pressing and release of graphitic pieces onto a sample. Although highly crystalline, only <100 µm graphene flakes with a random number of layers remain on the surface. Most of the unique physical and electrical properties of graphene mentioned above were first observed in these exfoliated samples.

However, since the first intentional growth of graphene on a transition metal film and transfer to an insulating substrate in 2008,[117,118] the quality of graphene samples produced via TCVD has steadily improved. It has been previously shown that almost any transition metal[113,119,120] can be used as a substrate/seed for TCVD growth of graphene. Of these metals,

Ni, Pt and Cu display the best results dependent upon desirable growth properties. Ni is known to produce the highest quality multi-layer graphene (MLG) samples due to its high carbon solubility.[117] On the other hand, it was demonstrated that Pt foils are ideal for growth of large single-domains (> 1 mm) of graphene, along with the ability to repeatedly reuse the foil with an electrochemical transfer method.[121] Although the ability to reuse the foil suggests a future route towards sustainability, Pt is such a rare commodity that price alone is an issue. Growth on Pt foils also utilized growth times far longer than other transition metal foils. Cu is the most studied metal for TCVD graphene growth processes due to its prevalence in the semiconductor industry, cheap cost, fast etching rate in nonhazardous chemicals such as FeCl-based etchants, and the possibility of large single crystal graphene domains.[122,123] As a result, growth of graphene using TCVD on Cu foils will be the focus of all subsequent experimental work in this thesis. In depth growth and transfer procedures are considered in section 3.2.

As a semimetal, graphene intrinsically has no bandgap and therefore a limited field effect response to carrier transport. Unlike CNTs, there are no boundary conditions we can apply to naturally induce a bandgap without modifying the monolayer graphene layer. Application of a transverse (perpendicular) electric field in Bernel-stacked bilayer graphene breaks the electron-hole symmetry and can open a small bandgap.[124] However, large fields are required, and the disadvantage of bilayer graphene is a lower mobility. Furthermore, Bernel-stacked bilayer graphene cannot yet be consistently grown with CVD methods.

Efforts to increase field effect response in monolayer graphene center around reducing the allowable phase space via reduced lateral dimensions.[125-129] Reflecting a consistent problem plaguing both industry and academia in transistor micro fabrication, graphene nanoribbons (GNR) with channel widths (w) smaller than 15 nm are extremely difficult to fabricate with

conventional top-down techniques.[130-132] Circumventing the use of top down procedures, in section 3.3 it will be shown that GNR can instead be fabricating using CNTs as etch masks. I_{sd} - V_g results indicate that on/off ratios greater than 10^4 are possible at room temperature using this novel method.
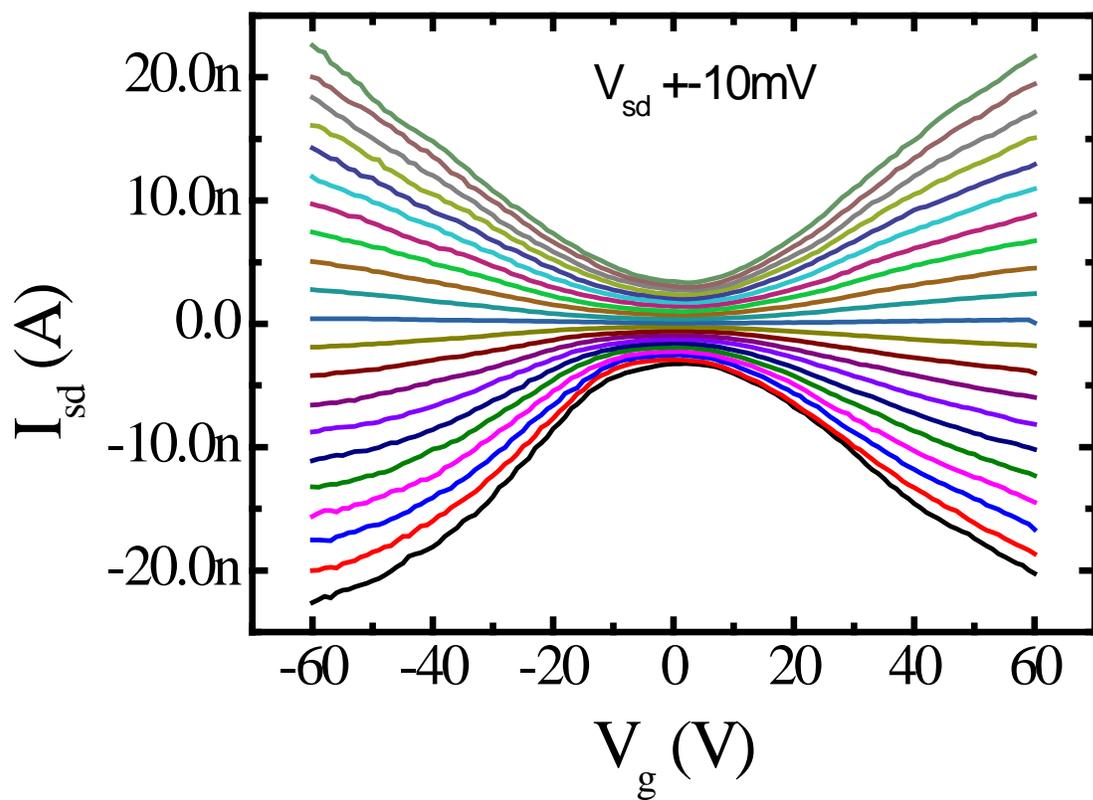
Figure 17. Field effect response of a graphene ribbon with width ~ 100 nm showing characteristic "V" shape.

3.2   GRAPHENE GROWTH AND CHARACTERIZATION

3.2.1   Growth of Graphene Using Chemical Vapor Deposition on Copper Foil

Recent work demonstrates that the nucleation of monolayer graphene and size of resulting crystal domains is highly dependent upon the smoothness of the Cu surface.[122] Therefore, prior to growth, we first annealed and then polished Cu foil using a cheap and easy hand-polishing method. Firstly, 100 micron Cu foil was purchased from Nilaco Corp. The large rolls of foil were carefully cut into ~4 cm x 8 cm pieces and annealed for 3 hours in a tube furnace at 1050° C while flowing 500-1000 sccm of 99.999% Ar gas, and 100 sccm of 99.999% H_2 gas. The annealing is performed to increase the Cu domain size and reduce surface roughness. Samples were then taped to the lid of a 4" plastic Petri dish for polishing. Importantly, the etchant used during polishing must not come into contact with the backside of the foil to avoid unwanted particle formation and damage to the Cu foil. To prevent etchant contamination, the tape was very carefully cut and pressed with sharp tweezers to cover all four edges and the corners of the Cu foil. Next, a two-stage polishing process is performed. In separate 4" plastic Petri dishes, 8 ml and 4 ml of Transene CE-100 (Transene Corporation) etchant are diluted with water to fill the dish to the brim. Ten clean wipes (Kimtech Science) are folded into 5cm x 5 cm squares and placed into each Petri dish. Beginning with the stronger etchant solution, the Cu foil is gently and very quickly wiped with the etchant-soaked wipes without applying significant pressure. After wipes turn green from CuO_x formation, a new wipe is used quickly to prevent drying of particles on the Cu surface. After vigorously polishing with first the strong etchant and then the weak

etchant, the sample is thoroughly washed in 18.3 Ω/cm DI water for ~5 minutes to remove any Cu/CuO$_x$ particles from attaching to the surface. Finally, the sample is dried with a nitrogen or air gun. The final washing step is critical to controlled nucleation of monolayer graphene. For unpolished graphene and on samples where little care was taken to remove Cu/CuO$_x$ nanoparticles, we observed the growth of poor quality monolayer, bilayer and multilayer growth depending upon the growth conditions and pressure. An example of a dirty sample is shown in fig. 18, where the small dots widely spread across the surface were found to be CuO$_x$ particles via electron diffraction spectra.

Graphene growth was performed in the home built LPCVD system discussed in Appendix C using a methane carbon source, hydrogen reducing gas, and argon flow gas following the recipe outlined in fig. 19. For monolayer growth, polished Cu foil was placed in the center region on an Al$_2$O$_3$ sample holder. After checking for leaks and pumping out with a mechanical pump, 200 sccm of Ar and 100 sccm H$_2$ flow was activated while turning on the furnace heating element. At max ramp rate (~20° C/min) the furnace temperature is raised to just under the melting temperature of the copper. This temperature was found to change, but typically the temperature was about 1078° C. Annealing was performed for at least an hour to further decrease surface roughness and remove any residual CuO$_x$ via high temperature reduction with hydrogen. During growth, Ar flow was turned off while flowing 10 sccm H$_2$ and 2 sccm of CH$_4$. On very flat samples, the growth time was found to be self limiting after a few minutes. A 3 minute growth time was found to reproducibly cover the substrate with a monolayer of graphene with sheet resistance ~ 225-300 Ω/□. An example optical and Raman spectra of high quality monolayer graphene is shown in fig. 20a and fig. 20b, respectively.

We further found that non polished/annealed 70 micron thick Cu foil (Nilaco Corp) or 25 micron foil (Alpha Aesar) in atmospheric pressure growth mode nearly always produced more than a single layer of graphene for growth times longer than 30 seconds. It was demonstrated previously that atmospheric growth nucleation and nucleation occurs much faster than low-pressure growth, therefore a monolayer-limiting condition is more difficult to achieve. One few-layer graphene SEM image is displayed in fig. 21.
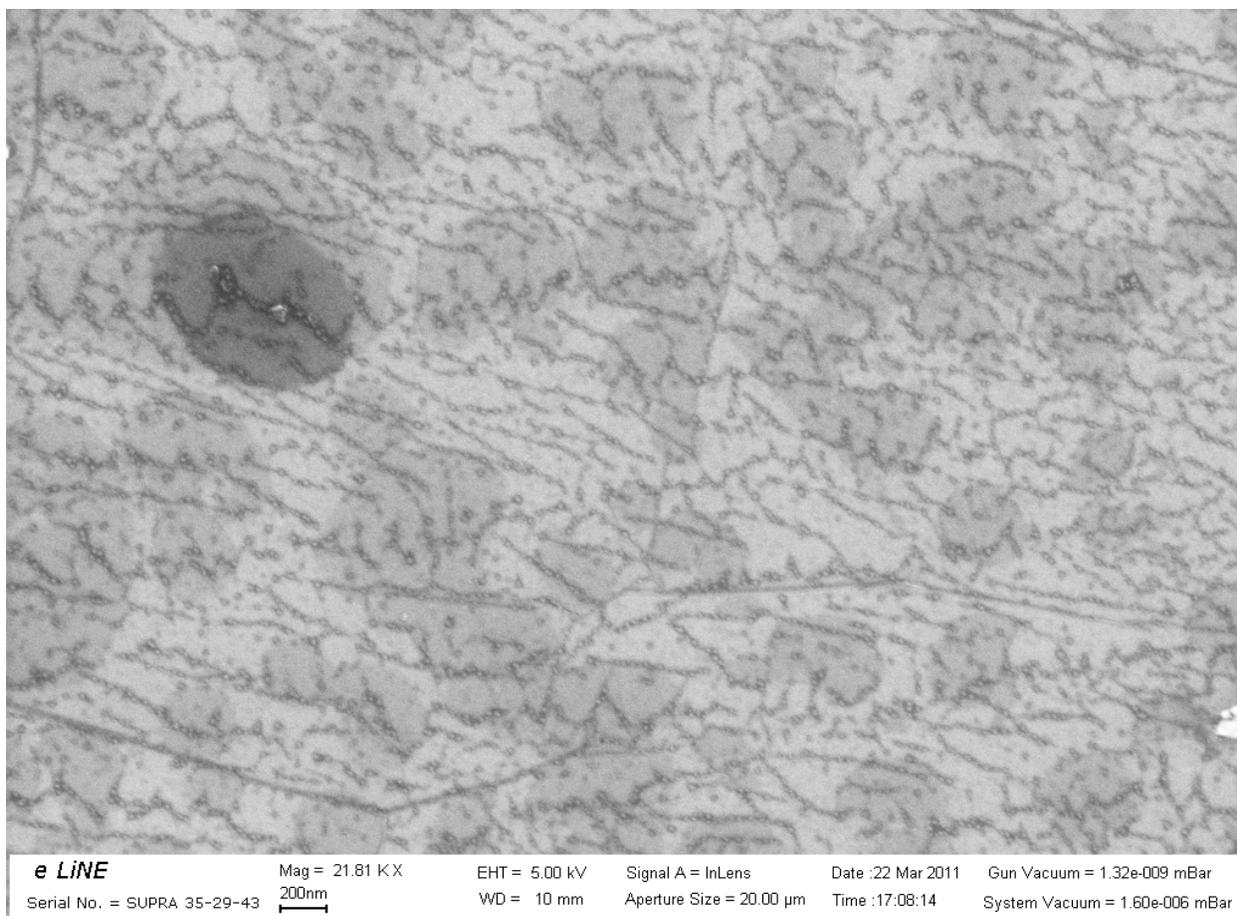
Figure 18. Zoomed images of the graphene surface post-transfer to SiO_2. Close examination reveals Cu/CuO_x nanoparticles littering the surface of the graphene.
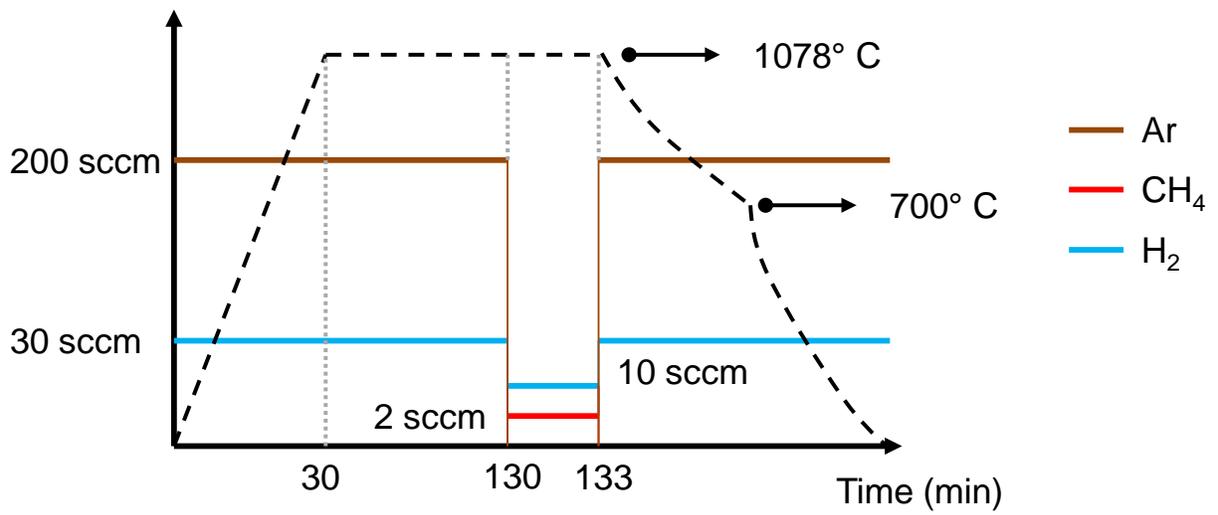
Figure 19. Typical low pressure CVD growth conditions using methane as a carbon source. The sharp decrease in temperature at 700° C is due to the opening of the split-hinge furnace.
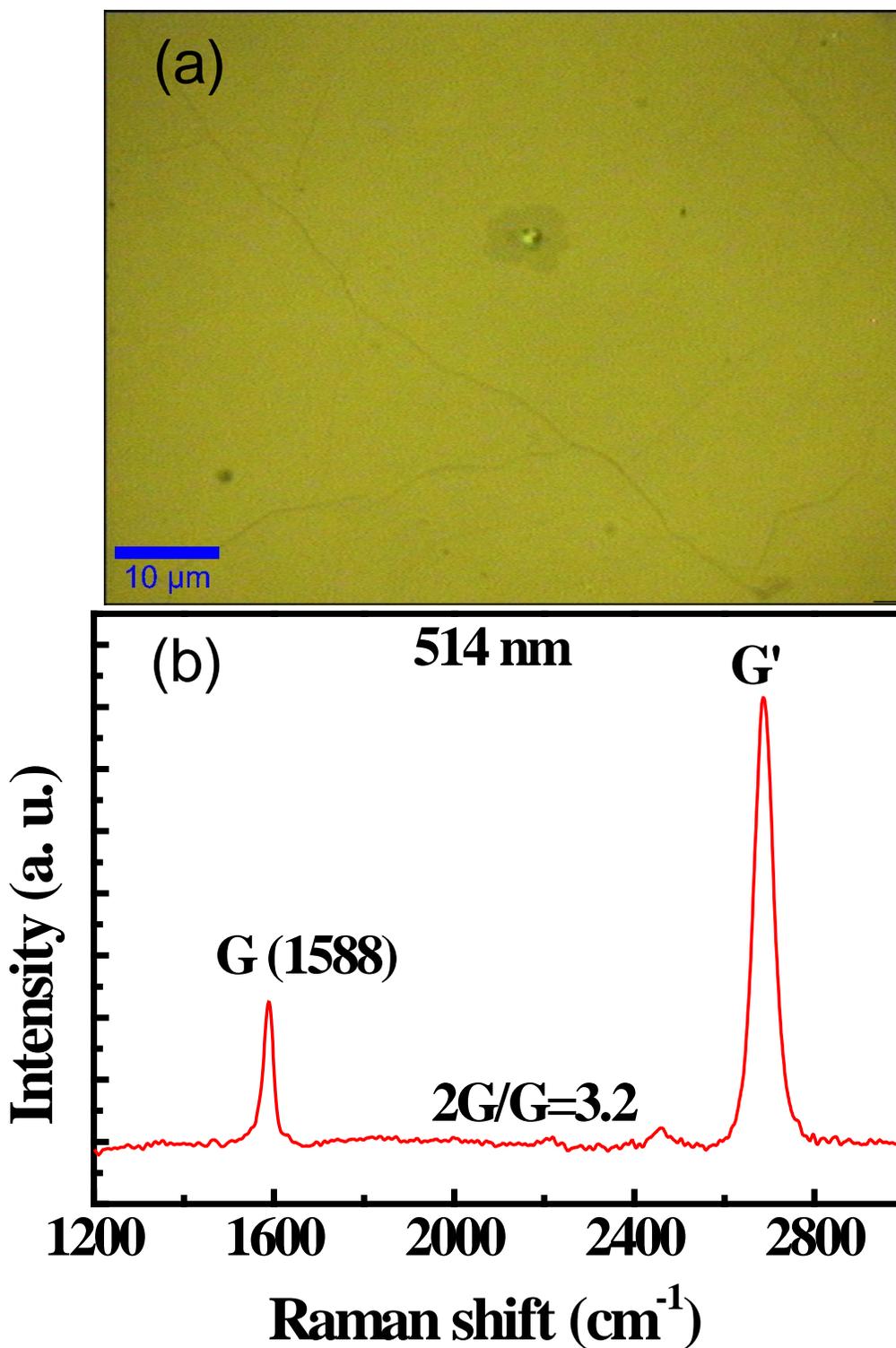
Figure 20. Monolayer graphene characterization (a) Optical Image of monolayer graphene after transfer to a SiO$_2$ substrate. (b) Raman spectra showing typical monolayer graphene signature. Note the lack of a D-band.
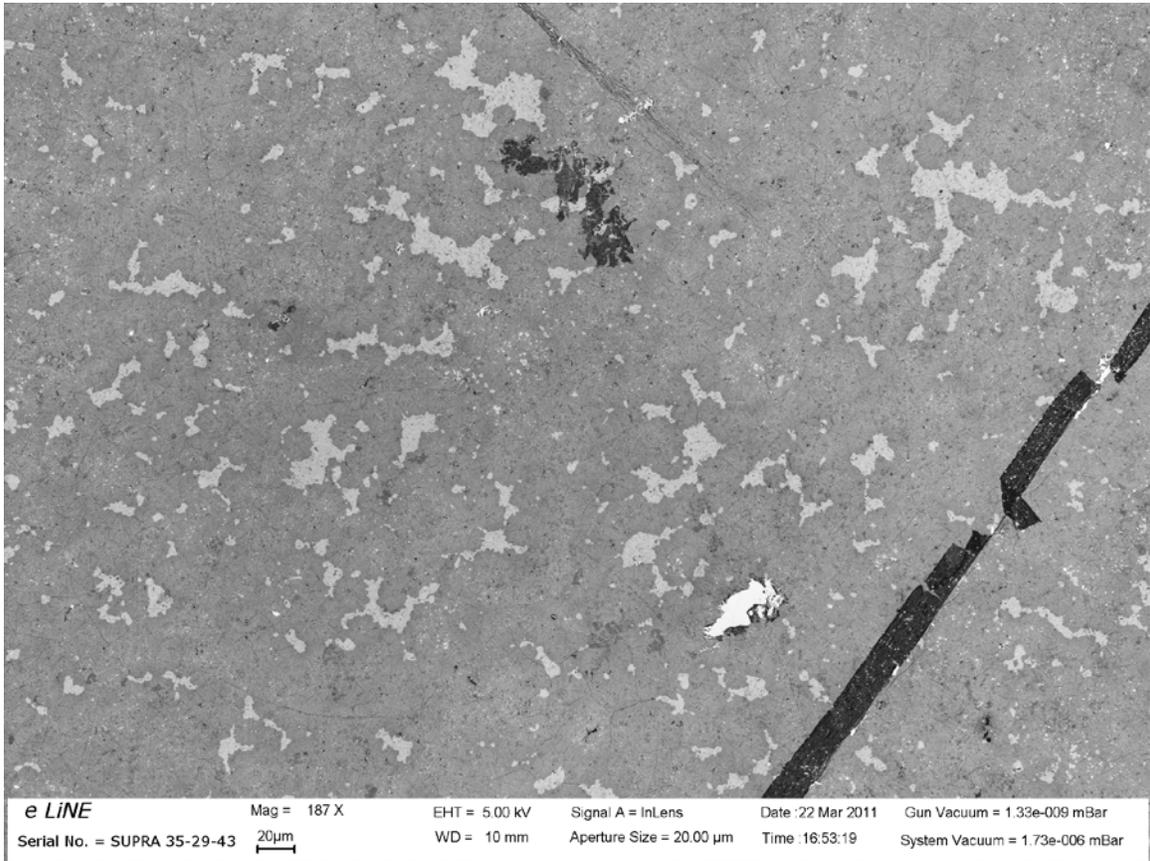
Figure 21. SEM image of graphene on SiO$_2$. Light areas are monolayer graphene while darker regions indicate regions of few/multi layer graphene.

3.2.2 Graphene Substrate Transfer

Poly(methyl methacrylate) (PMMA) in 4% Anisole was spin-coated on the post-graphene growth Cu foil, or post CNT-growth Si/SiO$_2$ sample at ~1000 rpm for 30 seconds. During CVD growth graphene is grown on both the polished surface of the Cu foil, as well as the rough back side. To remove the back-side graphene growth prior to etching away the Cu, the backside was etched using 20 W oxygen plasma for 5 seconds (O$_2$ flow rate of 5 sccm, P ~ 480 mtorr). The Cu foil was then etched using a ~.01 M solution of ammonium persulfate ((NH$_4$)$_2$S$_2$O$_8$) in DI water by floating the foil/PMMA on the surface of the etchant. For 100 µm Cu foil, etching required the foil to float on the surface of the etchant for up to 12 hours. After Cu foil is completely etched away, the PMMA/graphene remains floating on the surface due to the hydrophobic nature of moth materials. Next, the PMMA with graphene or SWCNT was soaked repeatedly in DI water baths by transferring the PMMA using a rigid and clean Si/SiO$_2$ sacrificial substrate. After soaking in the final clean DI bath for at least 12 hours, the PMMA was 'scooped' onto the final desired substrate. The substrate was placed vertically to allow residual water to drip from the substrate while drying in an oven at 70° C for 15 minutes. The dried sample was then placed on a hot plot set to 155° C for up to 24 hours to improve adhesion of the graphene with the Si/SiO$_2$ substrate. After removing and rethermalization with ambient environment, the samples were soaked in acetone for 30 minutes in two separate baths. Critically, we found that blow drying directly after acetone dipping improved adhesion when compared to the typically used Acetone/IPA/DI water soaking employed for clean samples.

After checking the quality of the graphene transfer in an optical microscope, the graphene substrate was typically baked for another 3-4 hours on a hot plate set to 150° C. Cleanliness of the graphene, including presence of residual PMMA was found to be more dependent upon the quality and crystallinity of the graphene film, and not the cleaning procedure.

3.2.3   Raman Spectroscopy of Graphene

Graphene grown under different polishing and growth conditions was characterized with resonant Raman scattering (Renishaw) and confocal Raman spectroscopy. Figure 22 shows Raman data for monolayer, bilayer with weak coupling, Bernel-stacked bilayer graphene, and twisted bilayer on the same sample grown via atmospheric pressure TCVD. Monolayer graphene Raman spectra is characterized based on the magnitude and shape of the second-order G' (~2700 cm^{-1} using 2.41 eV laser excitation) and G (1580 cm^{-1} using 2.41 eV laser excitation) bands. The G' mode is a 2-phonon (iTO) double resonance process, while the D-band (1350 cm^{-1} using 2.41 eV laser excitation) results from one elastic scattering event originating from a defect and a second inelastic (iTO) phonon.[133] The G-band is a result of a doubly degenerate zone center mode, and is actually the only first order Raman process observed in graphene.[134] G' band is often referred to as the 2D band since the frequency is roughly half that of the G', although they are phenomenalogically different, and the G' band can have a nonzero magnitude even in non-defective samples and away from sample edge. Examining fig. 22 carefully, we observe that the G' band in monolayer graphene and bilayer weakly-coupled graphene follows a single Lorentzian line shape. Conversely, the electronic and phonon bands split into two bands for Bernel (AB) stacked bilayer graphene. The broader G' band is thus a summation of 4 Lorentzian's reflecting the interaction of these sub bands.

The graphene sample measured and mapped in fig. 22 was grown on unpolished Cu foil with a slightly increased hydrogen content, resulting in about 90% bilayer growth. Such sample is not desirable for GNRs discussed in section 3.3, but is a strong demonstration of the nondestructive characterization capabilities of Raman spectroscopy of graphene. Raman data can also give basic information about the crystallinity and overall quality of monolayer and bilayer graphene. The D-band, which is almost unnoticeable in fig. 20, can be very significant in samples that are defective as in fig. 23.
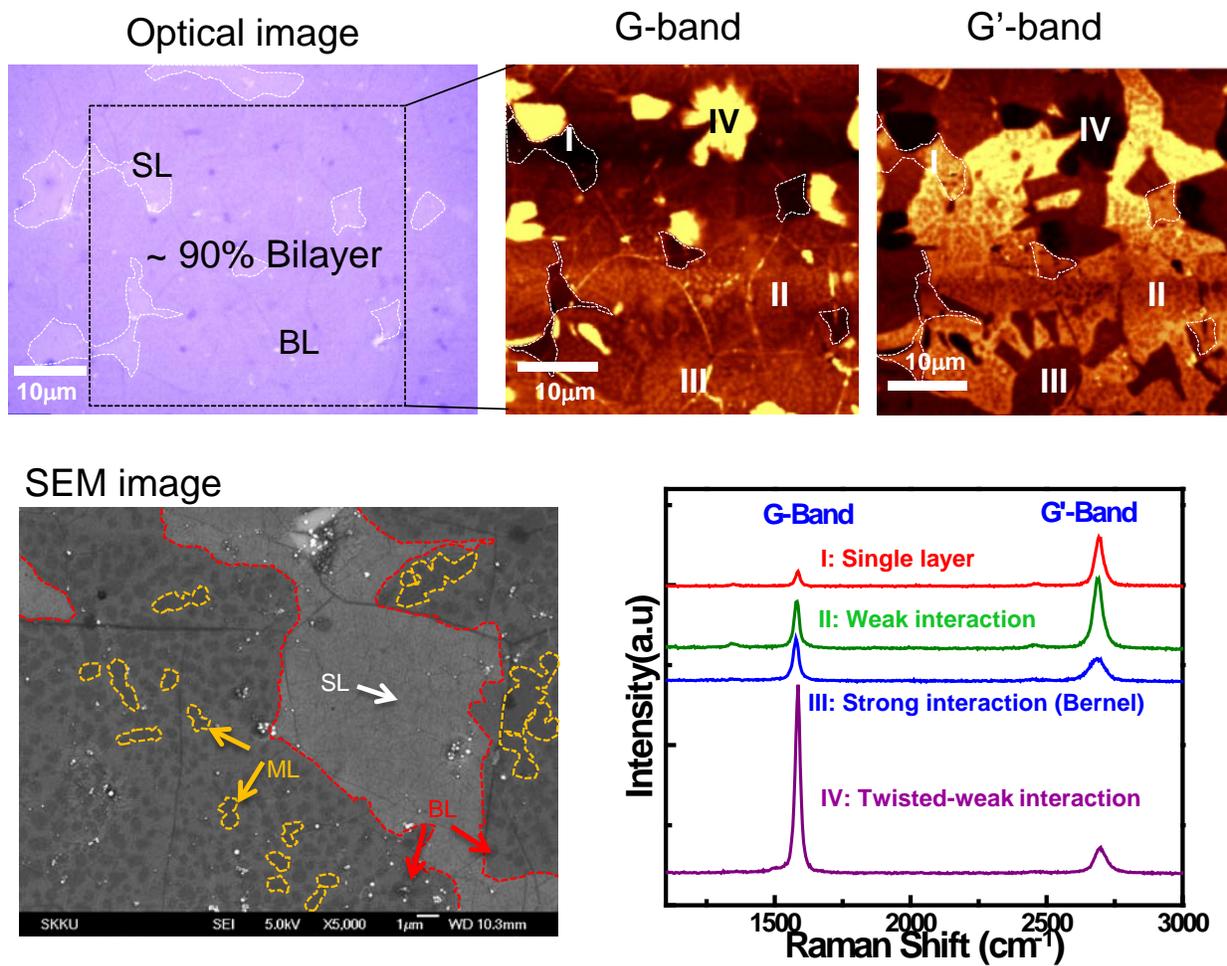
Figure 22. Bilayer graphene growth and interlayer-coupling variations. (a) Optical image of 90% bilayer graphene grown on Cu foil. (b) Confocal Raman mapping showing the inter-domain and cross-domain coupling differences via the G and G' bands. (c) SEM image of typical mixed-layer graphene growth sample. (d) Raman spectra indicating a stacking-order difference from various regions of (b).
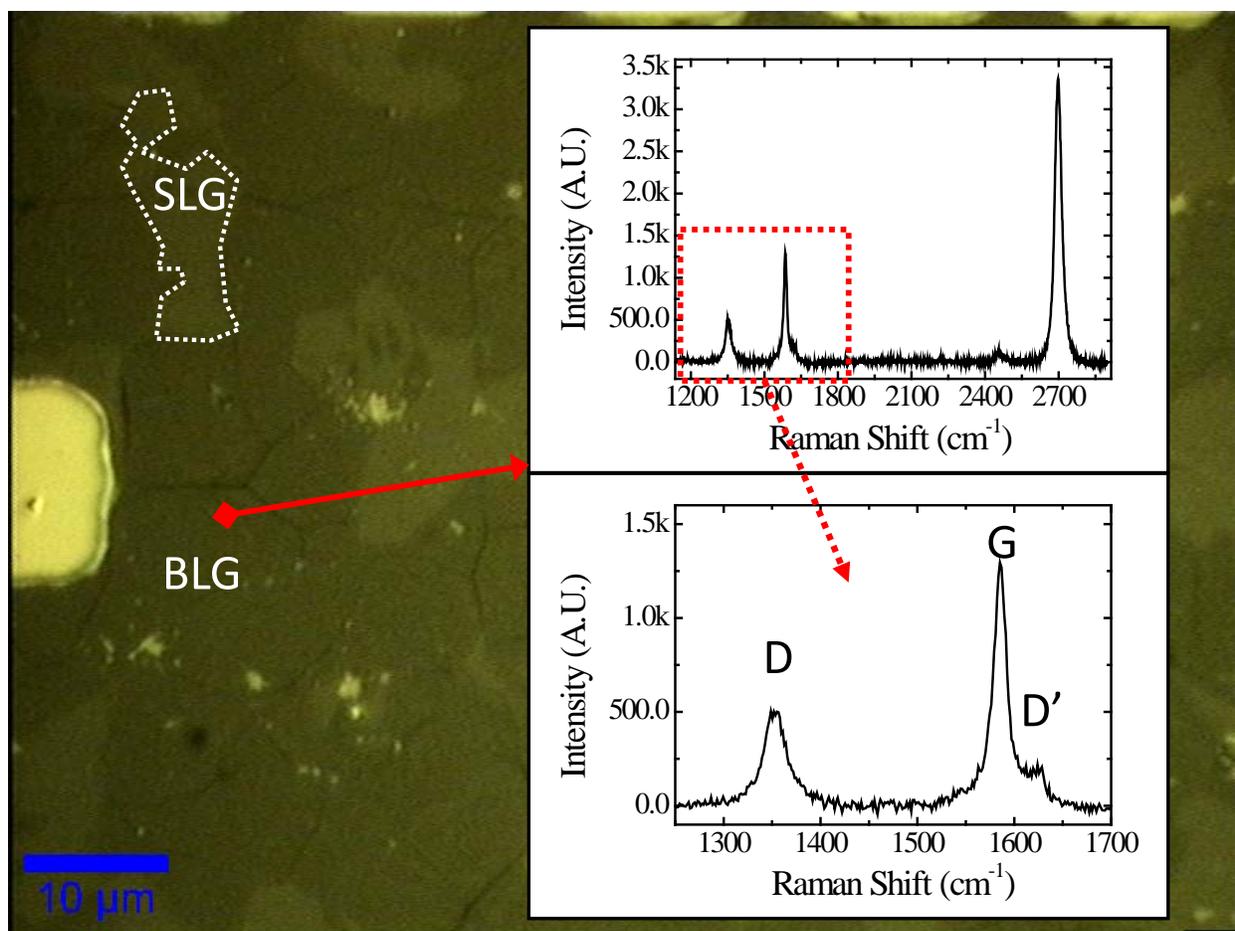
Figure 23. Defective bilayer graphene Raman signature. (a) Optical image shows graphene transferred onto SiO$_2$ substrate with electrodes. Roughly 90% is BLG. While the top layer is growing, the bottom layer is damaged by high temperature hydrogen etching. The resulting defects from the bottom layer can be seen in the appearance of a large 'D' peak in the Raman spectrum.

3.3 GRAPHENE NANORIBBON FIELD EFFECT TRANSISTORS FABRICATED FROM UV IRRADIATION OF CNT-MASKED GRAPHENE

3.3.1 Introduction

Graphene is an excellent platform for examining physics associated with quantum electrodynamics[105,135,136] and its high mobility shows promise in monolithic microwave integrated circuits found in communications applications[115,137] However, without an electrical band gap, graphene has limitations in the application of logic switching due to a very poor field effect on/off ratio. Formation of a transport gap/bandgap allows more efficient field effect carrier modulation in graphene. One manner of opening an electrical transport gap is via inducing lateral confinement by patterning graphene nanoribbons (GNR). [125,128,138,139]

Reducing GNRs to widths of 5-10 nm, where quantum confinement and coulomb blockade effects induce a large transport gap, challenges current minimal-width limitations in electron beam lithography.[126,127,130-132,140,141] Organic lithography dimensions are limited by the length of the molecular polymer chains, while inorganic resist patterning is limited by the minimum beam with achievable from the SEM column. To overcome these critical dimension limits, other methods incorporating graphene wrinkles,[130] dense and aligned block copolymer masks,[142] CNT unzipping,[143] and electrical sculpting[144] have been utilized to pattern GNRs narrower than 10 nm in width. CNT Unzipping aside, each of these novel methods are limited by unpredictable size distributions and small G_{on}/G_{off} ratios. Conversely, CNT unzipping promises smaller GNR widths because critical dimensions are determined by the initial tube diameter.

However, previous CNT unzipping procedures are limited by the need to first unzip the CNT into a GNR, and then disperse the resulting GNR onto a desired substrate. Unzipping results in better optimal performance over other methods discussed above, but chemical etching and dispersion methods often result in misoriented GNR that can be easily damaged during dispersion.[145,146]

In light of these technical challenges, in this letter we examine the effect of UV on graphene in an oxygen environment, and show that by masking single layer graphene with CNT as a sacrificial mask, ultra-narrow GNRs with room temperature G_{On}/G_{Off} exceeding 10^4 can be fabricated. The results of UV-irradiation on CNT-masked graphene are compared with UV exposures of CNTs and graphene separately. Results indicate that UV irradiation slowly etches both graphene and CNTs, but due to the CNT-masking in the hybrid samples, GNR can be fabricated when exposure time is controlled.

3.3.2 Fabrication and UV Irradiation

Graphene growth was done using low pressure-chemical vapor deposition (LP-CVD) on Cu foil using methane as the feed gas, similar to previous work.[147] Using standard floating PMMA methods, the graphene was transferred to an Si (500 μm)/SiO$_2$ (300nm) wafer with prefabricated probe-able Cr (10nm)/Au (70 nm) pads. Secondly, long and aligned SWCNTs were grown on a separate sacrificial Si/SiO$_2$ substrate using laminar flow thermal CVD using 0.001 M FeCl$_3$/Ethanol catalyst solution as reported previously.[89] Next, PMMA was spin coated on the SiO$_2$/CNT wafer surface. The sacrificial SiO$_2$ layer was etched away with a 25% HF solution, leaving the aligned SWCNTs attached on the bottom of the PMMA film. The SWCNTs were

then transferred onto the graphene surface. E-beam lithography/evaporation was used to fabricate Cr/Au source/drain electrodes with graphene/CNT traversing the contacts. To define the channel region of future GNRs, a sacrificial 20 nm thick Nickel film was deposited on the SWCNT/graphene across source/drain electrodes. All uncovered SWCNT/graphene were etched by exposing the sample to 20 watt oxygen plasma for 10 seconds. The protective Ni layer was subsequently etched with an $FeCl_3$-based etchant, leaving source and drain electrodes connected via SWCNT/graphene. For GNR patterning, SWCNT/graphene were placed in a closed chamber and 100 sccm of 99.999% O_2 flowed for 30 minutes to purge humidity and residual gases. While maintaining the O_2 flow, UV irradiation was done with a 20 mW/cm^2 low-pressure Hg lamp with 254 nm (90%) and 185 nm (10%) emission. Electrical measurements of GNR were performed prior to irradiation, and once again after 1 hour and 2 hours total UV exposure. AFM scans were also performed prior to irradiation and after a total of 2 hours of UV.

3.3.3   Characterization and Discussion

Electrical measurements of pristine SWCNT/graphene are shown in figure 24a. A V-shape G_{sd}-V_g response is observed, with minimum G_{sd} occurring at V_{Dirac} ~10V, similar behavior to a slight p-doped graphene on SiO_2 substrate. Therefore, CNT influence on conductance is assumed to be minimal due to both a large conductivity of pristine graphene, and small 1 mV applied potential. Figure 24b shows G_{sd} -V_g response after 1 hour of UV irradiation. No conductance minimum is observed although overall graphene conductance decreased by a factor of ~10^2 for all V_g. Further UV exposure decreased the off-state conductance 7 orders of magnitude from pristine, while on-state conductance decreased by ~5 x 10^3 , as seen in figure 24c.

Although the on/off ratio in Fig. 24c is greater than 10^3, the mechanism for the improved performance of CNT/graphene hybrid structure is unclear. As aforementioned, it seems that the contribution of CNT for channel conductance is insignificant because of the existence of a Dirac point. However, in Figs. 24b and 24c, it is not clear how monolayer graphene and CNT are contributing to the channel conductance. To determine the source of the G_{sd}-V_g dependence on UV exposure time, we independently examine the effects of UV irradiation by fabricating separate graphene-only FETs and on CNT-only FETs. These results are then compared with characteristics of the CNT-graphene hybrid devices.

Graphene FETs and CNT-FETs were fabricated with Cr/Au contacts and 2 μm channel lengths, equivalent to the GNR samples. Considering CNT-FETs first, G_{sd}-V_g measurements were performed in the pristine (non-UV irradiated) state and then as a function of UV irradiation time as shown in figure 25a. It was found that up to 10 minutes of UV exposure, CNT-FET clearly showed off-states near a gate bias of 20V. However, after 1 hour UV irradiation, all samples became insulating regardless of original metallicity. To clarify whether device failure resulted from break-junctions, complete etching, or CNT flattening, AFM topography scans were performed on a CNT-FET exposed to UV for 1 hour. In Fig. 25b, we observed bright lines running in a certain direction (indicated by arrows) that are SWCNTs grown by thermal SWCNT.
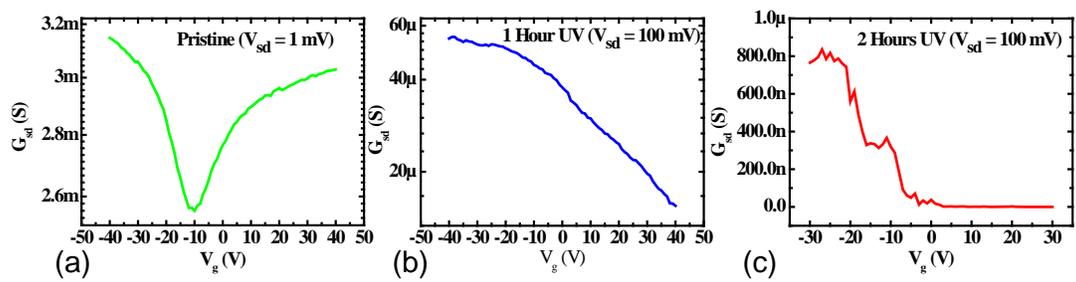
Figure 24. Electrical data for GNRs. (a-c) G_{sd}-V_g data of a GNR device as a function of UV exposure time.
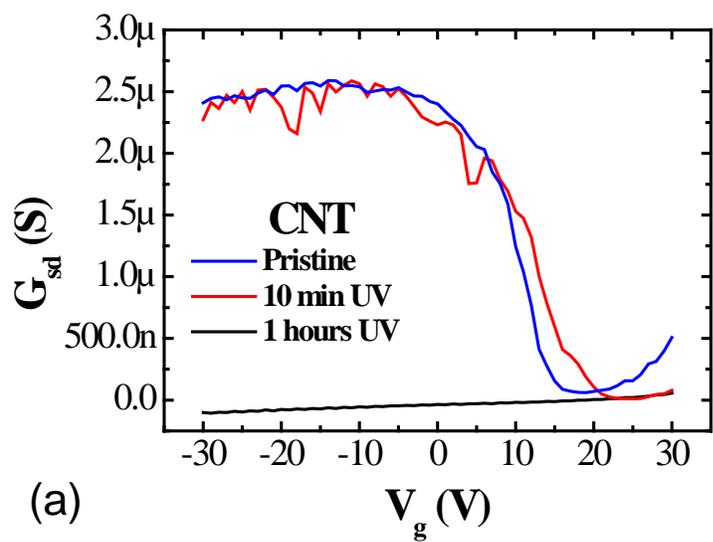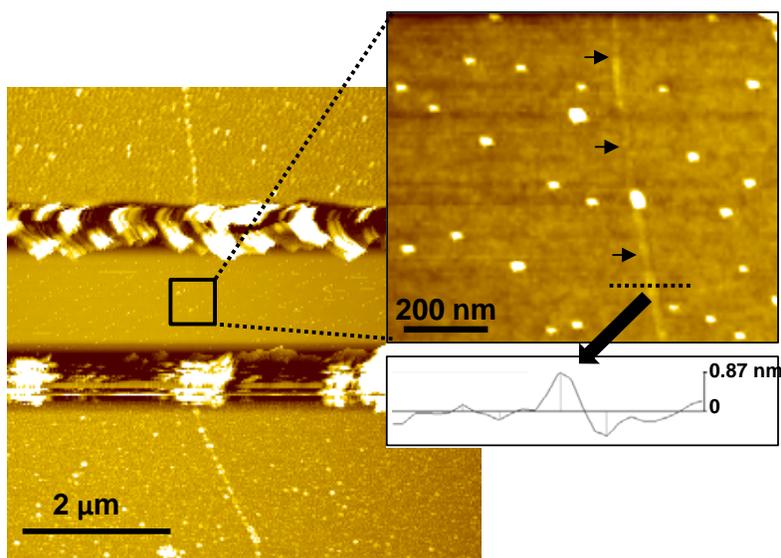
Figure 25. AFM and electrical analysis of CNT FETs. (a) G_{sd}-V_g as a function of time for CNT-FETs and (b) AFM topography of a CNT device after 2 hour of UV exposure time. Post UV CNT height < 1 nm indicates ozone etching.

As we zoomed in, we found that those SWCNTs were truncated (inset of Fig. 25b), which is attributed to inhomogeneous oxidation, and showed height of between 0.4 nm and 1 nm. The result indicates that SWCNTs are under an oxidative etching, because pristine tube diameters in our CVD process are 1.5 - 2 nm From these results, partial CNT etching occurs and intrinsic CNT electrical properties are not the source of the G_{sd}-V_g curves in figure 24. Therefore, we expect that exposing SWCNT to UV caused a gradual oxidative erosion of SWCNTs by oxygen radicals, and contributed to the termination of conducting path through SWCNT networks. As a result, after one hour, the channel conductance solely depends upon grapheme channel in case of CNT/graphene hybrid devices.

The same oxidation procedure was applied on graphene-FETs. Figure 26a shows G_{sd}-V_g before and after the UV exposure. It was observed that all samples become insulating after 1 hour irradiation. Figure 26b shows the surface topography in the pristine state while figure 26c shows the same area after 2 hours of UV exposure. Two notable changes were observed: Firstly, the graphene surface roughness increased, and is etched into nanoscale islands. Secondly, a larger portion of wrinkles clearly appear to remain even after the 2 hours of UV irradiation, which is consistent with previous work.[141] However, since no GRP-FET remained conducting after even 1 hours UV, these domain-boundary wrinkles cannot be the source of the FET response in the UV irradiated CNT/graphene samples. Furthermore, the clear etching of monolayer graphene precludes UV irradiation-induced GO_x formation as the cause of the improved G_{On}/G_{Off}.

To compare with each CNT and graphene result, AFM scans were also performed on 2 hour UV-irradiated CNT-graphene devices, as shown in figure 27. As in figure 26b, monolayer graphene is etched into nanoscale islands, which is more clearly shown in the inset of figure 27 (circular dotted lines). Large wrinkles resulting from Cu domain-boundaries during growth are etched into a very dense groupings of disconnected graphene islands. The location of the etched CNTs, which are distinguishable from the graphene wrinkles by strong parallel alignment, are denoted by two white dotted parallel curves running horizontally in figure 27. While topologically similar on a large scale, UV-irradiated graphene wrinkles and CNTs, closer analysis (square dotted outline in figure 27 inset) shows that the graphene wrinkles are actual highly discontinuous on a sub-micron scale (make it more outstanding. it is important).
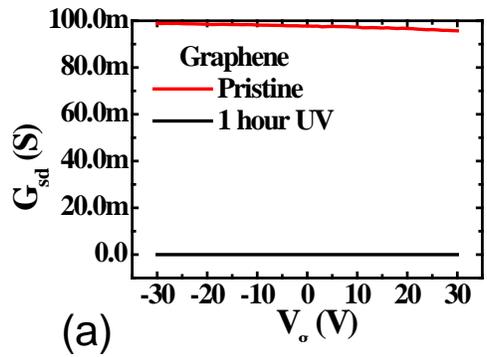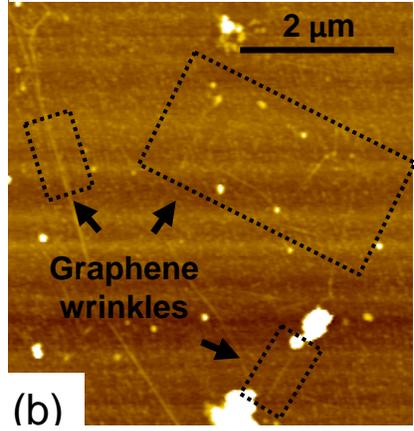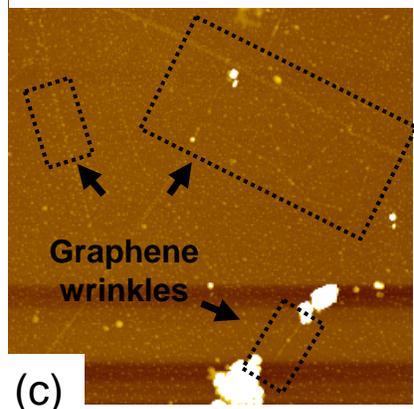
Figure 26. AFM and electrical analysis of Graphene FETs. (a) G_{sd} -V_g measurement of graphene samples as a function of UV exposure time. AFM topography of graphene (b) before and (c) after 2 hours of UV exposure. Graphene domain boundary wrinkles remain after UV irradiation, while monolayer graphene is etched into nano-islands.

In demonstrating that: (i) monolayer graphene and CNTs are slowly etched by UV irradiation in an oxygen environment, (ii) graphene wrinkles are highly discontinuous yet structurally remain after UV etching (but do not contribute to the conductance), and (iii) by showing that graphene-FETs and CNT-FETs become insulating after ~1 hour of UV exposure, it can be concluded that the improved on/off ratio and the formation of an off-state in the conductance sweeps results from formation of GNRs underneath the aligned CNTs. This is justified because although CNTs are partially etched by the UV irradiation and electrical discontinuous, AFM images in figure 25b do indicate that structurally the CNT remains intact. The resulting graphene strip under the CNT is thus patterned into an ultra-narrow GNR whose width is probably comparable to the CNT diameter of 1.5~2 nm. This suggests that the UV time-evolution shown in figure 24b would then represent a partial etching of the graphene/CNT structure, while figure 24c would be consistent with formation of clear transport gap and GNR thinning to nm dimensions. We note that a final channel width of < 10 nm is a 10^4 reduction in dimension from the initial 50 µm width, which is the same order of magnitude decrease in G_{On} observed between figure 24a and 24c.

To further analyze these ultra-narrow GNRs, we used a vacuum probe station with an open cycle LN2 feed through to measure cryogenic electrical properties of GNR FETs. G_{sd} - V_g measurements in figure 28a and 28c show two devices with G_{On}/G_{Off} ratio of 10^3 and $>10^4$, respectively, at room temperature. At 80K, the device from figure 28a showed an order of magnitude decrease in conductance for both the on-state and off-state as depicted in figure 28b. Critically, we also observed conductance fluctuations occurring when the device is switching between the on/off state. G_{On}, however, are consistent, always flattening out to produce on-state

resistance values of ~ 1.25 MΩ. The G_{sd} - V_g response in figures 28a (300K) and 28b (80K) indicate that current fluctuations also have no clear temperature dependence. Previous studies have shown via coulomb blockade spectroscopy and Dirac point mapping that inhomogeneous puddles of charge exist in graphene over length scales of 10-20 nm.[148] GNRs have weak coulomb screening and an imperfect edge structure, and thus the noisy electric response is attributed to perturbation by the charge puddles.

3.3.4   Conclusion

The method presented and corresponding GNR results demonstrate a unique method to fabricate GNR using CNT as a UV-irradiation mask. The GNR have excellent G_{On}/G_{Off} greater than 10^4. With careful time control, device scalability could be achieved and ribbon density controlled by varying the CVD growth conditions of the CNT or use of densely dispersed CNTs.[149] We further note that after considering previous work with UV-based oxidation and etching procedures, the conditions described are highly dependent upon the humidity, chamber design, UV intensity, and temperature.[150]
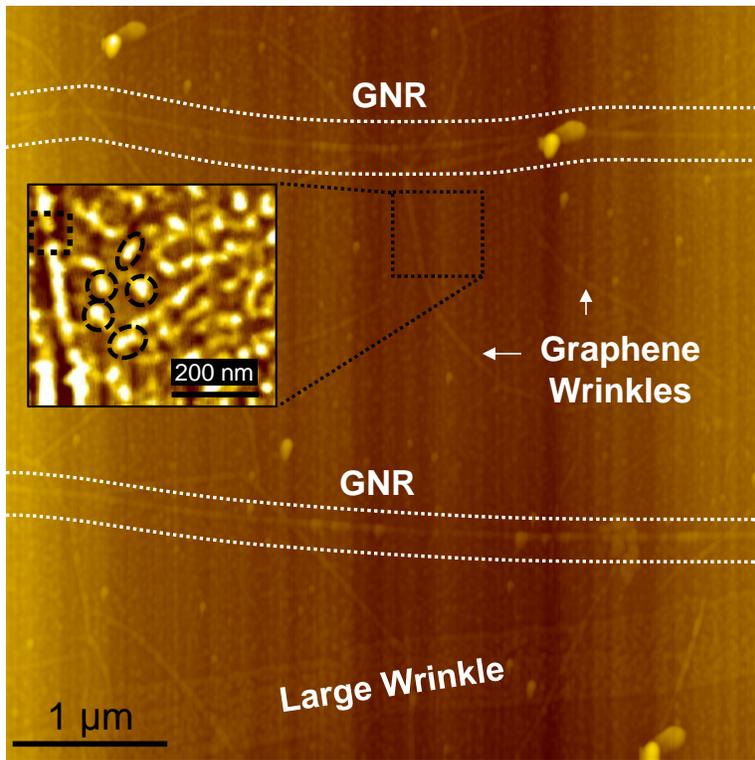
Figure 27. AFM Characterization of a CM-GNR FET after 2 hours of UV irradiation. Large wrinkles are etched into dense disconnected islands. GNR indicated by horizontal white lines.
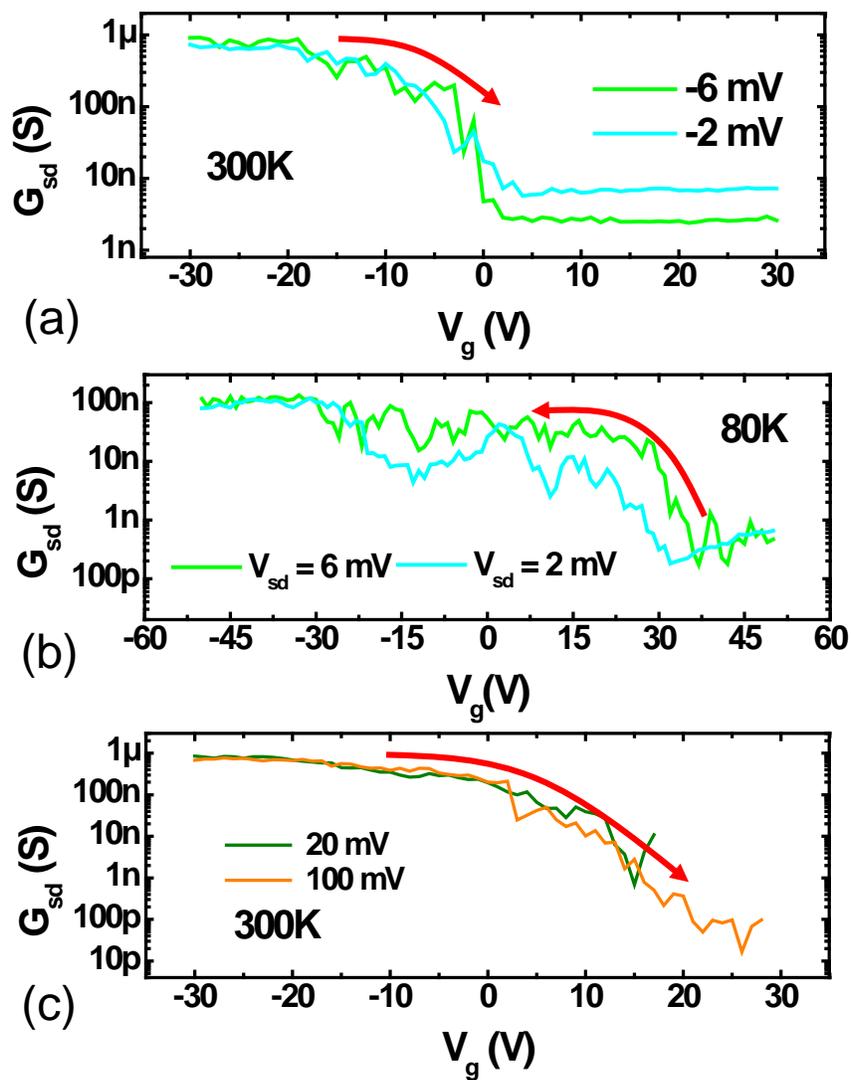
Figure 28. Field effect measurements of GNR transistors. (a) Room temperature and (b) 80K low temperature G_{sd}-V_g measurement of the same device. (c) Room temperature G_{sd}-V_g sweep of a second device having on/off ratio of $\sim 5 \times 10^4$. Red arrows denote sweep direction.

4.0   SUMMARY AND OUTLOOK

The work presented here includes significant advances in the understanding of the nature of mesoscopic contacts to nanoscale objects. We now have an improved phenomenological understanding of contact physics between CNT and metal species based on quantitative measurements of the energy barrier heights on the same CNT. From these measurements, a new non-planar dipole model nicknamed the SIC or Surface Inversion Channel model was proposed. We also observed, for the first time, a contact-dominant BTB tunneling mechanism in CNT FETs.

In addition to a new model of band alignment at the metal-CNT contacts, we were also able to formulate a TFE (thermionic field emission)-based model to describe the saturation current and contact resistance of devices purely based on metal type and work function. The results of each of these studies has increased validity due to the devices all being fabricated on one single ultra long CNT. Furthermore, the TFE model was based on a statistical analysis of almost a hundred devices on a single CNT to test the validity and prove the above TFE model. Using a similar TFE model, current rectification or "Anisotropy" can be predicted in CNT Schottky diodes based on the difference in metal work function of the hetero-metal contacts. The work on CNT Schottky diodes also demonstrated a novel switchable polarity CNT Schottky diode.

The work provides a vastly improved framework for understanding contact related properties in CNT FETs. Future improvements in devices and scalability may dependent moreso on improvements in CNT growth, positioning, and diameter/Chirality control.[151,152] These factors overshadow the ability to fabricate high performance electrical devices due to the maturity of the research field.

Graphene, conversely, remains a very hot topic with many unanswered questions - particularly involving GNR and bilayer graphene. Graphene growth has advanced steadily, and it is foreseeable that centimeter sized single-domain growth on Cu will become standard in research labs across the globe.[123] Our growth work here considered issues relating to the Cu substrate. We were able to lower sheet resistances and limit bilayer graphene growth by using a simple hand polishing method. Ultimately, however, graphene is a semimetal with limited application in FET switching devices. One possible route relying on CNT as a mask to intense UV irradiation of graphene was proposed and analyzed in this thesis. The GNR displayed excellent on/off ratios exceeding 10^4 without the need for top down lithography processes. One possible drawback is that the proposed method hinges on the ability to grow dense CNT arrays and cleanly transfer to graphene. Related issues are topics for future exploration and may allow magnitude increases in the on current density in such devices. Use of shorter channel lengths or larger diameter CNTs are two other possible routes to increase current densities to useful levels.

4.1 PUBLICATIONS

First Author:

1. **Perello, D. J.**; Chae, S.H.; Bae, J.J.; Ta Quang, H.; Lim, S. C.; Lee, Y. H.; Yun, M. Graphene nanoribbons fabricated using carbon nanotubes as an etch mask. In preparation

2. **Perello, D. J.**; Lim, S. C.; Chae, S. J.; Lee, I.; Kim, M.; Lee, Y. H.; Yun, M. Thermionic Field Emission Transport in Carbon Nanotube Transistors. ACS Nano 2011, *5* (3), 1756.

3. **Perello, D. J.**; ChuLim, S.; Chae, S. J.; Lee, I.; Kim, M.; Lee, Y. H.; Yun, M. Anomalous Schottky Barriers and Contact Band-to-Band Tunneling in Carbon Nanotube Transistors. ACS Nano 2010, 4 (6), 3103-3108.

4. **Perello, D. J.**; Lim, S. C.; Chae, S. J.; Lee, I.; Kim, M.; Lee, Y. H.; Yun, M. Current anisotropy of carbon nanotube diodes: Voltage and work function dependence. Applied Physics Letters 2010, 96 (26), 263107-3.

5. **Perello, D. J.**; Yu, W. J.; Bae, D. J.; Chae, S. J.; Kim, M. J.; Lee, Y. H.; Yun, M. Analysis of hopping conduction in semiconducting and metallic carbon nanotube devices. Journal of Applied Physics 2009, 105 (12), 124309-5.

6. **Perello, D.**; Dong, J. B.; Kim, M. J.; DongKyu, C.; Seung, Y. J.; Bo, R. K.; Woo, J. Y.; He, Y. L.; Minhee, Y. Quantitative Experimental Analysis of Schottky Barriers and Poole-Frenkel Emission in Carbon Nanotube Devices. Nanotechnology, IEEE Transactions on 2009, 8 (3), 355-360.

7. **Perello, D.**; Woojong, Y.; Dong, J. B.; Seung, J. C.; Kim, M. J.; Young, H. L.; Minhee, Y. Pool-Frenkel emission and hopping conduction in semiconducting carbon nanotube

transistor. In Proc. SPIE - Int. Soc. Opt. Eng. (USA); SPIE - The International Society for Optical Engineering: USA, 2009; p 739907.

8. **Perello, D.** ,Kim M.J., Jeong S.Y., Kang B.R., Bae D.J., Lee Y.H. and Yun M. (2008). CNT-FET Schottky Barrier Devices Fabricated by E-beam Lithography. (Conference Proceeding) Microscopy and Microanalysis, 14(Suppl. 2), pp 410-411 doi: 10.1017/S1431927608083086.

9. **Perello, D.**; Kim, M.J. Cha, D.K.; Han, G.H.; Bae, D.J.; Jeong, S.Y.; Lee, Y.H., and Yun, M.H.; "Schottky barrier engineering in carbon nanotube with various metal electrodes", IEEE Review on Advances in Micro, Nano, and Molecular Systems, 2007

Co-Author:

1. Sang Hoon Chae, Woo Jong Yu, Dinh Loc Duong, **David Perello**, Hye Yun Jeong, Chaejeong Heo, Quang Huy Ta, Thuc Hue Ly, Xiangfeng Duan, Minhee Yun, and Young Hee Lee. Transferred wrinkled Al_2O_3 for highly stretchable and transparent graphene/carbon nanotube transistors, *Accepted*, Nature Materials, 2013.

2. Yushi Hu, **David Perello**, Minhee YunDeok-Hwang Kwon, Miyoung Kim. Variation of switching mechanism in TiO2 thin film resistive random access memory with Ag and graphene electrodes. Microelectronic Engineering, 2013, 104, 42–47

3. Hyunjoong Lee, Sanghoon Lee, Dai-Hong Kim, **David Perello**, Young June Park, Seong-Hyeon Hong, Minhee Yun, and Suhwan Kim. Integrating Metal-Oxide-Decorated CNT Networks with a CMOS Readout in a Gas Sensor. Sensors, 2012, 12, 2582-2597.

4. Yu, W. J.; Lee, S. Y.; Chae, S. H.; **Perello, D.**; Han, G. H.; Yun, M.; Lee, Y. H. Small Hysteresis Nanocarbon-Based Integrated Circuits on Flexible and Transparent Plastic Substrate. Nano Letters 2011, 2011, 11 (3), 1344–1350.

5. Yu, W. J.; Chae, S. H.; **Perello, D.**; Lee, S. Y.; Han, G. H.; Yun, M.; Lee, Y. H. Synthesis of Edge-Closed Graphene Ribbons with Enhanced Conductivity. ACS Nano 2010, 4 (9), 5480-5486.

6. Biswas, C.; Jeong, S. Y.; Lim, S. C.; Bae, D. J.; Lee, Y. H.; Shin, H. J.; Yoon, S. M.; Choi, J. Y.; Cha, O. H.; Jeong, M. S.; **Perello, D.**; Yun, M. Efficacious photocurrent generation and carrier transport by quantum dot decorated carbon nanotubes. Kafafi, Z. H., Lane, P. A., Eds.; SPIE: San Diego, CA, USA, 2008; p 705216.

7. Yushi Hu, **David Perello**, Usman Mushtaq, and Minhee Yun, "A single palladium nanowire via electrophoresis deposition used as a ultrasensitive hydrogen sensor", IEEE Transactions on Nanotechnology, 7 (6), pp693-699 (2008)

8. Jeong, S. Y.; Lim, S. C.; Bae, D. J.; Lee, Y. H.; Shin, H. J.; Yoon, S. M.; Choi, J. Y.; Cha, O. H.; Jeong, M. S.; **Perello, D.**; Yun, M. Photocurrent of CdSe nanocrystals on single-walled carbon nanotube-field effect transistor. Applied Physics Letters 2008, 92 (24), 243103.

9. Hur, T. B.; Kim, H. K.; **Perello, D.**; Yun, M.; Kulovits, A.; Wiezorek, J. Morphology and grain structure evolution during epitaxial growth of Ag films on native-oxide-covered Si surface. Journal of Applied Physics 2008, 103 (10), 103507-5.

10. Woo, J. Y.; Seung, Y. J.; Ki, K. K.; Bo, R. K.; Dong, J. B.; Minbaek, L.; Seunghun, H.; Gaunkar, S. P.; Pribat, D.; **Perello, D.**; Minhee, Y.; Jae-Young, C.; Young, H. L. Bias-

induced doping engineering with ionic adsorbates on single-walled carbon nanotube thin film transistors. New Journal of Physics 2008, 10 (11), 113013.

11. Seung, Y. J.; **Perello, D.**; Sung, J. K.; Jin, H. J.; Kang, B. R.; Woo, J. Y.; Dong, J. B.; Minhee, Y.; Young, H. L. Chirality-specific transport phenomena of isolated single-walled carbon nanotube. physica status solidi (b) 2007, 244 (11), 4204-4211.

12. Park, H. I.; Mushtaq, U.; **Perello, D.**; Lee, I.; Cho, S. K.; Star, A.; Yun, M. Effective and Low-Cost Platinum Electrodes for Microbial Fuel Cells Deposited by Electron Beam Evaporation. Energy & Fuels 2007, 21 (5), 2984-2990.

Conference Presentations (Oral)

1. "Thermionic Field Emission in Carbon Nanotube Transistors and Proposal of Surface Inversion Channel Model." MRS December 2010 (Boston)

2. "Pool-Frenkel emission and hopping conduction in semiconducting carbon nanotube transistor." SPIE August 2009 (San Diego)

3. "CNT-FET Schottky Barrier Devices Fabricated by E-beam Lithography" Microscopy and Microanalysis 2008 (Albuquerque)

Conference Presentations (Poster)

1. CNT Schottky Diode Anisotropy: Theoretical Model and Novel Application

2. Analysis of Contact Barriers and Hopping Conduction in Electron Irradiated Carbon Nanotube Devices. MRS Boston 2008 (Poster)

3. Fabrication and Characterization of Single-Wall Carbon Nanotube Contacts. MRS Boston 2008 (Poster).

4. Explicit Determination of Various Metal-dependent Contact Properties to Single-wall Carbon Nanotubes. MRS Boston 2007 (Poster).

APPENDIX A

CNT/GRAPHENE TIGHT BINDING BAND STRUCTURE CALCULATION

The carbon atoms in a graphene lattice are arranged hexagonally, each atom having exactly 3 nearest neighbors. Only the p_z electron interactions between atoms are considered in this estimation, due to lack of overlap or zero total overlap for all other s, p_x, and p_y electron wave functions. Beginning with Schrödinger's Equation:

$$H\Psi(k) = E(k)\Psi(k) \tag{A.1}$$

With H the Hamiltonian, E the energy eigenvalues, and $\Psi(k)$ the corresponding eigenfunctions. Each eigenfunction can be written as a linear sum of Bloch functions:

$$\Psi(k) = \sum_m c_m \Phi_m(k) \tag{A.2}$$

These Bloch functions are themselves written as linear sums of atomic wave functions. The graphene lattice contains a dual basis, and we shall denote the atoms in the first and second sub lattice by the subscripts "D" and "F". Normalized Bloch functions for the sub lattices therefore are:

$$\Phi_D = \frac{1}{\sqrt{N}} \sum_{R_D} e^{ik \cdot R_D} \phi(r - R_D) \tag{A.3}$$

$$\Phi_F = \frac{1}{\sqrt{N}} \sum_{R_F} e^{ik \cdot R_F} \phi(r - R_F) \tag{A.4}$$

With N = number of unit cells, and R_D and R_F the translational lattice vector. Solving the Schrodinger's equation, we substitute in the Bloch functions from equation (A.4) and multiply by Φ_D and Φ_F. The resulting linear equations are:

$$
\begin{aligned}
C_D[H_{DD}(k) - E(k)S_{DD}(k)] + C_F[H_{DF}(k) - E(k)S_{DF}(k)] = 0 \\
C_D[H_{FD}(k) - E(k)S_{FD}(k)] + C_F[H_{FF}(k) - E(k)S_{FF}(k)] = 0
\end{aligned}
\tag{A.5}
$$

With $H_{jn}(k) = \langle \Phi_j | H | \Phi_n \rangle$ and $S_{jn} = \langle \Phi_j | H | \Phi_n \rangle$ the Hamiltonian matrix elements and the overlaps of the Bloch functions, respectively. We simply the system of equations by noting that $H_{DD}(k) = H_{FF}(k)$, $H_{DF}(k) = H_{FD}^*(k)$, $S_{DD}(k) = S_{FF}(k)$, and $S_{DF}(k) = S_{FD}^*(k)$ and finding the nontrivial solutions for $E(k)$ that satisfy the 2 x 2 matrix determinant $\det[H - ES]$. This yields:

$$E(k)\pm = \frac{-(-2E_0 + E_1) \mp \sqrt{(-2E_0 + E_1)^2 - 4E_2 E_3}}{2E_3} \tag{A.6}$$

With E values as follows, with k variable dropped to ease notation:

$$
\begin{aligned}
E_0 &= H_{DD} S_{DD} \\
E_1 &= S_{DF} H_{DF}^* + H_{DF} S_{DF}^* \\
E_2 &= H_{DD}^2 - H_{DF} S_{DF}^* \\
E_3 &= S_{DD}^2 - S_{DF} S_{DF}^*
\end{aligned}
\tag{A.7}
$$

With $E(k)^+$ representing the valence band and $E(k)^-$ the conduction band of graphene. Next we will assume that interactions occur only between nearest neighbors. The quantity H_{DD} is solved first:

$$H_{DD} = \langle \Phi_D | H | \Phi_D \rangle = \frac{1}{N} \sum_{R_D} \sum_{R_{D'}} \langle e^{ik \cdot R_D} \phi_D(r - R_D) | H | e^{ik \cdot R_{D'}} \phi_D(r - R_{D'}) \rangle \tag{A.8}$$

The nearest neighbor assumption implies that for each R_D summed over the second has only R_D = $R_{D'}$, simplifying the equation greatly and allowing us to define a new constant ε_{2p} :

$$\varepsilon_{2p} = H_{DD} = \frac{1}{N} N \langle \phi_D(r - R_D) | H | \phi_D(r - R_{D'}) \rangle \tag{A.9}$$

The matrix element for the Hamiltonian between the D and F atoms is slightly more complicated, but begins with the expression:

$$H_{DF} = \langle \Phi_D | H | \Phi_F \rangle = \frac{1}{N} \sum_{R_D} \sum_{R_F} e^{ik \cdot (R_D - R_F)} \langle \phi_D(r - R_D) | H | \phi_F(r - R_F) \rangle \tag{A.10}$$

The first sum is simply over N atoms in the lattice, once again cancelling out the 1/N constant. The second sum, however, is done over the three nearest neighbors of each atom R_D. To perform this sum, the vector quantities for the three nearest neighbors (which are defined as $R_{1i,}$ R_{2i}, and R_{3i} here, with $R_{ki} = R_{B(ki)} - R_A$ and k indicating the number of neighbors (1) and i = 1, 2, 3) must be known. These are:

$$R_{11} = \frac{1}{3}(2a_1 - a_2) \qquad R_{12} = \frac{1}{3}(-a_1 + 2a_2) \qquad R_{13} = \frac{1}{3}(-a_1 - a_2)$$

Inserting into equation (A.10) above, and recognizing that the atomic wave functions are radial symmetric, the Hamiltonian matrix element becomes:

$$H_{DF} = \left(e^{ik \cdot R_{11}} + e^{ik \cdot R_{12}} + e^{ik \cdot R_{13}} \right) \langle \phi_D(r - R_D) | H | \phi_F(r - R_D - R_{11}) \rangle \tag{A.11}$$

Which can be further reduced by introducing the constant γ_0 and substituting in the vector constants for R_{11}, R_{12}, R_{13} :

$$H_{DF} = \gamma_0 \left(e^{-\frac{1}{3}ik \cdot (a_1 + a_2)} \right) \left(e^{ik \cdot a_1} + e^{ik \cdot a_2} + 1 \right) \tag{A.12}$$

γ_0 is typically referred to as the tight binding integral. Performing the same analysis for S_{DF}, we get:

$$S_{DF} = S_0 \left(e^{-\frac{1}{3}ik \cdot (a_1 + a_2)} \right) \left(e^{ik \cdot a_1} + e^{ik \cdot a_2} + 1 \right) \tag{A.13}$$

With the constant overlap integral $S_0 = \langle \phi_A | \phi_{B_{1i}} \rangle$. Finally, the resulting energy bands can solutions can be achieved by substituting the values of H_{DF} and S_{DF} (or conjugates) into the E(k) expression of equation (A.6) to get the result (in reciprocal lattice vectors $\mathbf{k} = k_1 \mathbf{k_1} + k_2 \mathbf{k_2}$)

$$E^{\pm}(k_1, k_2) = \frac{\varepsilon_{2p} \pm \gamma_0 \sqrt{3 + 2\cos 2\pi k_1 + 2\cos 2\pi k_2 + 2\cos 2\pi (k_1 - k_2)}}{1 \pm s_0 \sqrt{3 + 2\cos 2\pi k_1 + 2\cos 2\pi k_2 + 2\cos 2\pi (k_1 - k_2)}} \tag{A.14}$$

Note that an even simpler "tight binding approximation" can be performed by assuming that the overlap between atomic wave functions at different atoms is zero ($S_{DF} = 0$), and assuming $S_{DD} = 1$. This is a reasonable assumption and significantly reduces the complexity of the energy band equations by forcing $E_1 = 0$ and $E_3 = 1$.[153] This method is only accurate near the graphene k – points, however.

Note that the above derivation for graphene is identical to the CNT tight binding calculation, at least for the bands near the Dirac k-points. To take into account the CNTs circumference, simply adding a quantization conditions to the radial wave function quantitatively reproduces the semiconducting and metallic relationships described in Appendix B.

APPENDIX B

CARBON NANOTUBE CHIRALITY

The lattice structure, Brillouin zone and unit cell of CNT are defined in terms of graphene. Figure 29 shows the graphene honeycomb lattice with the reciprocal space vectors a_1 and a_2 defined. A graphene unit cell contains two atoms at the locations (in terms of a_1 and a_2) $\frac{1}{3}(a_1 + a_2)$ and $\frac{2}{3}(a_1 + a_2)$. These basis vectors are further used to define the structure of a SWCNT. SWCNT are classified and identified by interpreting the cylinder as a sheet of graphene wrapped via the Chiral vector. This Chiral wrapping vector is defined as:

$$c = na_1 + ma_2 \tag{B.1}$$

Where n, m defines the Chiral indices of the nanotube, and will become useful later when electrical properties are defined in terms of these values. The wrapping angle or Chiral angle of a CNT is defined as:

$$\cos(\theta) = \frac{(n_1 + n_2)}{2\sqrt{n_1^2 + n_1 n_2 + n_2^2}} \tag{B.2}$$

The Chiral angle is the angle between the basic vector a_1 and the Chiral vector c. Figure 29 can be seen for the graphical interpretation of this value. As can be inferred from the definition of the Chiral vector, the diameter of a SWCNT is simply the length of c:

$$d = \frac{|c|}{\pi} = \frac{|a_1|}{\pi} \sqrt{n_1^2 + n_1 n_2 + n_2^2} = \frac{a_0}{\pi} \sqrt{n_1^2 + n_1 n_2 + n_2^2} \qquad \text{(B.3)}$$
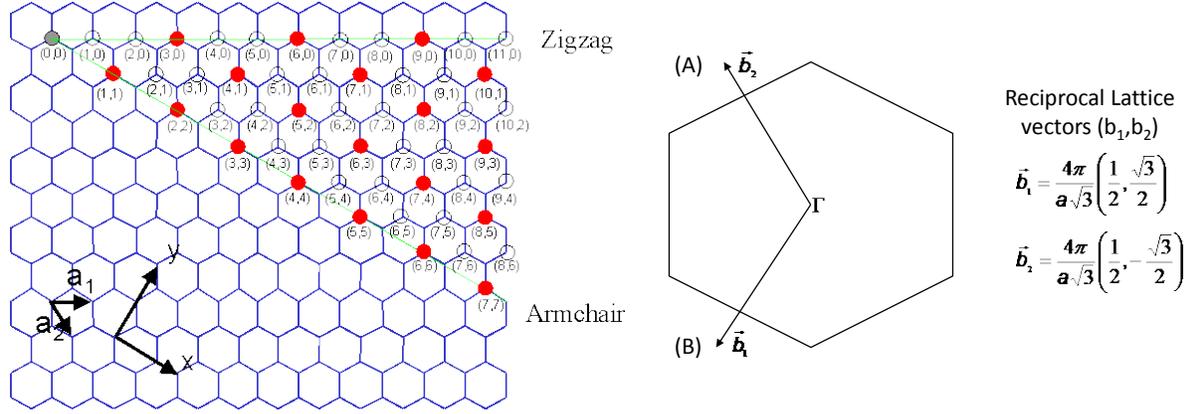
Figure 29. (a) Diagram of graphene with Chiral vector and wrapping angle used to construct CNT from graphene lattice [154]. (b) Graphene Brillouin zone with corresponding reciprocal lattice vectors defined.

Where $a_0 = |a_1| = |a_2|$. When discussing electronic band structure, quantities based upon the Chiral indices can be utilized in defining quantization conditions and other values. Further subcategories of carbon nanotubes are based on these indices, with each having unique characteristics: SWCNT are further divisible into three classifications dependent upon these Chiral indices: armchair, Chiral, and zigzag. Armchair tubes are those SWCNT with an index of (n,n) and are unique by their metallic character. Zigzag SWCNT denote those with (n,0) index and may be either semiconducting or metallic dependent upon the value of n. The remaining tubes are referred to as Chiral CNT, and can also have either metallic or semiconducting character. They are further defined by (in most cases) a very large unit cell.

99

APPENDIX C

THERMAL CHEMICAL VAPOR DEPOSITION SYSTEM

A TCVD system based on a three-zone Carbolite 24" hot-zone split-hinge furnace was built as shown in Figure 30. The furnace is capable of 1200° Celsius operation and was retrofitted in-house using fibrous alumina refractory board to fit common 50 cm diameter tubes. This tube size was chosen to limited turbulent flow in long, thin tubes, reduce flow rate requirements of feed gases, and for better uniformity of the temperature within the chamber. Gas flow rates are controlled using MKS Mass Flow Controllers and Control unit with feed gases methane (CH_4), hydrogen (H_2), and Argon (Ar). The flow ranges for each of these units is 1:50 sccm CH_4, 1:100 sccm (H_2), and 1:500 sccm (Ar). The system was fitted with ultra high vacuum capable ends (MTI Corporation), and all gas connections were made from ¼" Swagelok fittings to prevent leakage. The system was further formatted with a valve to switch between atmospheric and vacuum (~10^{-3} torr) operation. Atmospheric pressure is utilized primarily for CNT growth, while vacuum condition was found to be more idea for single-layer graphene.

Figure 30. TCVD system based on a split-hinge Carbolite furnace retrofitted with Al_2O_3 insulation to fit 50 cm quartz tubes. The system is interface to a computer using Labview (to the right of the visible furnace controller) with gas flow controlled using an MKS MFC system and flow controller. System is connect to roughing pump in this diagram although it can operate at atmospheric pressure by changing fittings.

APPENDIX D

ELECTRICAL CHARACTERIZATION

Low temperature measurements were performed in a closed cycle refrigerator over the temperature range 20 – 300 K. Electrical measurements were collected with a Keithley 236 (Source/Drain) and Keithley 237 (Gate/Drain) with automated Labview interface, or via Keithley 4200SC semiconductor analyzer.

BIBLIOGRAPHY

1. Iijima, S. Helical microtubules of graphitic carbon. *Nature* **1991,** *354*, 56-58.

2. Bethune, D. S.; Klang, C. H.; de Vries, M. S.; Gorman, G.; Savoy, R.; Vazquez, J.; Beyers, R. Cobalt-catalysed growth of carbon nanotubes with single-atomic-layer walls. *Nature* **1993,** *363* (6430), 605-607.

3. Kroto, H. W.; Heath, J. R.; O'Brien, S. C.; Curl, R. F.; Smalley, R. E. C60: Buckminsterfullerene. *Nature* **1985,** *318* (6042), 162-163.

4. Liao, X. Z. Effect of catalyst composition on carbon nanotube growth. *Appl. Phys. Lett.* **2003,** *82*, 2694-2696.

5. Saito, T.; Matsushige, K.; Tanaka, K. Chemical treatment and modification of multi-walled carbon nanotubes. *Physica B* **2002,** *323*, 280-283.

6. Li, Y. On the origin of preferential growth of semiconducting single-walled carbon nanotubes. *J. Phys. Chem. B* **2005,** *109*, 6968-6971.

7. Zuo, G.; Shen, R.; Ma, S.; Guo, W. Transport Properties of Single-File Water Molecules inside a Carbon Nanotube Biomimicking Water Channel. *ACS Nano* **2009,** *4* (1), 205-210.

8. Charlier, J.-C.; Blase, X.; Roche, S. Electronic and transport properties of nanotubes. *Rev. Mod. Phys.* **2007,** *79*, 677-733.

9. Freitag, M.; Steiner, M.; Naumov, A.; Small, J. P.; Bol, A. A.; Perebeinos, V.; Avouris, P. Carbon Nanotube Photo- and Electroluminescence in Longitudinal Electric Fields. *ACS Nano* **2009,** *3* (11), 3744-3748.

10. Ding, L.; Wang, S.; Zhang, Z.; Zeng, Q.; Wang, Z.; Pei, T.; Yang, L.; Liang, X.; Shen, J.; Chen, Q.; Cui, R.; Li, Y.; Peng, L. M. Y-Contacted High-Performance n-Type Single-Walled Carbon Nanotube Field-Effect Transistors: Scaling and Comparison with Sc-Contacted Devices. *Nano Letters* **2009**.

11. Durkop, T.; Getty, S. A.; Cobas, E.; Fuhrer, M. S. Extraordinary mobility in semiconducting carbon nanotubes. *Nano Lett.* **2004,** *4*, 35-39.

12. Perebeinos, V.; Tersoff, J.; Avouris, P. Mobility in semiconducting carbon nanotubes at finite carrier density. *Nano Lett.* **2006,** *6*, 205-208.

13. Latil, S.; Roche, S.; Charlier, J. C. Electronic Transport in Carbon Nanotubes with Random Coverage of Physisorbed Molecules. *Nano Letters* **2005,** *5* (11), 2216-2219.

14. Treacy, M. M. J.; Ebbesen, T. W.; Gibson, J. M. Exceptionally high Young's modulus observed for individual carbon nanotubes. *Nature* **1996,** *381* (6584), 678-680.

15. Sawano, S.; Arie, T.; Akita, S. Carbon Nanotube Resonator in Liquid. *Nano Letters* **2010,** *10* (9), 3395-3398.

16. Xu, Y. Q.; Barnard, A.; McEuen, P. L. Bending and Twisting of Suspended Single-Walled Carbon Nanotubes in Solution. *Nano Letters* **2009,** *9* (4), 1609-1614.

17. Ha, M.; Xia, Y.; Green, A. A.; Zhang, W.; Renn, M. J.; Kim, C. H.; Hersam, M. C.; Frisbie, C. D. Printed, Sub-3V Digital Circuits on Plastic from Aqueous Carbon Nanotube Inks. *ACS Nano* **2010,** *4* (8), 4388-4395.

18. DiLeo, R. A.; Castiglia, A.; Ganter, M. J.; Rogers, R. E.; Cress, C. D.; Raffaelle, R. P.; Landi, B. J. Enhanced Capacity and Rate Capability of Carbon Nanotube Based Anodes with Titanium Contacts for Lithium Ion Batteries. *ACS Nano* **2010,** null.

19. Wilson, N. R.; Macpherson, J. V. Carbon nanotube tips for atomic force microscopy. *Nat Nano* **2009,** *4* (8), 483-491.

20. Zhang, L.; Jia, Y.; Wang, S.; Li, Z.; Ji, C.; Wei, J.; Zhu, H.; Wang, K.; Wu, D.; Shi, E.; Fang, Y.; Cao, A. Carbon Nanotube and CdSe Nanobelt Schottky Junction Solar Cells. *Nano Letters* **2010,** *10* (9), 3583-3589.

21. Yu, M. F.; Lourie, O.; Dyer, M. J.; Moloni, K.; Kelly, T. F.; Ruoff, R. S. Strength and Breaking Mechanism of Multiwalled Carbon Nanotubes Under Tensile Load. *Science* **2000,** *287* (5453), 637-640.

22. Chang, C. C.; Hsu, I. K.; Aykol, M.; Hung, W. H.; Chen, C. C.; Cronin, S. B. A New Lower Limit for the Ultimate Breaking Strain of Carbon Nanotubes. *ACS Nano* **2010,** *4* (9), 5095-5100.

23. Ko, F. K.; Lam, H.; Titchenal, N.; Ye, H.; Gogotsi, Y. Coelectrospinning of Carbon Nanotube Reinforced Nanocomposite Fibrils. In *Polymeric Nanofibers*, 918 ed.; American Chemical Society: 2006; pp 231-245.

24. Charlier, J. C.; Blase, X.; Roche, S. Electronic and transport properties of nanotubes. *Reviews of Modern Physics* **2007,** *79* (2), 677-56.

25. Javey, A. Ballistic carbon nanotube field-effect transistors. *Nature* **2003,** *424*, 654-657.

26. White, C. T.; Todorov, T. N. Carbon nanotubes as long ballistic conductors. *Nature* **1998,** *393*, 240-242.

27. Gomez-Navarro, C.; Pablo, P. J. D.; Gomez-Herrero, J.; Biel, B.; Garcia-Vidal, F. J.; Rubio, A.; Flores, F. Tuning the conductance of single-walled carbon nanotubes by ion irradiation in the Anderson localization regime. *Nat Mater* **2005,** *4* (7), 534-539.

28. Bachtold, A. Aharonov-Bohm oscillations in carbon nanotubes. *Nature* **1999,** *397*, 673-675.

29. Ishii, H.; Kataura, H.; Shiozawa, H.; Yoshioka, H.; Otsubo, H.; Takayama, Y.; Miyahara, T.; Suzuki, S.; Achiba, Y.; Nakatake, M.; Narimura, T.; Higashiguchi, M.; Shimada, K.; Namatame, H.; Taniguchi, M. Direct observation of Tomonaga-Luttinger-liquid state in carbon nanotubes at low temperatures. *Nature* **2003,** *426* (6966), 540-544.

30. Yoshioka, H. Tomonaga-Luttinger-liquid behavior in conducting carbon nanotubes with open ends. *Physica E* **2003,** *18*, 212-213.

31. Kane, C.; Balents, L.; Fisher, M. P. A. Coulomb interactions and mesoscopic effects in carbon nanotubes. *Phys. Rev. Lett.* **1997,** *79*, 5086-5089.

32. Egger, R.; Gogolin, A. O. Effective low-energy theory for correlated carbon nanotubes. *Phys. Rev. Lett.* **1997,** *79*, 5082-5085.

33. Mattsson, A. E.; Eggert, S.; Johannesson, H. Properties of a Luttinger liquid with boundaries at finite temperature and size. *Phys. Rev. B* **1997,** *56*, 15615-15628.

34. De Martino, A.; Egger, R. Effective low-energy theory of superconductivity in carbon nanotube ropes. *Phys. Rev. B* **2004,** *70* (1), 014508.

35. Kociak, M.; Kasumov, A. Y.; Gu+¬ron, S.; Reulet, B.; Khodos, I. I.; Gorbatov, Y.; Volkov, V. T.; Vaccarini, L.; Bouchiat, H. Superconductivity in Ropes of Single-Walled Carbon Nanotubes. *Phys. Rev. Lett.* **2001,** *86* (11), 2416-2419.

36. Kasumov, A.; Kociak, M.; Ferrier, M.; Deblock, R.; Gu+¬ron, S.; Reulet, B.; Khodos, I.; St+¬phan, O.; Bouchiat, H. Quantum transport through carbon nanotubes: Proximity-induced and intrinsic superconductivity. *Phys. Rev. B* **2003,** *68* (21), 214521.

37. Weisman, R. B.; Bachilo, S. M. Dependence of Optical Transition Energies on Structure for Single-Walled Carbon Nanotubes in Aqueous Suspension: An Empirical Kataura Plot. *Nano Letters* **2003,** *3* (9), 1235-1238.

38. Perebeinos, V.; Tersoff, J.; Avouris, P. Scaling of excitons in carbon nanotubes. *Phys. Rev. Lett.* **2004,** *92*, 257402.

39. Spataru, C. D.; Ismail-Beigi, S.; Benedict, L. X.; Louie, S. G. Excitonic effects and optical spectra of single-walled carbon nanotubes. *Phys. Rev. Lett.* **2004,** *92*, 077402.

40. Ando, T. J. Excitons in carbon nanotubes. *J. Phys. Soc. Jpn* **1997,** *66*, 1066-1073.

41. Dresselhaus, M. S.; Dresselhaus, G.; Jorio, A.; Souza Filho, A. G.; Saito, R. Raman spectroscopy on isolated single wall carbon nanotubes. *Carbon* **2002,** *40* (12), 2043-2061.

42. Seung, Y. J.; Perello, D.; Sung, J. K.; Jin, H. J.; Kang, B. R.; Woo, J. Y.; Dong, J. B.; Minhee, Y.; Young, H. L. Chirality-specific transport phenomena of isolated single-walled carbon nanotube. *physica status solidi (b)* **2007,** *244* (11), 4204-4211.

43. Rao, A. M.; Richter, E.; Bandow, S.; Chase, B.; Eklund, P. C.; Williams, K. A.; Fang, S.; Subbaswamy, K. R.; Menon, M.; Thess, A.; Smalley, R. E.; Dresselhaus, G.; Dresselhaus, M. S. Diameter-Selective Raman Scattering from Vibrational Modes in Carbon Nanotubes. *Science* **1997,** *275* (5297), 187-191.

44. Dresselhaus, M. S.; Dresselhaus, G.; Jorio, A.; Souza, A. G.; Saito, R. Raman spectroscopy on isolated single wall carbon nanotubes. *Carbon* **2002,** *40*, 2043-2061.

45. Anderson, N.; Hartschuh, A.; Novotny, L. Chirality Changes in Carbon Nanotubes Studied with Near-Field Raman Spectroscopy. *Nano Letters* **2007,** *7* (3), 577-582.

46. Perebeinos, V.; Avouris, P. Exciton Ionization, FranzΓêÆKeldysh, and Stark Effects in Carbon Nanotubes. *Nano Letters* **2007,** *7* (3), 609-613.

47. Perello, D. J.; ChuLim, S.; Chae, S. J.; Lee, I.; Kim, M.; Lee, Y. H.; Yun, M. Anomalous Schottky Barriers and Contact Band-to-Band Tunneling in Carbon Nanotube Transistors. *ACS Nano* **2010,** *4* (6), 3103-3108.

48. Kim, W.; Javey, A.; Vermesh, O.; Wang, Q.; Li, Y.; Dai, H. Hysteresis Caused by Water Molecules in Carbon Nanotube Field-Effect Transistors. *Nano Letters* **2003,** *3* (2), 193-198.

49. Lim, S. C.; Jang, J. H.; Bae, D. J.; Han, G. H.; Lee, S.; Yeo, I. S.; Lee, Y. H. Contact resistance between metal and carbon nanotube interconnects: Effect of work function and wettability. *Applied Physics Letters* **2009,** *95* (26), 264103.

50. Tans, S.; Verschueren, A.; Dekker, C. Room-temperature transistor based on a single carbon nanotube. *Nature* **1998,** *393*, 49-52.

51. Postma, H. W. C.; Teepen, T.; Yao, Z.; Grifoni, M.; Dekker, C. Carbon Nanotube Single-Electron Transistors at Room Temperature. *Science* **2001,** *293* (5527), 76-79.

52. Nygard, J.; Cobden, D. H.; Bockrath, M.; McEuen, P. L.; Lindelof, P. E. Electrical transport measurements on single-walled carbon nanotubes. *Appl Phys A* **1999,** *69* (3), 297-304.

53. Cobden, D. H.; Nyg+Ñrd, J. Shell Filling in Closed Single-Wall Carbon Nanotube Quantum Dots. *Phys. Rev. Lett.* **2002,** *89* (4), 046803.

54. Zhu, W.; Bower, C.; Zhou, O.; Kochanski, G.; Jin, S. Large current density from carbon nanotube field emitters. *Applied Physics Letters* **1999,** *75* (6), 873-875.

55. Javey, A.; Guo, J.; Farmer, D. B.; Wang, Q.; Wang, D.; Gordon, R. G.; Lundstrom, M.; Dai, H. Carbon Nanotube Field-Effect Transistors with Integrated Ohmic Contacts and High-+¦ Gate Dielectrics. *Nano Letters* **2004,** *4* (3), 447-450.

56. Yu, W. J.; Kim, U. J.; Kang, B. R.; Lee, I. H.; Lee, E. H.; Lee, Y. H. Adaptive Logic Circuits with Doping-Free Ambipolar Carbon Nanotube Transistors. *Nano Letters* **2009,** *9* (4), 1401-1405.

57. Zhang, Z.; Liang, X.; Wang, S.; Yao, K.; Hu, Y.; Zhu, Y.; Chen, Q.; Zhou, W.; Li, Y.; Yao, Y.; Zhang, J.; Peng, L. M. Doping-Free Fabrication of Carbon Nanotube Based Ballistic CMOS Devices and Circuits. *Nano Letters* **2007,** *7* (12), 3603-3607.

58. Woo Jong Yu et al . Bias-induced doping engineering with ionic adsorbates on single-walled carbon nanotube thin film transistors. New Journal of Physics 10[11], 113013. 2008.
Ref Type: Abstract

59. Lin, Y. M.; Appenzeller, J.; Avouris, P. Ambipolar-to-Unipolar Conversion of Carbon Nanotube Transistors by Gate Structure Engineering. *Nano Letters* **2004,** *4* (5), 947-950.

60. Freitag, M.; Tsang, J. C.; Bol, A.; Yuan, D.; Liu, J.; Avouris, P. Imaging of the Schottky Barriers and Charge Depletion in Carbon Nanotube Transistors. *Nano Letters* **2007,** *7* (7), 2037-2042.

61. Xue, Y.; Ratner, M. A. Scaling analysis of Schottky barriers at metal-embedded semiconducting carbon nanotube interfaces. *Phys. Rev. B* **2004,** *69* (16), 161402.

62. Chen, Y. F.; Fuhrer, M. S. Tuning from Thermionic Emission to Ohmic Tunnel Contacts via Doping in Schottky-Barrier Nanotube Transistors. *Nano Letters* **2006,** *6* (9), 2158-2162.

63. Shim, M.; Javey, A.; Kam, N. W. S.; Dai, H. Polymer functionalization for air-stable n-type carbon nanotube field-effect transistors. *J. Am. Chem. Soc.* **2001,** *123*, 11512-11513.

64. Heinze, S.; Tersoff, J.; Martel, R.; Derycke, V.; Appenzeller, J.; Avouris, P. Carbon Nanotubes as Schottky Barrier Transistors. *Phys. Rev. Lett.* **2002,** *89* (10), 106801.

65. Xiaodong, C.; Freitag, M.; Martel, R.; Brus, L.; Avouris, P. Controlling energy-level alignments at carbon nanotube/Au contacts. *Nano Letters* **2003,** *3* (6), 783-787.

66. McClain, D.; Thomas, N.; Youkey, S.; Schaller, R.; Jiao, J.; O'Brien, K. P. Impact of oxygen adsorption on a population of mass produced carbon nanotube field effect transistors. *Carbon* **2009,** *47* (6), 1493-1500.

67. Collins, P. G.; Arnold, M. S.; Avouris, P. Engineering carbon nanotubes and nanotube circuits using electrical breakdown. *Science* **2001,** *292* (5517), 706-713.

68. Nosho, Y.; Ohno, Y.; Kishimoto, S.; Mizutani, T. Relation between conduction property and work function of contact metal in carbon nanotube field-effect transistors. *Nanotechnology* **2006,** *17* (14), 3412-3415.

69. Lθonard, F.; Tersoff, J. Role of Fermi-Level Pinning in Nanotube Schottky Diodes. *Phys. Rev. Lett.* **2000,** *84* (20), 4693.

70. Xue, Y.; Ratner, M. A. Schottky barriers at metal-finite semiconducting carbon nanotube interfaces. *Applied Physics Letters* **2003,** *83* (12), 2429-2431.

71. Sze, S. M. *Physics of Semiconductor Devices;* Wiley-Interscience: New York, 1981.

72. Chen, Z.; Appenzeller, J.; Lin, Y. M.; Sippel-Oakley, J.; Rinzler, A. G.; Tang, J.; Wind, S. J.; Solomon, P. M.; Avouris, P. An Integrated Logic Circuit Assembled on a Single Carbon Nanotube. *Science* **2006,** *311* (5768), 1735.

73. Bachtold, A.; Hadley, P.; Nakanishi, T.; Dekker, C. Logic circuits with carbon nanotube transistors. *Science* **2001,** *294,* 1317-1320.

74. Chen, Z.; Appenzeller, J.; Knoch, J.; Lin, Y. M.; Avouris, P. The Role of MetalΓêÆNanotube Contact in the Performance of Carbon Nanotube Field-Effect Transistors. *Nano Letters* **2005,** *5* (7), 1497-1502.

75. Appenzeller, J.; Radosavljevi-ç, M.; Knoch, J.; Avouris, P. Tunneling Versus Thermionic Emission in One-Dimensional Semiconductors. *Phys. Rev. Lett.* **2004,** *92* (4), 048301.

76. Javey, A.; Wang, Q.; Ural, A.; Li, Y.; Dai, H. Carbon Nanotube Transistor Arrays for Multistage Complementary Logic and Ring Oscillators. *Nano Letters* **2002,** *2* (9), 929-932.

77. Derycke, V.; Martel, R.; Appenzeller, J.; Avouris, P. Carbon nanotube inter- and intramolecular logic gates. *Nano. Lett.* **2001,** *1,* 453-456.

78. Martel, R.; Wong, H. S. P.; Chan, K.; Avouris, P. Carbon nanotube field effect transistors for logic applications. *IEDM Tech. Dig.* **2001,** 159-162.

79. Bandow, S.; Asaka, S.; Saito, Y.; Rao, A. M.; Grigorian, L.; Richter, E.; Eklund, P. C. Effect of the Growth Temperature on the Diameter Distribution and Chirality of Single-Wall Carbon Nanotubes. *Phys. Rev. Lett.* **1998,** *80* (17), 3779.

80. Yao, Y.; Li, Q.; Zhang, J.; Liu, R.; Jiao, L.; Zhu, Y. T.; Liu, Z. Temperature-mediated growth of single-walled carbon-nanotube intramolecular junctions. *Nat Mater* **2007,** *6* (4), 283-286.

81. Ding, L.; Tselev, A.; Wang, J.; Yuan, D.; Chu, H.; McNicholas, T. P.; Li, Y.; Liu, J. Selective Growth of Well-Aligned Semiconducting Single-Walled Carbon Nanotubes. *Nano Letters* **2009,** *9* (2), 800-805.

82. Huang, S. M.; Woodson, M.; Smalley, R.; Liu, J. Growth mechanism of oriented long single walled carbon nanotubes using fast-heating chemical vapor deposition process. *Nano Lett.* **2004,** *4*, 1025-1028.

83. Perello, D. J.; Yu, W. J.; Bae, D. J.; Chae, S. J.; Kim, M. J.; Lee, Y. H.; Yun, M. Analysis of hopping conduction in semiconducting and metallic carbon nanotube devices. *Journal of Applied Physics* **2009,** *105* (12), 124309-5.

84. Manohara, H. M.; Wong, E. W.; Schlecht, E.; Hunt, B. D.; Siegel, P. H. Carbon Nanotube Schottky Diodes Using Ti/Schottky and Pt/Ohmic Contacts for High Frequency Applications. *Nano Letters* **2005,** *5* (7), 1469-1474.

85. Yang, M. H.; Teo, K. B. K.; Milne, W. I.; Hasko, D. G. Carbon nanotube Schottky diode and directionally dependent field-effect transistor using asymmetrical contacts. *Applied Physics Letters* **2005,** *87* (25), 253116-3.

86. Lu, C.; An, L.; Fu, Q.; Liu, J.; Zhang, H.; Murduck, J. Schottky diodes from asymmetric metal-nanotube contacts. *Applied Physics Letters* **2006,** *88* (13), 133501-133503.

87. Li, H.; Zhang, Q.; Marzari, N. Unique Carbon-Nanotube Field-Effect Transistors with Asymmetric Source and Drain Contacts. *Nano Letters* **2007,** *8* (1), 64-68.

88. Lee, J. U. Photovoltaic effect in ideal carbon nanotube diodes. *Applied Physics Letters* **2005,** *87* (7), 073101-073103.

89. Jin, Z.; Chu, H.; Wang, J.; Hong, J.; Tan, W.; Li, Y. Ultralow Feeding Gas Flow Guiding Growth of Large-Scale Horizontally Aligned Single-Walled Carbon Nanotube Arrays. *Nano Letters* **2007,** *7* (7), 2073-2079.

90. Jonker, B. T.; Morar, J. F.; Park, R. L. Surface states and oxygen chemisorption on Ti(0001). *Phys. Rev. B* **1981,** *24* (6), 2951.

91. Szadkowski, A. J.; Kalnitsky, A.; Ma, K. B.; Zukotynski, S. Implications of the change in work function of chromium by the presence of hydrogen on the properties of electrical contact between chromium and hydrogenated amorphous silicon. *Journal of Applied Physics* **1982,** *53* (1), 557-558.

92. Appenzeller, J.; Knoch, J.; Radosavljevi-ç, M.; Avouris, P. Multimode Transport in Schottky-Barrier Carbon-Nanotube Field-Effect Transistors. *Phys. Rev. Lett.* **2004,** *92* (22), 226802.

93. Ustaze, S.; Lacombe, S.; Guillemot, L.; Esaulov, V. A.; M.Canepa Electron transfer on oxygen-covered Ag(110) and Al(111) surfaces: work function versus local electronic effects. *Surface Science* **1998,** *414* (1-2), L938-L944.

94. Sankaranarayanan, S. K. R. S.; Kaxiras, E.; Ramanathan, S. Electric field tuning of oxygen stoichiometry at oxide surfaces: molecular dynamics simulations studies of zirconia. *Energy & Environmental Science*.

95. Shapiro, S. S.; Wilk, M. B. An analysis of variance test for normality (complete samples). *Biometrika* **1965,** *52* (3-4), 591-611.

96. Crowell, C. R.; Rideout, V. L. Normalized thermionic-field (T-F) emission in metal-semiconductor (Schottky) barriers. *Solid-State Electronics* **1969,** *12* (2), 89-105.

97. Padovani, F. A.; Stratton, R. Field and thermionic-field emission in Schottky barriers. *Solid-State Electronics* **1966,** *9* (7), 695-707.

98. Perello, D. J.; Lim, S. C.; Chae, S. J.; Lee, I.; Kim, M.; Lee, Y. H.; Yun, M. Current anisotropy of carbon nanotube diodes: Voltage and work function dependence. *Applied Physics Letters* **2010,** *96* (26), 263107-3.

99. Javey, A.; Guo, J.; Wang, Q.; Lundstrom, M.; Dai, H. J. Ballistic carbon nanotube field-effect transistors. *Nature* **2003,** *424*, 654-657.

100. Nonnenmacher, M.; O'Boyle, M. P.; Wickramasinghe, H. K. Kelvin probe force microscopy. *Applied Physics Letters* **1991,** *58* (25), 2921-2923.

101. Diefeng, G.; Dey, S. K.; Majhi, P. Effective work function of Pt, Pd, and Re on atomic layer deposited HfO2. *Applied Physics Letters* **2006,** *89* (8), 82907-1.

102. Novoselov, K. S. Electric field effect in atomically thin carbon films. *Science* **2004,** *306*, 666-669.

103. Zhang, Y.; Tan, Y.-W.; Stormer, H. L.; Kim, P. Experimental observation of the quantum Hall effect and Berry's phase in graphene. *Nature* **2005,** *438*, 201-204.

104. Stander, N.; Huard, B.; Goldhaber-Gordon, D. Evidence for Klein Tunneling in Graphene p-n Junctions. *Phys. Rev. Lett.* **2009,** *102* (2), 026807.

105. Young, A. F.; Kim, P. Quantum interference and Klein tunnelling in graphene heterojunctions. *Nat Phys* **2009,** *5* (3), 222-226.

106. Beenakker, C. W. J. Colloquium: Andreev reflection and Klein tunneling in graphene. *Reviews of Modern Physics* **2008,** *80* (4), 1337-1354.

107. Bolotin, K. I.; Sikes, K. J.; Jiang, Z.; Klima, M.; Fudenberg, G.; Hone, J.; Kim, P.; Stormer, H. L. Ultrahigh electron mobility in suspended graphene. *Solid State Communications* **2008,** *146* (9ΓÇô10), 351-355.

108. Hwang, E. H.; Adam, S.; Das Sarma, S. Carrier Transport in Two-Dimensional Graphene Layers. *Phys. Rev. Lett.* **2007,** *98* (18), 186806.

109. Orlita, M.; Faugeras, C.; Plochocka, P.; Neugebauer, P.; Martinez, G.; Maude, D. K.; Barra, A. L.; Sprinkle, M.; Berger, C.; de Heer, W. A.; Potemski, M. Approaching the Dirac Point in High-Mobility Multilayer Epitaxial Graphene. *Phys. Rev. Lett.* **2008,** *101* (26), 267601.

110. Balandin, A. A.; Ghosh, S.; Bao, W.; Calizo, I.; Teweldebrhan, D.; Miao, F.; Lau, C. N. Superior Thermal Conductivity of Single-Layer Graphene. *Nano Letters* **2008,** *8* (3), 902-907.

111. Bolotin, K. I.; Ghahari, F.; Shulman, M. D.; Stormer, H. L.; Kim, P. Observation of the fractional quantum Hall effect in graphene. *Nature* **2009,** *462* (7270), 196-199.

112. Geim, A. K.; Novoselov, K. S. The rise of graphene. *Nature Mater.* **2007,** *6*, 183-191.

113. Sutter, P.; Sadowski, J. T.; Sutter, E. Graphene on Pt(111): Growth and substrate interaction. *Phys. Rev. B* **2009,** *80* (24), 245411.

114. Tromp, R. M.; Hannon, J. B. Thermodynamics and Kinetics of Graphene Growth on SiC(0001). *Phys. Rev. Lett.* **2009,** *102* (10), 106104.

115. Lin, Y. M.; Dimitrakopoulos, C.; Jenkins, K. A.; Farmer, D. B.; Chiu, H. Y.; Grill, A.; Avouris, P. 100-GHz Transistors from Wafer-Scale Epitaxial Graphene. *Science* **2010,** *327* (5966), 662.

116. Novoselov, K. S.; Geim, A. K.; Morozov, S. V.; Jiang, D.; Zhang, Y.; Dubonos, S. V.; Grigorieva, I. V.; Firsov, A. A. Electric Field Effect in Atomically Thin Carbon Films. *Science* **2004,** *306* (5696), 666-669.

117. Reina, A.; Jia, X.; Ho, J.; Nezich, D.; Son, H.; Bulovic, V.; Dresselhaus, M. S.; Kong, J. Large Area, Few-Layer Graphene Films on Arbitrary Substrates by Chemical Vapor Deposition. *Nano Letters* **2008,** *9* (1), 30-35.

118. Chae, S. J.; G++ne+ƒ, F.; Kim, K. K.; Kim, E. S.; Han, G. H.; Kim, S. M.; Shin, H. J.; Yoon, S. M.; Choi, J. Y.; Park, M. H.; Yang, C. W.; Pribat, D.; Lee, Y. H. Synthesis of Large-Area Graphene Layers on Poly-Nickel Substrate by Chemical Vapor Deposition: Wrinkle Formation. *Advanced Materials* **2009,** *21* (22), 2328-2333.

119. Yu, W. J.; Chae, S. H.; Perello, D.; Lee, S. Y.; Han, G. H.; Yun, M.; Lee, Y. H. Synthesis of Edge-Closed Graphene Ribbons with Enhanced Conductivity. *ACS Nano* **2010,** *4* (9), 5480-5486.

120. Li, X.; Cai, W.; Colombo, L.; Ruoff, R. S. Evolution of Graphene Growth on Ni and Cu by Carbon Isotope Labeling. *Nano Letters* **2009,** *9* (12), 4268-4272.

121. Gao, L.; Ren, W.; Xu, H.; Jin, L.; Wang, Z.; Ma, T.; Ma, L. P.; Zhang, Z.; Fu, Q.; Peng, L. M.; Bao, X.; Cheng, H. M. Repeated growth and bubbling transfer of graphene with millimetre-size single-crystal grains using platinum. *Nat Commun* **2012,** *3*, 699.

122. Han, G. H.; Gunes, F.; Bae, J. J.; Kim, E. S.; Chae, S. J.; Shin, H. J.; Choi, J. Y.; Pribat, D.; Lee, Y. H. Influence of Copper Morphology in Forming Nucleation Seeds for Graphene Growth. *Nano Letters* **2011,** *11* (10), 4144-4148.

123. Yan, Z.; Lin, J.; Peng, Z.; Sun, Z.; Zhu, Y.; Li, L.; Xiang, C.; Samuel, E. L. c.; Kittrell, C.; Tour, J. M. Toward the Synthesis of Wafer-Scale Single-Crystal Graphene on Copper Foils. *ACS Nano* **2012,** *6* (10), 9110-9117.

124. Zhang, Y.; Tang, T. T.; Girit, C.; Hao, Z.; Martin, M. C.; Zettl, A.; Crommie, M. F.; Shen, Y. R.; Wang, F. Direct observation of a widely tunable bandgap in bilayer graphene. *Nature* **2009,** *459* (7248), 820-823.

125. Han, M. Y.; Ozyilmaz, B.; Zhang, Y.; Kim, P. Energy band gap engineering of graphene nanoribbons. *Phys. Rev. Lett.* **2007,** *98,* 206805.

126. Han, M. Y.; Brant, J. C.; Kim, P. Electron Transport in Disordered Graphene Nanoribbons. *Phys. Rev. Lett.* **2010,** *104* (5), 056801.

127. Han, M. Y.; +ûzyilmaz, B.; Zhang, Y.; Kim, P. Energy Band-Gap Engineering of Graphene Nanoribbons. *Phys. Rev. Lett.* **2007,** *98* (20), 206805.

128. Son, Y. W.; Cohen, M. L.; Louie, S. G. Energy gaps in graphene nanoribbons. *Phys. Rev. Lett.* **2006,** *97,* 216803.

129. Son, Y. W.; Cohen, M. L.; Louie, S. G. Half-metallic graphene nanoribbons. *Nature* **2006,** *444,* 347-349.

130. Lu, Y.; Merchant, C. A.; Drndi-ç, M.; Johnson, A. T. C. In Situ Electronic Characterization of Graphene Nanoconstrictions Fabricated in a Transmission Electron Microscope. *Nano Letters* **2011,** *11* (12), 5184-5188.

131. Lu, Y.; Goldsmith, B.; Strachan, D. R.; Lim, J. H.; Luo, Z.; Johnson, A. T. C. High-On/Off-Ratio Graphene Nanoconstriction Field-Effect Transistor. *Small* **2010,** *6* (23), 2748-2754.

132. Ozyilmaz, B.; Jarillo-Herrero, P.; Efetov, D.; Kim, P. Electronic transport in locally gated graphene nanoconstrictions. *Applied Physics Letters* **2007,** *91* (19), 192107-3.

133. Malard, L. M.; Pimenta, M. A.; Dresselhaus, G.; Dresselhaus, M. S. Raman spectroscopy in graphene. *Physics Reports* **2009,** *473* (5-6), 51-87.

134. Tuinstra, F.; Koenig, J. L. Raman Spectrum of Graphite. *The Journal of Chemical Physics* **1970,** *53* (3), 1126-1130.

135. Zhang, Y.; Tan, Y. W.; Stormer, H. L.; Kim, P. Experimental observation of the quantum Hall effect and Berry/'s phase in graphene. *Nature* **2005,** *438,* 201-204.

136. Katsnelson, M. I.; Novoselov, K. S.; Geim, A. K. Unconventional quantum Hall effect and Berry's phase of 2[pi] in bilayer graphene. *Nature Phys.* **2006,** *2,* 177-180.

137. Wu, Y.; Lin, Y. M.; Bol, A. A.; Jenkins, K. A.; Xia, F.; Farmer, D. B.; Zhu, Y.; Avouris, P. High-frequency, scaled graphene transistors on diamond-like carbon. *Nature* **2011,** *472* (7341), 74-78.

138. Barreiro, A.; van der Zant, H. S. J.; Vandersypen, L. M. K. Quantum Dots at Room Temperature Carved out from Few-Layer Graphene. *Nano Letters* **2012**.

139. Stampfer, C.; Guttinger, J.; Molitor, F.; Graf, D.; Ihn, T.; Ensslin, K. Tunable Coulomb blockade in nanostructured graphene. *Applied Physics Letters* **2008,** *92* (1), 012102-012103.

140. Murali, R.; Yang, Y.; Brenner, K.; Beck, T.; Meindl, J. D. Breakdown current density of graphene nanoribbons. *Applied Physics Letters* **2009,** *94* (24), 243114-3.

141. Pan, Z.; Liu, N.; Fu, L.; Liu, Z. Wrinkle Engineering: A New Approach to Massive Graphene Nanoribbon Arrays. *Journal of the American Chemical Society* **2011,** *133* (44), 17578-17581.

142. Kosynkin, D. V.; Higginbotham, A. L.; Sinitskii, A.; Lomeda, J. R.; Dimiev, A.; Price, B. K.; Tour, J. M. Longitudinal unzipping of carbon nanotubes to form graphene nanoribbons. *Nature* **2009,** *458* (7240), 872-876.

143. Wang, X.; Ouyang, Y.; Li, X.; Wang, H.; Guo, J.; Dai, H. Room-Temperature All-Semiconducting Sub-10-nm Graphene Nanoribbon Field-Effect Transistors. *Phys. Rev. Lett.* **2008,** *100* (20), 206803-206804.

144. Reina, A.; Son, H.; Jiao, L.; Fan, B.; Dresselhaus, M. S.; Liu, Z.; Kong, J. Transferring and Identification of Single- and Few-Layer Graphene on Arbitrary Substrates. *The Journal of Physical Chemistry C* **2008,** *112* (46), 17741-17744.

145. Li, X.; Wang, X.; Zhang, L.; Lee, S.; Dai, H. Chemically derived, ultrasmooth graphene nanoribbon semiconductors. *Science* **2008,** *319*, 1229-1232.

146. Zhang, Y.; Brar, V. W.; Girit, C.; Zettl, A.; Crommie, M. F. Origin of spatial charge inhomogeneity in graphene. *Nat Phys* **2009,** *5* (10), 722-726.

147. Li, X.; Cai, W.; An, J.; Kim, S.; Nah, J.; Yang, D.; Piner, R.; Velamakanni, A.; Jung, I.; Tutuc, E.; Banerjee, S. K.; Colombo, L.; Ruoff, R. S. Large-Area Synthesis of High-Quality and Uniform Graphene Films on Copper Foils. *Science* **2009,** *324* (5932), 1312-1314.

148. Cao, Q.; Han, S. J.; Tulevski, G. S.; Zhu, Y.; Lu, D. D.; Haensch, W. Arrays of single-walled carbon nanotubes with full surface coverage for high-performance electronics. *Nat Nano* **2013,** *advance online publication*.

149. Gunes, F.; Han, G. H.; Shin, H. J.; Lee, S. Y.; Jin, M. E. I. H.; Duong, D. L.; Chae, S. J.; Kim, E. S.; Yao, F. E. I.; Benayad, A. N. A. S.; Choi, J. Y.; Lee, Y. H. UV-Light-Assisted Oxidative sp3 Hybridization of Graphene. *Nano* **2011,** *06* (05), 409-418.

150. Duong, D. L.; Han, G. H.; Lee, S. M.; Gunes, F.; Kim, E. S.; Kim, S. T.; Kim, H.; Ta, Q. H.; So, K. P.; Yoon, S. J.; Chae, S. J.; Jo, Y. W.; Park, M. H.; Chae, S. H.; Lim, S. C.; Choi, J. Y.; Lee, Y. H. Probing graphene grain boundaries with optical microscopy. *Nature* **2012,** *490* (7419), 235-239.

151. Tanaka, T.; Jin, H.; Miyata, Y.; Fujii, S.; Suga, H.; Naitoh, Y.; Minari, T.; Miyadera, T.; Tsukagoshi, K.; Kataura, H. Simple and Scalable Gel-Based Separation of Metallic and Semiconducting Carbon Nanotubes. *Nano Letters* **2009,** *9* (4), 1497-1500.

152. Park, H.; Afzali, A.; Han, S. J.; Tulevski, G. S.; Franklin, A. D.; Tersoff, J.; Hannon, J. B.; Haensch, W. High-density integration of carbon nanotubes via chemical self-assembly. *Nat Nano* **2012,** *7* (12), 787-791.

153. Reich, S.; Thomsen, C.; Maultzsch, J. *Carbon Nanotubes: Basic Concepts and Physical Properties;* Wiley - VCH: New York, 2004.

154. Saito, R.; Fujita, M.; Dresselhaus, G.; Dresselhaus, M. S. Electronic structure of chiral graphene tubules. *Applied Physics Letters* **1992,** *60* (18), 2204-2206.